Progress in Materials Science 77 (2016) 125–211

Contents lists available at ScienceDirect

Progress in Materials Science

journal homepage: www.elsevier.com/locate/pmatsci

# Advances in tailoring the electronic properties of single-walled carbon nanotubes

Marianna V. Kharlamova *

*Faculty of Physics, University of Vienna, Strudlhofgasse 4, 1090 Vienna, Austria*
*Department of Materials Science, Lomonosov Moscow State University, Leninskie gory 1-3, 119991 Moscow, Russia*

ARTICLE INFO

*Article history:*
Received 19 January 2014
Received in revised form 9 December 2014
Accepted 9 May 2015
Available online 28 September 2015

*Keywords:*
Single-walled carbon nanotube
Filling
Nanochemical reaction
Electronic properties
Electron acceptor
Electron donor
Doping

ABSTRACT

Considerable progress has been made in the last several years in the fields of investigation and understanding of the influence of encapsulated substances on the electronic properties of single-walled carbon nanotubes (SWCNTs). Relevant data on the modified electronic properties of filled SWCNTs were obtained. The possibility of achieving both acceptor and donor doping and precise changes of the SWCNT doping level by the filling of channels and transformation of incorporated substances was demonstrated. This article presents a comprehensive review of the current status of the research on the electronic properties of filled SWCNTs. The review begins with a brief description of basic aspects of the band theory of solids and peculiarities of the band structure and electronic properties of SWCNTs. The next part of the review is dedicated to a systematization and description of different methods for modification of the SWCNT electronic properties. Then, the review introduces filling methods of SWCNT inner channels. The main part of the review is dedicated to an analysis, systematization and generalization of the up-to-date reported results on experimental and theoretical investigations of the electronic properties of filled SWCNTs and nanostructures obtained as result of chemical reactions inside the SWCNT channels. Finally, the possible applications of filled nanotubes are highlighted.



* Address: Faculty of Physics, University of Vienna, Strudlhofgasse 4, 1090 Vienna, Austria. Tel.: +43 (0)1 42 77 51304; fax: +43 (0)1 42 77 51375.
*E-mail address:* mv.kharlamova@gmail.com

http://dx.doi.org/10.1016/j.pmatsci.2015.09.001
0079-6425/

**Nomenclature**

*Acronyms*

| | |
|---|---|
| AFM | atomic force microscopy |
| BWF | Breit–Wigner–Fano function |
| CVD | chemical vapor deposition |
| DFT | density functional theory |
| DMF | dimethylformamide |
| DNBN | 3,5-dinitrobenzonitrile |
| DOS | density of states |
| DWCNT | double-walled carbon nanotube |
| EC charging | electrochemical charging |
| EELS | electron energy loss spectroscopy |
| $F_4$TCNQ | tetrafluorocyano-*p*-quinodimethane |
| FWHM | full width at half maximum |
| HRTEM | high-resolution transmission electron microscopy |
| LO phonon | longitudinal optical phonon |
| MRI | magnetic resonance imaging |
| NIR | near-infrared |
| NT | nanotube |
| OAS | optical absorption spectroscopy |
| PLS | photoluminescence spectroscopy |
| QM | quantum-chemical modeling |
| RBM | radial breathing mode |
| RS | Raman spectroscopy |
| STS | scanning tunneling spectroscopy |
| SWCNT | single-walled carbon nanotube |
| TCNQ | tetracyano-*p*-quinodimethane |
| TDAE | tetrakis(dimethylamino)ethylene |
| TEM | transmission electron microscopy |
| TMTSF | tetramethyl-tetraselenefulvalene |
| TO phonon | transversal optical phonon |
| TTF | tetrathiafulvalene |
| UPS | ultraviolet photoelectron spectroscopy |
| UV | ultraviolet |
| vHs | van Hove singularities |
| WF | work function |
| XAS | X-ray absorption spectroscopy |
| XES | X-ray emission spectroscopy |
| XPS | X-ray photoelectron spectroscopy |
| X@SWCNT | single-walled carbon nanotube filled with substance X |
| 1D | one-dimensional |

*Symbols*

| | |
|---|---|
| $\mathbf{a_1}$, $\mathbf{a_2}$, $\mathbf{a_3}$ | basis vectors of the direct lattice |
| $a$ | lattice parameter of a graphene layer |
| $a_{c-c}$ | the nearest-neighbor carbon–carbon distance in a graphene layer |
| $\mathbf{b_1}$, $\mathbf{b_2}$, $\mathbf{b_3}$ | basis vectors of the reciprocal lattice |
| $\mathbf{C_h}$ | chiral vector of a nanotube |
| $d$ | the highest common divisor of chirality indexes $n$ and $m$ of a nanotube |
| $d_R$ | the greatest common divisor of $2m + n$ and $2n + m$ |
| $d_t$ | diameter of nanotube |
| $D(E)$ | density of states |
| $D(E_F)$ | density of states at the Fermi energy |

| | |
|---|---|
| $e$ | charge of an electron |
| $e^{i\mathbf{kr}}$ | plane wave that runs along the vector $\mathbf{k}$ in a crystal |
| $E$ | energy of the system of all particles in a solid |
| $E_e$ | energy of electrons in a solid |
| $E_i$ | energy of the $i$-th electron in a solid |
| $E_F$ | Fermi energy |
| $E_n(\mathbf{k})$ | energy states of electrons in the periodic potential of a crystal, which define the band structure of a crystalline solid |
| $E^{\pm}_{g2D}(\mathbf{k})$ | two-dimensional energy dispersion relations of graphene ($E^{+}$ and $E^{-}$ correspond to the valence $\pi$ and the conduction $\pi^{*}$ energy bands) |
| $E^{\pm}_{1D}(k)$ | one-dimensional energy dispersion relations of nanotubes ($E^{+}$ and $E^{-}$ correspond to the valence $\pi$ and the conduction $\pi^{*}$ energy bands) |
| $E_q^{armchair}(k)$ | energy dispersion relations of armchair nanotubes ($q$ is the band index) |
| $E_q^{zigzag}(k)$ | energy dispersion relations of zigzag nanotubes ($q$ is the band index) |
| $E_{ii}^{M}$ | energy of electronic transition between vHs of metallic SWCNTs |
| $E_{ii}^{S}$ | energy of electronic transition between vHs of semiconducting SWCNTs |
| $f(E, T)$ | Fermi–Dirac distribution function |
| $gcd(t_1,t_2)$ | the greatest common divisor of $t_1$ and $t_2$ |
| $G$ | conductance |
| $\widehat{H}$ | Hamiltonian of the system of all particles in a solid |
| $\widehat{H}_i$ | Hamiltonian of the $i$-th electron in a solid |
| $\widehat{J}$ | operator of the kinetic energy of the system of all particles in a solid |
| $\mathbf{k}$ | wave vector of an electron in a crystal |
| $k$ | one-dimensional wave vector of an electron |
| $k_B$ | Boltzmann constant |
| $\mathbf{K}$ | vector of the reciprocal lattice |
| $\mathbf{K_1}$ | vector of the reciprocal lattice of SWCNTs along the circumference |
| $\mathbf{K_2}$ | vector of the reciprocal lattice of SWCNTs along the axis |
| $L$ | circumferential length of nanotube |
| $m_0$ | mass of an electron |
| $M_1$ | the first vHs of metallic SWCNTs |
| $M_\alpha$ | mass of a nucleus |
| $n$ | density of electrons |
| $(n,m)$ | coordinates of the chiral vector (chirality indexes) |
| $N$ | number of hexagons of carbon atoms per unit cell of nanotube |
| $N_0$ | number of electrons in an allowed energy band |
| $\mathbf{p}$ | momentum of a free electron |
| $p$ | density of holes |
| $\mathbf{P}$ | quasi-momentum of an electron in the periodic field of a crystal |
| $q$ | momentum transfer |
| $\mathbf{r_i}$ | coordinates of the $i$-th electron in a solid |
| $\mathbf{R}$ | vector of the direct lattice |
| $\mathbf{R_\alpha}$ | coordinates of the $\alpha$-th nucleus in a solid |
| $\mathbf{R_{\alpha 0}}$ | fixed coordinates of the $\alpha$-th stationary nucleus in a solid |
| $s$ | tight-binding overlap integral of the electronic wave function on adjacent sites in a graphene layer |
| $S$ | $(2 \times 2)$ overlap integral matrix, associated with the two inequivalent atoms of a graphene sheet |
| $S_1$, $S_2$, $S_3$ | the first, second and third vHs of semiconducting SWCNTs |
| $t$ | translational period along the nanotube axis |
| $(t_1,t_2)$ | coordinates of the translational vector of a nanotube |
| $\mathbf{T}$ | translational vector of a nanotube |

| | |
|---|---|
| $T$ | absolute temperature |
| $U$ | potential energy of the system of all particles in a solid |
| $U(\mathbf{r_1}, \mathbf{r_2}, \ldots, \mathbf{r_n}, \mathbf{R_1}, \mathbf{R_2}, \ldots, \mathbf{R_N})$ | potential energy of the interaction between electrons and nuclei in a solid |
| $U_i(\mathbf{r_i})$ | potential energy of the $i$-th electron in the field of all nuclei in a solid |
| $U_{\mathbf{k}}(\mathbf{r})$ | Bloch function with the period of a crystal lattice that depends on the wave vector $\mathbf{k}$ |
| $V_G$ | gate voltage |
| $V(\mathbf{r})$ | potential energy of an electron in a crystal |
| $V_0(\mathbf{R_1}, \mathbf{R_2}, \ldots, \mathbf{R_N})$ | potential energy of the pairwise interaction of nuclei in a solid |
| $Z$ | number of states per unit interval of energy in a crystal with unit volume |
| $\alpha$ | asymmetry parameter of the C 1*s* XPS spectra |
| $\gamma_0$ | the nearest-neighbor carbon–carbon interaction energy of graphene |
| $\Gamma$ | center of the first Brillouin zone of graphene |
| $\varepsilon_{2p}$ | site energy of the 2*p* atomic orbital in a graphene layer |
| $\hbar$ | Plank's constant $h$ divided by $2\pi$ |
| $\mathcal{H}$ | $(2 \times 2)$ Hamiltonian, associated with the two inequivalent atoms of a graphene sheet |
| $\theta$ | chiral angle of a nanotube |
| K | corner of the first Brillouin zone of graphene |
| $\mu_n$ | mobility of electrons |
| $\mu_p$ | mobility of holes |
| M | middle of edges of the first Brillouin zone of graphene |
| $\sigma$ | conductivity |
| $\varphi_i(\mathbf{r_i})$ | wave function of the $i$-th electron in a solid |
| $\varphi_{\mathbf{k}}(\mathbf{r})$ | Bloch wave function of an electron in the periodic field of a crystal |
| $\varphi_{n,\mathbf{k}}(\mathbf{r})$ | wave functions of electrons in a crystal |
| X | edge of the first Brillouin zone of SWCNTs |
| $\psi$ | wave function of the system of all particles in a solid |
| $\psi_e$ | wave function of electrons in a solid |
| $\Omega_i(\mathbf{r_i})$ | energy of the interaction between the $i$-th electron and the averaged field of all other electrons in a solid |

**Contents**

## 1. Introduction

Single-walled carbon nanotubes (SWCNTs) discovered in 1993 [1] are a fascinating class of carbon materials attracting much interest due to their unique chemical, physical, mechanical and structural properties [2]. The SWCNT investigations are propelled by their large potential for energy, mechanical, sensor, field emission, lighting and biological applications [3,4]. One of the most important SWCNT applications belongs to the field of nanoelectronics. Possessing a very small diameter and outstanding physical characteristics, the SWCNTs are considered to be promising elements for electronic device architectures of the next generations [3,4].

A wonderful thing discovered during early SWCNT investigations is that the interior space of nanotubes can be filled with foreign substances. It was firstly demonstrated in 1998 by an example of the encapsulation of fullerene $C_{60}$ [5] and $RuCl_3$ [6] molecules inside the SWCNT channels. Later on, attempts to fill the SWCNTs with other molecules [7–16], simple substances [17–22] and chemical compounds [18,21,23–26] were intensively explored. Special attention was devoted to the analysis of the atomic structure of encapsulated substances that turned out to be different from the one in the bulk state due to confined one-dimensional space of nanotube channels [27–45]. Aside from interest of fundamental science, the possibility of modification of the SWCNT electronic properties by filling the channels [46–48] and conducting nanochemical reactions inside the nanotubes [49–51] was demonstrated. Starting from the aforementioned pioneer works, this topic got increasing attention in the last years, it is currently expanding and of large actuality. The impetus for the development of this nanotube research field is the necessity of creating the methods for tailoring the electronic properties of SWCNTs, which is required for applications of nanotubes in nanoelectronic devices. To date, such applications are limited because there are no methods to directly synthesize nanotubes with defined electronic properties [4,52].

During the last years, several methods were established for the modification of nanotube electronic properties. These methods are the substitution of carbon atoms of SWCNT walls by other atoms, the covalent modification of outer nanotube surface by different functional groups (chemisorption), the non-covalent modification of outer nanotube surface with molecules (physisorption), the intercalation of SWCNT bundles, the filling of the SWCNT channels and the nanochemical reaction inside the SWCNT channels. Among all these approaches, the filling of the SWCNT channels and transformation of encapsulated substances are the most promising methods for tailoring the nanotube electronic properties, because a number of different substances can be incorporated into the SWCNT inner cavities using appropriate filling methods [53–57]. Nanochemical reactions inside the SWCNT channels open a way of fine tuning the SWCNT electronic structure by choosing a specific precursor and conditions for the reaction [49–51]. Thus, the electronic properties of SWCNTs can be engineered for particular applications.

Considerable progress has been made in the last several years in the fields of investigation and understanding of the influence on the electronic properties of substances incorporated into the channels of SWCNTs and obtained by nanochemical reactions inside the SWCNT inner cavities. The advancement of state-of-the-art spectroscopic techniques, such as Raman spectroscopy (RS), optical absorption spectroscopy (OAS), X-ray photoelectron spectroscopy (XPS), X-ray emission spectroscopy (XES), X-ray absorption spectroscopy (XAS), ultraviolet photoelectron spectroscopy (UPS) and photoluminescence spectroscopy (PLS), as well as the methods of quantum-chemical modeling (QM) enabled detailed investigations of the modification of the electronic properties of nanotubes that takes place as result of the encapsulation and chemical transformation of different substances inside their channels.

Relevant data on the modified electronic properties of filled SWCNTs were obtained. The possibility of achieving both acceptor and donor doping and precise changes of the SWCNT doping level by the filling of channels and transformation of encapsulated substances was demonstrated. The tuning of the doping level may modify a number of crucial fundamental properties, such as the allowed optical transitions, the phonon spectrum, the bulk conductance, the internal charge neutrality level and the collective free charge carrier response [58]. This paves the way to a further development toward the application of nanotube-based hybrids as active elements in electronic devices.

The aim of this manuscript is to deliver a comprehensive review of the current status of research on the electronic properties of filled SWCNTs. The first part of the review is dedicated to a brief description of basic aspects of the band theory of solids and peculiarities of the band structure and electronic properties of SWCNTs. The second part of the review is devoted to a systematization and description of different methods for the modification of the SWCNT electronic properties. The third part of the paper is dedicated to a description of filling methods of SWCNTs, including the methods from gas phase, liquid phase, using plasma and chemical reactions inside the SWCNT channels. The main part of the review is dedicated to an analysis, systematization and generalization of the up-to-date reported results on the investigation of electronic properties of filled single-walled carbon nanotubes and nanostructures obtained as a result of nanochemical reactions inside the SWCNT channels. Typical acceptors and donors of electrons are considered as well as the methods of their encapsulation into the nanotube channels. The data obtained in the studies dedicated to the characterization of the electronic properties of filled SWCNTs by experimental and theoretical methods are analyzed. Tailoring the electronic properties of the SWCNTs by nanochemical reactions inside their channels (including the ones with the formation of double-walled carbon nanotubes) is also reviewed. Precursors for the DWCNT formation, methods of their encapsulation and transformation are considered. The collected data on the characterization of the electronic properties of these nanostructures are presented. The final part of the paper reviews possible (demonstrated and expected) applications of filled nanotubes. The substantial part of this section is dedicated to the application in the field of nanoelectronics. Also electrochemical energy storage, catalyst support, biomedical and other applications of filled nanotubes are considered.

## 2. Basics of band theory of solids

### 2.1. Schrödinger equation for solids, one-electron approximation, Bloch functions

Solids are built from atoms that, in turn, consist of nuclei and electrons. The stationary states and energy spectrum of a set of all nuclei and electrons in a solid are described by the Schrödinger equation [59–61]:

$$\widehat{H}\psi = E\psi, \tag{1}$$

where $\widehat{H}$ is the Hamiltonian of the system of all particles, i.e., the whole solid, $\psi$ is the wave function, $E$ is the energy. This eigenvalue equation has a set of solutions $E_n$ and $\psi_n$. The solution of the equation for electrons in a crystal is presented below, following the descriptions given in Refs. [60,61].

The Hamiltonian of a system is the sum of the operator of the kinetic energy of this system $\widehat{J}$ and its potential energy $U$ [59–61]:

$$\widehat{H} = \widehat{J} + U. \tag{2}$$

The operator of the kinetic energy of a solid includes the operator of the kinetic energy of electrons $\sum_i \left(-\frac{\hbar^2}{2m_0}\Delta_i\right)$ and the operator of the kinetic energy of atomic nuclei $\sum_\alpha \left(-\frac{\hbar^2}{2M_\alpha}\Delta_\alpha\right)$, where $\hbar$ is the Plank's constant $h$ divided by $2\pi$, $m_0$ is the mass of an electron, $M_\alpha$ is the mass of a nucleus, $\Delta_i$ and $\Delta_\alpha$ are the Laplace operators for the $i$-th electron and the $\alpha$-th nucleus. The potential energy of the set of particles of the solid includes the potential energy of the pairwise interaction of electrons (the energy of the Coulomb repulsion of electrons) $\frac{1}{2}\sum_i \sum_{j\neq i} \frac{e^2}{r_{ij}}$, the potential energy of the pairwise interaction of nuclei (the energy of the Coulomb repulsion of nuclei) $V_0(\mathbf{R_1}, \mathbf{R_2}, \ldots, \mathbf{R_N})$ and the potential energy of the interaction between electrons and nuclei (the energy of the attraction between electrons and nuclei) $U(\mathbf{r_1}, \mathbf{r_2}, \ldots, \mathbf{r_n}, \mathbf{R_1}, \mathbf{R_2}, \ldots, \mathbf{R_N})$, where $e$ is the charge of an electron, $\mathbf{r_i}$ and $\mathbf{R_\alpha}$ are the coordinates of electrons and nuclei, respectively [59–61].

Thus, the Schrödinger equation can be presented in the following form [59–61]:

$$\left(\sum_i \left(-\frac{\hbar^2}{2m_0}\Delta_i\right) + \sum_\alpha \left(-\frac{\hbar^2}{2M_\alpha}\Delta_\alpha\right) + \frac{1}{2}\sum_i \sum_{j\neq i} \frac{e^2}{r_{ij}} + V_0(\mathbf{R_1}, \mathbf{R_2}, \ldots, \mathbf{R_N}) + U(\mathbf{r_1}, \mathbf{r_2}, \ldots, \mathbf{r_n}, \mathbf{R_1}, \mathbf{R_2}, \ldots, \mathbf{R_N})\right)\psi = E\psi. \tag{3}$$

The wave function in Eq. (3) depends on the coordinates of all electrons and nuclei:

$$\psi = \psi(\mathbf{r_1}, \mathbf{r_2}, \ldots, \mathbf{r_n}, \mathbf{R_1}, \mathbf{R_2}, \ldots, \mathbf{R_N}). \tag{4}$$

Because of the large number of independent variables, which is connected with the total number of particles in the solid, Eq. (3) cannot be solved in its general form [59–61]. To achieve an approximate solution, several approximations have to be applied.

The adiabatic approximation (or Born–Oppenheimer approximation) takes into account the different character of the movement of electrons and nuclei. Because the mass of a nucleus is much larger than the mass of an electron, the velocity of the movements of electrons is much higher than the one of nuclei. Therefore, it is correct to assume that electrons and nuclei move without an energy exchange. In the roughest approximation it is assumed that the nuclei do not move at all [59–61]. Then the coordinates of nuclei $\mathbf{R_1}, \mathbf{R_2}, \ldots, \mathbf{R_N}$ are not variables anymore, but they are the fixed coordinates $\mathbf{R_{10}}, \mathbf{R_{20}}, \ldots, \mathbf{R_{N0}}$. In this case, the Schrödinger Eq. (3) is significantly simplified, because the kinetic energy of nuclei becomes zero and the potential energy of their interaction $V_0$ becomes a constant, which can be set to zero by an appropriate choice of the reference point of the energy [60,61]:

$$\left(\sum_i \left(-\frac{\hbar^2}{2m_0}\Delta_i\right) + \frac{1}{2}\sum_i \sum_{j\neq i} \frac{e^2}{r_{ij}} + U(\mathbf{r_1}, \mathbf{r_2}, \ldots, \mathbf{r_n}, \mathbf{R_{10}}, \mathbf{R_{20}}, \ldots, \mathbf{R_{N0}})\right)\psi_e = E_e\psi_e. \tag{5}$$

Eq. (5) describes the movement of interacting electrons in the field of stationary nuclei. In this equation the energy of electrons $E_e$ and their wave function $\psi_e$ depend only parametrically on the

coordinates of stationary nuclei $\mathbf{R_{\alpha 0}}$. In spite of significant simplifications, the Schrödinger equation in the form (5) could not be solved [60,61]. Therefore, further approximations are applied in order to reduce the number of variables. In the valence approximation Eq. (5) is written only for valence electrons that move in the potential field of stationary atomic cores (all remaining electrons with nuclei, i.e., ions) [60,61]. However, even with this approximation Eq. (5) could not be solved in the general form. The wave function of the system still depends on the coordinates of all valence electrons, which interact with one another. Therefore, the variables in Eq. (5) cannot be separated [60,61].

The many-electron task can be turned into the one-electron task by the Hartree–Fock method. In this method, the potential energy of the pairwise interaction of electrons $\frac{1}{2}\sum_i \sum_{j\neq i} \frac{e^2}{r_{ij}}$ is replaced by the potential energy in the form $\sum_i \Omega_i(\mathbf{r_i})$, where $\Omega_i(\mathbf{r_i})$ is the energy of the interaction between the $i$-th electron and the averaged field of all other electrons (the so called self-consistent field) [60,61]. Similarly, the potential energy of the interaction between electrons and nuclei $U(\mathbf{r_1}, \mathbf{r_2} \ldots)$ can be presented as the sum $\sum_i U_i(\mathbf{r_i})$, where $U_i(\mathbf{r_i})$ is the potential energy of the $i$-th electron in the field of all nuclei. Taking it into consideration, Eq. (5) is transformed into the following form [60,61]:

$$\left(\sum_i \left(-\frac{\hbar^2}{2m_0}\Delta_i + \Omega_i(\mathbf{r_i}) + U_i(\mathbf{r_i})\right)\right)\psi_e = E_e\psi_e. \tag{6}$$

This equation can be written as [60,61]:

$$\widehat{H}\psi_e = \left(\sum_i \widehat{H}_i\right)\psi_e = E_e\psi_e, \tag{7}$$

where $\widehat{H}_i$ is the Hamiltonian of the $i$-th electron.

As follows from Eq. (7), the Hamiltonian of the whole solid is the sum of the Hamiltonians of individual electrons. In this case, the wave function of the system of particles can be presented as the product of the one-electron wave functions [60,61]:

$$\psi_e(\mathbf{r_1}, \mathbf{r_2} \ldots) = \varphi_1(\mathbf{r_1})\varphi_2(\mathbf{r_2}) \ldots = \prod_i \varphi_i(\mathbf{r_i}). \tag{8}$$

Each wave function $\varphi_1(\mathbf{r_i})$ satisfies to the one-electron Schrödinger equation:

$$\widehat{H}_i\varphi_i = E_i\varphi_i, \tag{9}$$

in which the interaction between the $i$-th electron and other electrons is described with the potential $\Omega_i(\mathbf{r_i})$ [60,61].

Thus, the introduction of the self-consistent field allows turning the many-electron equation to a set of the one-electron equations. The electrons in the solid are considered as non-interacting particles, and the total energy of the system of particles equals the sum of the energies of individual electrons $E_e = \sum_i E_i$ [60,61].

If we introduce the potential energy of an electron in a crystal as the function $V(\mathbf{r})$:

$$V(\mathbf{r}) = U(\mathbf{r}) + \Omega(\mathbf{r}), \tag{10}$$

the Schrödinger equation can be written in the form [60–62]:

$$\left(-\frac{\hbar^2}{2m_0}\Delta + V(\mathbf{r})\right)\varphi(\mathbf{r}) = E\varphi(\mathbf{r}). \tag{11}$$

Because atoms are placed periodically in the crystal, the total potential of the crystal $V(\mathbf{r})$ will possess the three-dimensional periodicity of the crystal lattice [60–62].

F. Bloch proved that the wave function of an electron in the periodic field of a crystal is a plane wave that is modulated in amplitude with the periodicity of a crystal lattice and runs along the wave vector. The Bloch function (or wave) is defined by the equation:

$$\varphi_{\mathbf{k}}(\mathbf{r}) = e^{i\mathbf{k}\mathbf{r}}U_{\mathbf{k}}(\mathbf{r}), \tag{12}$$

where $e^{i\mathbf{kr}}$ is the plane wave that runs along the wave vector $\mathbf{k}$, which characterizes the quantum state of an electron in a crystal, $U_{\mathbf{k}}(\mathbf{r})$ is some periodic function with the period of a crystal lattice that depends on the wave vector $\mathbf{k}$ [59–62].

The substitution of the Bloch function (12) into the one-electron Schrödinger Eq. (9) gives the following equation [60,61]:

$$\widehat{H}\varphi_{\mathbf{k}}(\mathbf{r}) = E\varphi_{\mathbf{k}}(\mathbf{r}). \tag{13}$$

As follows from Eq. (13), the energy of an electron in a crystal depends on the wave vector $\mathbf{k}$.

Thus, the solution of the Schrödinger equation for an electron in the periodic field of a crystal is a running plane wave that is modulated with the periodicity of the crystal lattice. The dispersion of the energy of an electron in a crystal depends on the wave vector $\mathbf{k}$. Determining the dependence $E(\mathbf{k})$ is one of the central tasks in solid state physics.

### 2.2. Properties of the wave vector of electron in a crystal, Brillouin zones

The wave vector $\mathbf{k}$ that was introduced during discussion of the Bloch function of an electron in the periodic field of a crystal in the previous section, is analogues to the wave vector $\mathbf{k}$ of a free electron [60–62]. However, while the wave vector $\mathbf{k}$ of a free electron is proportional to the momentum $\mathbf{p}$ ($\mathbf{p} = \hbar\mathbf{k}$), the wave vector of an electron in a crystal is not proportional to the momentum. For an electron in the periodic field of a crystal, the quasi-momentum $\mathbf{P}$ is introduced: $\mathbf{P} = \hbar\mathbf{k}$. The energy of an electron in a crystal is a function of the quasi-momentum $E = E(\mathbf{P})$ [60–62].

While the wave vector $\mathbf{k}$ of a free electron is well defined, the wave vector $\mathbf{k}$ of an electron in a crystal is degenerate. The states that are characterized by the wave vector $\mathbf{k}$ and the wave vector $\mathbf{k} + \mathbf{K}$ are physically equivalent [60,62]. Here $\mathbf{K} = h\mathbf{b_1} + k\mathbf{b_2} + l\mathbf{b_3}$ is a vector of the reciprocal lattice, $h$, $k$, $l$ are integer numbers. The reciprocal lattice consists of a set of wave vectors $\mathbf{K}$ so that $e^{i\mathbf{KR}} = 1$ for all vectors $\mathbf{R}$ of the direct lattice. The reciprocal lattice is defined by three basis vectors $\mathbf{b_1} = 2\pi(\mathbf{a_2} \times \mathbf{a_3})/\mathbf{a_1} \cdot (\mathbf{a_2} \times \mathbf{a_3})$, $\mathbf{b_2} = 2\pi(\mathbf{a_3} \times \mathbf{a_1})/\mathbf{a_2} \cdot (\mathbf{a_3} \times \mathbf{a_1})$ and $\mathbf{b_3} = 2\pi(\mathbf{a_1} \times \mathbf{a_2})/\mathbf{a_3} \cdot (\mathbf{a_1} \times \mathbf{a_2})$, where $\mathbf{a_1}$, $\mathbf{a_2}$ and $\mathbf{a_3}$ are basis vectors of the direct lattice [62].

Thus, the wave function and energy of an electron in a crystal are periodic functions of the wave vector $\mathbf{k}$ with the period $\mathbf{K}$ (or the quasi-momentum $\mathbf{P}$ with the period $\hbar\mathbf{K}$) [60,62]:

$$\begin{aligned} E(\mathbf{k}) &= E(\mathbf{k} + \mathbf{K}), \\ E(\mathbf{P}) &= E(\mathbf{P} + \hbar\mathbf{K}). \end{aligned} \tag{14}$$

If the reciprocal lattice is built in $k$-space (or in $P$-space), all this space can be divided into volumes that contain physically equivalent states. These volumes are called Brillouin zones [60]. A polyhedron with a minimal volume that is built around the origin of coordinates in $k$- (or $P$-) space and contains all possible distinct states is called the first Brillouin zone [60]. The first Brillouin zone is the Wigner–Seitz cell for the reciprocal lattice. Any point in $k$- (or $P$-) space can be translated into the first Brillouin zone by vectors of the reciprocal lattice. Because states in different Brillouin zones are equivalent, it is enough to consider only the range of $\mathbf{k}$ values confined in the first Brillouin zone for a complete description of the whole set of all electronic states in a crystal [60].

The indexes $n$ are given to the energy states to denote the different solutions of the Schrödinger equation. At a specified $n$ the eigenfunctions and eigenvalues are periodic functions of the vector $\mathbf{k}$ [60,62]:

$$\begin{aligned} \varphi_{n,\mathbf{k}+\mathbf{K}}(\mathbf{r}) &= \varphi_{n,\mathbf{k}}(\mathbf{r}), \\ E_n(\mathbf{k} + \mathbf{K}) &= E_n(\mathbf{k}). \end{aligned} \tag{15}$$

By this way we come to the description of energy states of electrons in the periodic potential by a family of continuous functions $E_n(\mathbf{k})$, each of which has the periodicity of the reciprocal lattice [60,62]. These functions define the band structure of a crystalline solid. The collection of all energy states of electrons that are described by the function $E_n(\mathbf{k})$ at a fixed $n$ is called the energy band. Because each function $E_n(\mathbf{k})$ is periodic and continuous, it has upper and lower limits. Therefore, all energy states of a given energy band are confined within these two limits [60,62].

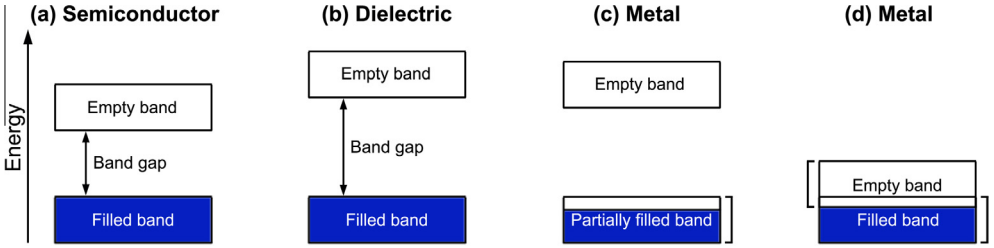


**Fig. 1.** The scheme of filling of energy bands with electrons in semiconductors, dielectrics and metals. In the case of semiconductors (a), the valence band is completely filled and is separated from the conduction band by the relatively narrow band gap. Because of thermal excitations, a tiny fraction of electrons is transferred to the conduction band, which causes the conduction of semiconductors. In the case of dielectrics (b), the completely filled valence band is separated from the next empty band by a large band gap. Electrons in the valence band cannot change their energy, therefore, dielectrics do not conduct the electric current. In the case of metals with the band structure (c), the valence band is partially filled. The external electric field initiates accelerating and moving electrons from the highest filled energy states to empty states of the same band, thus the electric current is induced in a crystal. In the case of metals with the band structure (d), the valence band is completely filled with electrons, but overlaps with the next empty allowed band. An external electric field initiates moving electrons to energy states of the empty band, i.e., the electric current is induced.

### *2.3. Filling of energy bands with electrons*

For every allowed **k** value, there are corresponding allowed energy states. According to the Pauli exclusion principle, two electrons with oppositely directed spins can occupy the same energy state. Consequently, a number of electrons in an allowed band that contains $N_0$ energy states cannot exceed $2N_0$ [60]. According to the number of electrons per unit cell of a crystal, different variants of filling of energy bands with electrons are possible. In semiconductors and dielectrics the highest completely filled band (the so-called valence band, because it is occupied by valence electrons) is separated from the lowest empty band (the so-called conduction band) by an energy gap (the so-called band gap) [60,62]. Solids with a band gap of less than ~3 eV belong to semiconductors (e.g. silicon). In semiconductors a number of electrons populate the conduction band due to thermal excitations, which causes the conductance. Solids with a band gap of more than ~3 eV are dielectrics (e.g. sodium chloride). In dielectrics the external electric field cannot induce an electric current, because electrons in the valence band can change neither their energy nor momentum [60,62].

In metals one or more energy bands are filled partially. In this case, the energy of the highest filled states (the so-called Fermi level) lies inside a range of the allowed energies of one or several bands. In *k*-space for each partially filled band there is a surface that separates filled and unfilled states [60,62]. All these surfaces together are called the Fermi surface. The parts of the Fermi surface that correspond to individual partially filled bands are called the pockets of the Fermi surface [60,62]. The examples of crystals with the partially filled valence band are alkali metals. Metals are also crystals where the valence band is completely filled with electrons, but overlaps with the next empty allowed band. This is the case in alkali-earth metals [60].

Fig. 1 shows the scheme that illustrates the filling of energy bands with electrons in semiconductors, dielectrics and metals.

In general, the population of energy bands with electrons depends on the electronic configuration of atoms that form a crystal, nature of chemical bonds and also the crystal structure [60].

### *2.4. Density of states, Fermi–Dirac distribution*

The population of energy bands with electrons defines electrical and transport properties of solids. In order to calculate the density of electrons, the density of states and the probability of electrons being present at these states should be known. The density of states $D(E)$ is the number of states per unit interval of energy for unit volume of a crystal. It can be written as

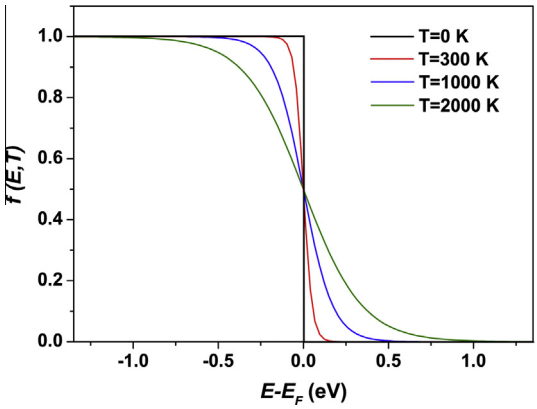


**Fig. 2.** The plot of the Fermi–Dirac distribution function $f(E, T)$ at temperatures of 0 K, 300 K, 1000 K and 2000 K. At absolute zero, the function $f(E, T)$ changes stepwise from 1 (filled states) to 0 (empty states) when the energy equals the Fermi energy. At temperatures of 300 K, 1000 K and 2000 K, the function $f(E, T)$ changes continuously from 1 to 0 in an ever broader energy range around the Fermi energy.

$$D(E) = \frac{dZ}{dE}, \tag{16}$$

where $dZ$ is the number of states per interval of energy from $E$ to $E + dE$ in a crystal with unit volume [61,62]. If the probability of an electron being present at a state with the energy $E$ is $f(E, T)$, the number of electrons $dn$ being present at states $dZ$ can be defined in the following form [61,62]:

$$dn = f(E,T)dZ = f(E,T)D(E)dE. \tag{17}$$

Consequently, the number of electrons, for which the energy lies in the interval from $E_1$ to $E_2$ equals:

$$n = \int_{E_1}^{E_2} f(E,T)D(E)dE. \tag{18}$$

The total number of electrons per unit volume is obtained by setting $E_1$ to $-\infty$ and $E_2$ to $+\infty$.

In thermodynamic equilibrium thermal excitations of electrons, which are particles with half-integer spin and obey the Pauli exclusion principle, are characterized by the Fermi–Dirac distribution. The probability of an electron being present at a given state with the energy $E$ at temperature $T$, i.e., the distribution function $f(E, T)$ is described by the following formula [59,61,62]:

$$f(E,T) = \frac{1}{e^{(E-E_F)/k_BT} + 1}, \tag{19}$$

where $k_B$ is the Boltzmann constant, $T$ is the absolute temperature and $E_F$ is the Fermi energy.

As follows from Eq. (19), at temperature $T = 0$, when the energy $E < E_F$, the function $f(E, T = 0)$ amounts to 1. When $E > E_F$, the function $f(E, T = 0)$ becomes 0. It means that all states with the energy smaller than the Fermi energy are occupied with electrons and states with the energy larger than the Fermi energy are empty. Thus, the Fermi energy is the maximal possible energy of electrons in metals at absolute zero temperature [59,61,62].

At temperature $T > 0$ and energy $E = E_F$, the function $f(E, T)$ equals 0.5. Therefore, the Fermi level is the energy level for which the possibility of filling with electrons at the non-zero temperature amounts to 0.5. At temperature $T > 0$, as a result of the thermal motion, a part of electrons will go to states with the energy larger than the Fermi energy ($E > E_F$) and, consequently, some states below the Fermi level turn out to be empty. In this case, the number of electrons that go to higher energy levels balances the number of holes with the energies $E < E_F$ [61].

Fig. 2 demonstrates the plot of the Fermi–Dirac distribution function at different temperatures. At temperature $T = 0$, the function $f(E, T)$ changes stepwise from the value of 1 (filled states) to the value

of 0 (empty states) when the energy $E = E_F$. At finite temperature $T > 0$, the function $f(E, T)$ changes continuously from 1 to 0 in an energy range around $E = E_F$. This energy range increases with raising the temperature.

### 2.5. Comparison of electrical properties of metals, semiconductors and dielectrics

Because of the high density of conduction electrons, metals possess large electric conductivity ($10^4$–$10^6\ \Omega^{-1}\ cm^{-1}$ [60]). The electric conductivity of intrinsic semiconductors (without impurities) at $T = 0$ K is zero, because there are no free charge carriers. At temperature $T > 0$ K, as a result of the thermal motion, a fraction of electrons is transferred from the valence band to the conduction band, and holes are formed in the valence band. Due to two competitive processes (generation of charge carriers and their recombination), there is an equilibrium density of charge carriers. As a result, the electric conductivity of semiconductors is $10^4$–$10^{-10}\ \Omega^{-1}\ cm^{-1}$ [60]. At the same time, the electric conductivity may be influenced by impurities and defects in semiconductor crystals. There are no free charge carriers in dielectrics, therefore they do not conduct the current. Their electric conductivity is $10^{-10}$–$10^{-22}\ \Omega^{-1}\ cm^{-1}$ [60]. The mentioned values of the electric conductivity correspond to room temperature.

The temperature dependence of the conductivity is different for metals, semiconductors and dielectrics. In the case of metals, the conductivity increases linearly with lowering the temperature. At temperatures near absolute zero, the conductivity of many metals stops changing and has some constant value [60]. Some metals change to the superconducting state due to the Cooper pairing at temperatures near zero, which is characterized by the complete loss of the electric resistance and ideal diamagnetism.

As it was discussed above, the Bloch function (12) of electrons in a crystal is a running wave that is modulated with the period of the crystal lattice. It means that the Bloch wave runs in principle through an ideal crystal without damping. In the case of disturbance of the ideal periodicity in the crystal, the Bloch function does not satisfy the Schrödinger equation anymore, and electrons are scattered. The mean free path becomes finite, which leads to a finite value of the electric conductivity or resistance [60]. The disturbance of the ideal periodicity may be caused by impurities, defects, crystal surfaces and thermal atomic oscillations (phonons) [60]. The main scattering mechanism of electrons at high temperatures is the scattering by phonons. The temperature dependence of the conductivity is defined by the temperature dependencies of the density of conduction electrons and their mobility (because $\sigma = en\mu_n$, where $\sigma$ is the conductivity, $n$ is the density of electrons, $\mu_n$ is the mobility of electrons, $e$ is the charge of electrons). Because the density of electrons in metals does not depend on temperature, at high temperatures the electric conductivity of metals decreases due to decrease of the electron mobility [60]. At low temperatures, the scattering of electrons by impurities and defects start to dominate. In this case, the electron mobility in metals does not depend on the temperature. Therefore, at low temperatures the conductivity becomes constant [60].

In intrinsic semiconductors the density of charge carriers increases exponentially with raising the temperature. The temperature dependence of the conductivity is defined by the temperature dependencies of the density of charge carriers and their mobility (because $\sigma = en\mu_n + ep\mu_p$, where $p$ is the density of holes, $\mu_p$ is the mobility of holes). The charge carriers are scattered by phonons, and their mobility decreases with raising the temperature. As a result, the conductivity of intrinsic semiconductors grows exponentially with increasing the temperature [60].

In dielectrics, as in intrinsic semiconductors, the electric conductivity increases exponentially with the temperature [60]. If there are impurity atoms, free charge carriers may appear as a result of the thermal activation of impurity levels. However, due to the low density of charge carriers, the electric conductivity of dielectrics is significantly smaller than the values for semiconductors. Besides, the mobility of charge carriers is very low in most dielectrics. Electrons and holes are strongly bounded to the crystal lattice and form polarons, which leads to the polaron conductivity [60]. In some dielectrics the ionic conduction dominates, where the current is conducted by cations and anions, and in the electrostatic field there is the transport of charge and matter [60].

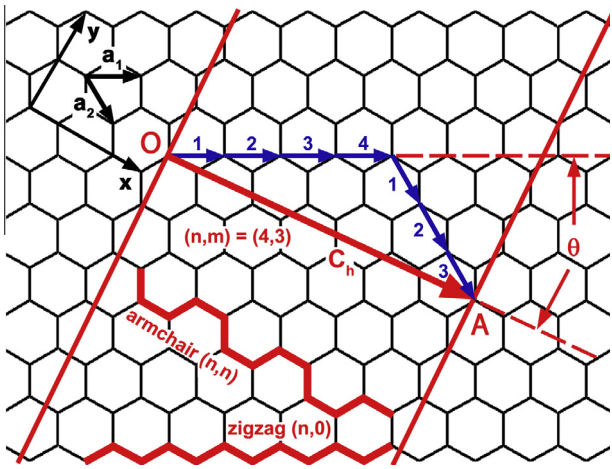


**Fig. 3.** Schematic hexagonal structure of a two-dimensional graphene sheet with the lattice vectors $\mathbf{a_1}$ and $\mathbf{a_2}$ in real space. The rolling of the graphene sheet along the chiral vector $\mathbf{C_h} = 4\mathbf{a_1} + 3\mathbf{a_2}$ (the construction of the vector is shown with numbers) connects two crystallographically equivalent sites O and A and forms the nanotube with the (4,3) chirality. The vector $\mathbf{C_h}$ is perpendicular to the SWCNT axis. The chiral angle $\theta$ is the angle between the vectors $\mathbf{C_h}$ and $\mathbf{a_1}$. In zigzag nanotubes with a $(n,0)$ chirality $\theta = 0°$ and a third of the C–C bonds are parallel to the nanotube axis, whereas in armchair nanotubes with a $(n,n)$ chirality $\theta = 30°$ and a third of the C–C bonds are perpendicular to the SWCNT axis. Figure is redrawn with modifications from Ref. [64].

## 3. Band structure and electronic properties of single-walled carbon nanotubes

### *3.1. Atomic structure and its correlation with electronic structure of SWCNTs*

The SWCNTs are unique nanoscale objects, because their electronic structure and properties are defined by the atomic structure [2,63]. Therefore, before description of peculiarities of the band structure of SWCNTs, a brief overview of their geometric structure is presented.

A cylindrical one-dimensional structure of single-walled carbon nanotubes is geometrically obtained by rolling up a honeycomb graphene sheet [2], as illustrated in Fig. 3. The vector along which the rolling takes place is called the chiral vector ($\mathbf{C_h}$). It connects two crystallographically equivalent sites on a graphene layer (O and A in Fig. 3). The chiral vector is defined by the following equation:

$$\mathbf{C_h} = n\mathbf{a_1} + m\mathbf{a_2} \equiv (n, m), \tag{20}$$

where $\mathbf{a_1}$ and $\mathbf{a_2}$ are the basis vectors of the hexagonal graphene lattice, and $n$, $m$ are integer numbers ($0 \leqslant m \leqslant n$) that are called the chirality indexes [2]. The basis vectors are expressed in the $x$ and $y$ coordinates in real space as:

$$\mathbf{a_1} = \left(\frac{\sqrt{3}}{2}, \frac{1}{2}\right)a, \quad \mathbf{a_2} = \left(\frac{\sqrt{3}}{2}, -\frac{1}{2}\right)a, \tag{21}$$

where $a$ is the lattice parameter of the graphene layer, $a = \sqrt{3}a_{c-c} \approx 0.246$ nm, $a_{c-c}$ is the nearest-neighbor carbon–carbon distance, $a_{c-c} \approx 0.142$ nm [2].

The chiral vector $\mathbf{C_h} = (n,m)$ defines the chiral angle $\theta$ of a nanotube with $(n,m)$ chirality. This is the angle between the vectors $\mathbf{C_h}$ and $\mathbf{a_1}$, and it can be calculated by the formula [2]:

$$\cos\theta = \mathbf{C_h} \cdot \mathbf{a_1} / |\mathbf{C_h}||\mathbf{a_1}| = \frac{2n + m}{2\sqrt{n^2 + nm + m^2}}, \tag{22}$$

where $0 \leqslant |\theta| \leqslant 30°$, because of the hexagonal symmetry of the graphene lattice (Fig. 3).

Depending on the chiral vector and chiral angle, the structure of SWCNTs can be classified to three types [2,63]:

1. Zigzag nanotubes ($n$,0), where $\theta = 0°$ and a third of the C–C bonds are parallel to the nanotube axis.
2. Armchair nanotubes ($n$,$n$), where $\theta = 30°$ and a third of the C–C bonds are perpendicular to the SWCNT axis.
3. Chiral nanotubes ($n$,$m$), where $0 < |\theta| < 30°$.

Fig. 4 demonstrates the atomic structures of (12,0) zigzag, (6,6) armchair and (6,4) chiral SWCNTs [63].

The diameter of nanotube ($d_t$) is defined by the chiral vector:

$$d_t = L/\pi = |\mathbf{C_h}|/\pi = \frac{a}{\pi}\sqrt{n^2 + nm + m^2}, \tag{23}$$

where $L$ is the circumferential length of the nanotube [2].

The unit cell of nanotube depends on the translational vector **T**. This is the smallest vector that is parallel to the SWCNT axis and is perpendicular to the chiral vector $\mathbf{C_h}$ in the unrolled graphene lattice. It can be written in the following form:

$$\mathbf{T} = t_1\mathbf{a_1} + t_2\mathbf{a_2} \equiv (t_1, t_2), \tag{24}$$

where $t_1$, $t_2$ are integer numbers, $gcd(t_1,t_2) = 1$, $gcd(t_1,t_2)$ is the greatest common divisor of $t_1$ and $t_2$. Taking into consideration that $\mathbf{C_h} \cdot \mathbf{T} = 0$, the expressions for $t_1$ and $t_2$ can be written as $t_1 = (2m + n)/d_R$ and $t_2 = -(2n + m)/d_R$, where $d_R = gcd(2m + n, 2n + m)$ [2].

The translational period $t$ along the nanotube axis can be calculated as [2]:

$$t = |\mathbf{T}| = \frac{\sqrt{3}L}{d_R} = \frac{\sqrt{3}a\sqrt{n^2 + nm + m^2}}{d_R}. \tag{25}$$

The unit cell of nanotube is defined by the chiral vector $\mathbf{C_h}$ and the translational vector **T**, while the unit cell of the graphene lattice is determined by the basis vectors $\mathbf{a_1}$ and $\mathbf{a_2}$. The number of hexagons per unit cell of nanotube $N$ can be presented by the formula [2]:

$$N = |\mathbf{C_h} \times \mathbf{T}|/|\mathbf{a_1} \times \mathbf{a_2}| = \frac{2(n^2 + nm + m^2)}{d_R} = \frac{2L^2}{a^2 d_R}. \tag{26}$$

Because each hexagon contains two carbon atoms, there are $2N$ atoms per unit cell of nanotube.

Early theoretical calculations [65–67], which were done right after the discovery of carbon nanotubes, showed that their electronic properties are very sensitive to the atomic structure. Depending on the atomic structure, SWCNTs can have metallic or semiconducting properties. In particular, all armchair nanotubes ($n$,$n$) are metallic, whereas zigzag and chiral SWCNTs can be either metallic or semiconducting, which depends on the $n$ and $m$ chiral indexes and relations between them. These differences arise from the different Brillouin zones and band structures of zigzag, armchair and chiral nanotubes, which are discussed in the following sections.

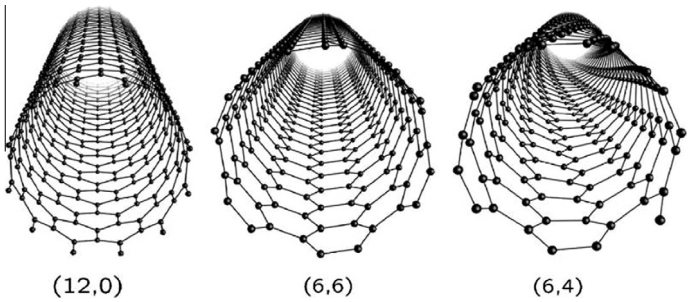


**Fig. 4.** Schematic representation of the atomic structures of three types of SWCNTs: zigzag (12,0), armchair (6,6) and chiral (6,4) nanotubes. Black balls correspond to carbon atoms, and connecting lines correspond to the C–C bonds. Reprinted figure with permission from Charlier JC et al. Rev Mod Phys 2007;79:677. Copyright 2007 by the American Physical Society [63].

### 3.2. Brillouin zone of SWCNTs

Because the atomic structure of SWCNTs is geometrically described as a rolled-up graphene sheet, the Brillouin zone of nanotubes can be derived from the Brillouin zone of graphene.

The unit cell of the hexagonal graphene lattice is defined by the basis vectors $\mathbf{a_1}$ and $\mathbf{a_2}$ in real space, which are expressed by Eq. (21) in the $x$ and $y$ coordinates. This is a rhombus that contains two carbon atoms (Fig. 5a). The reciprocal lattice of graphene is defined by the basis vectors $\mathbf{b_1}$ and $\mathbf{b_2}$ in reciprocal space, which can be presented in the $x$ and $y$ coordinates as [2]:

$$\mathbf{b_1} = \left(\frac{1}{\sqrt{3}}, 1\right)\frac{2\pi}{a}, \quad \mathbf{b_2} = \left(\frac{1}{\sqrt{3}}, -1\right)\frac{2\pi}{a}. \tag{27}$$

The first Brillouin zone of graphene is a hexagon with three high symmetry points: Γ in the center, K at the corners and M at the middle of edges [2], as illustrated in Fig. 5b.

As was mentioned above, the unit cell of SWCNTs is defined by the chiral vector $\mathbf{C_h}$ and the translational vector $\mathbf{T}$. The corresponding vectors of the reciprocal lattice are $\mathbf{K_1}$ along the circumference and $\mathbf{K_2}$ along the axis of nanotube. Taking into consideration the relation $\mathbf{R_i} \cdot \mathbf{K_j} = 2\pi\delta_{ij}$ between the lattice vectors in real space $\mathbf{R_i}$ and the vectors in reciprocal space $\mathbf{K_j}$, it can be written [2]:

$$\begin{aligned} &\mathbf{C_h} \cdot \mathbf{K_1} = 2\pi, \quad \mathbf{T} \cdot \mathbf{K_1} = 0, \\ &\mathbf{C_h} \cdot \mathbf{K_2} = 0, \quad \mathbf{T} \cdot \mathbf{K_2} = 2\pi. \end{aligned} \tag{28}$$

Then the reciprocal lattice vectors $\mathbf{K_1}$ and $\mathbf{K_2}$ of a $(n,m)$ nanotube, which has the chiral vector $\mathbf{C_h} = (n,m)$, the translational vector $\mathbf{T} = (t_1,t_2)$ and $N$ hexagons per unit cell, can be expressed through the reciprocal lattice vectors of graphene $\mathbf{b_1}$ and $\mathbf{b_2}$ in the following form [2]:

$$\mathbf{K_1} = \frac{1}{N}(-t_2\mathbf{b_1} + t_1\mathbf{b_2}), \quad \mathbf{K_2} = \frac{1}{N}(m\mathbf{b_1} - n\mathbf{b_2}). \tag{29}$$

Because of the one-dimensional structure of SWCNTs, only the vector $\mathbf{K_2}$ remains continuous (for a nanotube of infinite length). The quantization of vector $\mathbf{K_1}$ as a result of the periodic boundary conditions on the chiral vector of nanotube gives a set of discrete one-dimensional $k$ vectors. Since $N\mathbf{K_1} = -t_2\mathbf{b_1} + t_1\mathbf{b_2}$ corresponds to a reciprocal lattice vector of graphene, the wave vectors with a difference of $N\mathbf{K_1}$ are equivalent. The $N$ wave vectors $\mu\mathbf{K_1}$ ($\mu = -N/2 + 1, \ldots, N/2$) result in $N$ discrete one-dimensional $k$ vectors [2].

Thus, the first Brillouin zone of nanotubes is a set of $N$ parallel lines with the length of $|\mathbf{K_2}|$ that are separated by the distance $|\mathbf{K_1}|$ [2,68]. The lengths of the vectors $\mathbf{K_1}$ and $\mathbf{K_2}$ are given by the formulas [68]:

$$|\mathbf{K_1}| = 2/d_t, \quad \text{and} \quad |\mathbf{K_2}| = 2\pi/|\mathbf{T}| = 2d_R/\sqrt{3}d_t. \tag{30}$$

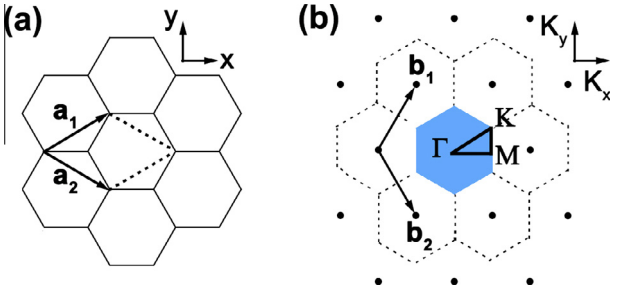


**Fig. 5.** (a) The unit cell (the dotted rhombus, containing two carbon atoms) of hexagonal graphene lattice defined by the basis vectors $\mathbf{a_1}$ and $\mathbf{a_2}$ in real space. (b) The reciprocal lattice of graphene (dashed hexagons) with the basis vectors $\mathbf{b_1}$ and $\mathbf{b_2}$ and the first Brillouin zone of graphene (light blue hexagon) with three high symmetry points Γ, K and M (connected by the black triangle). Bold dots correspond to Γ points.

The first Brillouin zone of SWCNTs is described by the reciprocal vector **K** as follows:

$$\mathbf{K} = k\mathbf{K_2}/|\mathbf{K_2}| + \mu\mathbf{K_1}, \tag{31}$$

where $\mu = -N/2 + 1, \ldots, N/2$ and $-\pi/|\mathbf{T}| < k < \pi/|\mathbf{T}|$.

Fig. 6 compares the first Brillouin zone of armchair (7,7), zigzag (11,0) and chiral (6,3) nanotubes. The first Brillouin zone of a (7,7) SWCNT (Fig. 6a) includes 14 lines. They are parallel to the nanotube axis. The length of the vector $\mathbf{K_2}$, which defines the length of the first Brillouin zone, is $2\pi/a$. The first Brillouin zone of a zigzag (11,0) SWCNT (Fig. 6b) includes 22 lines. The length of the first Brillouin zone is $2\pi/\sqrt{3}a$. The comparison of the first Brillouin zones of armchair and zigzag nanotubes with the first Brillouin zone of chiral nanotube (6,3) (Fig. 6c) shows that the latter includes more number of lines – 42. Taking into consideration that every discrete value of $k$ vector gives rise to a one-dimensional energy band, one can conclude that the band structure of a chiral nanotube can contain a large number of energy bands.

### 3.3. From band structure of graphene to SWCNTs

The one-dimensional energy dispersion relations of SWCNTs are derived from those of graphene, considering the first Brillouin zone of nanotubes.

Every carbon atom of a graphene layer has four valence orbitals ($2s$, $2p_x$, $2p_y$ and $2p_z$). The ($s$, $p_x$, $p_y$) orbitals form together in-plane σ (bonding or occupied) and σ* (antibonding or unoccupied) orbitals. The σ-bonds between carbon atoms are strong covalent bonds, which define most of the binding energy and elastic properties of graphene [63]. The remaining $p_z$ orbitals, perpendicular to the graphene plane, interact with neighboring $p_z$ orbitals, which creates delocalized $\pi$ (bonding) and $\pi^*$ (antibonding) orbitals [2,63]. The bonding σ and antibonding σ* bands are separated by a large energy gap, and they are not considered for calculation of the band structure of graphene. At the same time, the binding $\pi$ (last valence) and antibonding $\pi^*$ (first conduction) bands cross at the K points of the first Brillouin zone, and they define the low energy electronic properties of graphene [2,63].

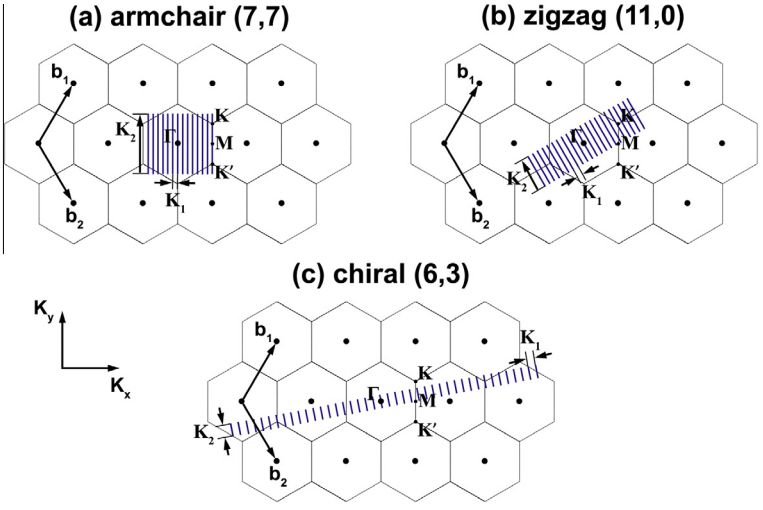


**Fig. 6.** The first Brillouin zone of (7,7) armchair (a), (11,0) zigzag (b) and (6,3) chiral (c) nanotubes, which is a set of $N$ parallel lines with the length of $|\mathbf{K_2}|$ separated by the distance $|\mathbf{K_1}|$. $\mathbf{K_1}$ and $\mathbf{K_2}$ are vectors in the reciprocal graphene lattice (shown by hexagons) with the basis vectors $\mathbf{b_1}$ and $\mathbf{b_2}$. They correspond, respectively, to the chiral vector $\mathbf{C_h}$ and translational vector $\mathbf{T}$ that define the unit cell of SWCNTs in real space. The first Brillouin zone of graphene with three high symmetry points Γ, K and M is shown for comparison. Bold dots in the center of every hexagon mark Γ points.

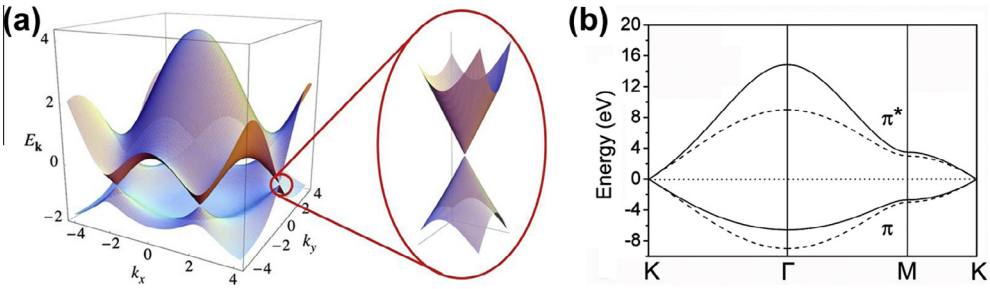


**Fig. 7.** (a) The energy dispersion relations for graphene as a function of the two-dimensional wave vector **k** throughout the whole first Brillouin zone. The antibonding $\pi^*$ band (upper part) and the bonding $\pi$ band (lower part) cross at the K points which corresponds to the Fermi energy. The zoom in demonstrates the cone shapes of the energy bands near the Fermi energy. Reprinted figure with permission from Castro Neto AH et al. Rev Mod Phys 2009;81:109. Copyright 2009 by the American Physical Society [70]. (b) The energy dispersion relations along the perimeter of the triangle ΓMK. The asymmetric dispersion relations (solid line) has the parameters $\varepsilon_{2p} = 0$, $\gamma_0 = 3.033$ eV and $s = 0.129$, and symmetric dispersion relations (dashed line) has the parameter $s = 0$. The data are replotted from Refs. [2,71].

The two-dimensional energy dispersion relations of graphene are calculated [2] within the tight-binding model by solving the eigenvalue problem for a $(2 \times 2)$ Hamiltonian $\mathcal{H}$ and a $(2 \times 2)$ overlap integral matrix $S$, associated with the two inequivalent atoms of a graphene sheet [2,68,69]:

$$\mathcal{H} = \begin{pmatrix} \varepsilon_{2p} & -\gamma_0 f(k) \\ -\gamma_0 f(k)^* & \varepsilon_{2p} \end{pmatrix} \quad \text{and} \quad S = \begin{pmatrix} 1 & sf(k) \\ sf(k)^* & 1 \end{pmatrix}, \tag{32}$$

where $\varepsilon_{2p}$ is the site energy of the $2p$ atomic orbital, $\gamma_0$ is the nearest-neighbor carbon–carbon interaction energy, $s$ is the tight-binding overlap integral of the electronic wave function on adjacent sites, and the function $f(k)$ is written as:

$$f(k) = e^{ik_x a/\sqrt{3}} + 2e^{-ik_x a/2\sqrt{3}} \cos\left(\frac{k_y a}{2}\right). \tag{33}$$

Solving the secular equation $\det(\mathcal{H} - ES) = 0$ with $\mathcal{H}$ and $S$ from Eq. (32) gives the eigenvalues $E(\mathbf{k})$ as a function of $w(\mathbf{k})$ [2,68,69]:

$$E^{\pm}_{g2D}(\mathbf{k}) = (\varepsilon_{2p} \pm \gamma_0 w(\mathbf{k}))/(1 \mp s w(\mathbf{k})). \tag{34}$$

Here $E^+$ and $E^-$ correspond to the valence $\pi$ and the conduction $\pi^*$ energy bands, respectively. The function $w(\mathbf{k})$ has the following form:

$$w(\mathbf{k}) = \sqrt{1 + 4\cos\left(\frac{\sqrt{3}k_x a}{2}\right)\cos\left(\frac{k_y a}{2}\right) + 4\cos^2\left(\frac{k_y a}{2}\right)}. \tag{35}$$

It follows from Eq. (34) that the $\pi$ and $\pi^*$ bands become symmetrical around $E = \varepsilon_{2p}$, when the overlap integral $s$ becomes 0. In this case, the energy dispersion relations are presented as [2]:

$$E^{\pm}_{g2D}(k_x, k_y) = \pm\gamma_0 \sqrt{1 + 4\cos\left(\frac{\sqrt{3}k_x a}{2}\right)\cos\left(\frac{k_y a}{2}\right) + 4\cos^2\left(\frac{k_y a}{2}\right)}. \tag{36}$$

Fig. 7a demonstrates the energy dispersion relations for graphene as a function of the two-dimensional wave vector **k** throughout the whole first Brillouin zone [70]. The upper part of the diagram describes the antibonding $\pi^*$ band and the lower part is the bonding $\pi$ band. They degenerate at the K points of the first Brillouin zone where the Fermi energy lies. The bands have the cone shapes near the Fermi energy, which is shown in the zoomed part of the diagram. Since the occupied and unoccupied bands cross, the graphene shows a metallic (zero-energy gap) behavior [2,63,70].

However, because the Fermi surface is of zero dimension (it is a set of points), the term semimetal is used [63]. Fig. 7b demonstrates the energy dispersion relations of graphene along the perimeter of the triangle ΓMK [2,71]. The parameters $\varepsilon_{2p} = 0$, $\gamma_0 = 3.033$ eV and $s = 0.129$ were used for the asymmetric dispersion relations (solid line) and $s = 0$ for symmetric dispersion relations (dashed line). In the region near the K point the asymmetric and symmetric dispersion relations are in good agreement, and the energy difference between $\pi$ and $\pi^*$ bands are almost the same for them up to the energy of about 6 eV. It allows using symmetric dispersion relations of graphene to obtain a simple approximation for the electronic dispersion relations of nanotubes [2].

The energy dispersion relations of SWCNTs are obtained by considering the two-dimensional symmetric energy dispersion relations of graphene in the domain of the first Brillouin zone of nanotubes (the so-called zone-folding approximation) [2,63,68,69]. Taking into account Eq. (31) for the wave vector of the first Brillouin zone of SWCNTs, the one-dimensional energy dispersion relations of nanotubes are written in the following form [2,68,69]:

$$E_{1D}^{\pm}(k) = E_{g2D}^{\pm}(k\mathbf{K_2}/|\mathbf{K_2}| + \mu\mathbf{K_1}), \tag{37}$$

where $\mu = -N/2 + 1, \ldots, N/2$ and $-\pi/|\mathbf{T}| < k < \pi/|\mathbf{T}|$. The $N$ pairs of energy dispersion relations given by Eq. (37) correspond to the cross sections of the energy dispersion surface of graphene shown in Fig. 7a, where cuts are made on the lines $k\mathbf{K_2}/|\mathbf{K_2}| + \mu\mathbf{K_1}$ [2,68,69]. The number of energy dispersion relations in the energy bands of SWCNTs is defined by the number of the cutting lines.

Depending on the chirality $(n,m)$ of nanotube and, consequently, the number of the cutting lines, they can either pass through the K point of the two-dimensional first Brillouin zone of graphene or miss it. If the cutting line crosses the K point, then the one-dimensional energy bands of a nanotube have a zero energy gap, and the SWCNT is metallic. If the cutting lines do not cross the K point, then the nanotube is semiconducting with a finite energy gap [2,68,69]. From geometrical reasons, for a particular $(n,m)$ nanotube the cutting line passes through the K point when $(n - m)$ is a multiple of 3, and it happens for the third of nanotubes $(n,m)$ [2,68]. Therefore, the third of SWCNTs where $(n - m) = 3l$ ($l$ is an integer number) are metallic, and the other two third of nanotubes where $(n - m) \neq 3l$ are semiconducting. Thus, all armchair nanotubes $(n,n)$ are metallic, and zigzag nanotubes $(n,0)$ are only metallic when $n = 3l$ [2,63,68]. As an example, the discussed above Fig. 6 with the first Brillouin zones of (7,7) armchair, (11,0) zigzag and (6,3) chiral nanotubes can be considered. It is seen in Fig. 6 that the cutting lines pass through the K point for the (7,7) armchair nanotube ($(n - m) = 0$) and the (6,3) chiral SWCNT ($(n - m) = 3$), whereas they miss it for the (11,0) zigzag nanotube ($(n - m) \neq 3l$). As a result, the (7,7) and (6,3) SWCNTs are metallic, and the (11,0) nanotube is semiconducting.

### 3.4. Electronic structure of armchair and zigzag SWCNTs

To get the energy dispersion relations for armchair and zigzag nanotubes, we use the expression for the symmetric energy dispersion relations of graphene given in Eq. (36), considering the periodic boundary conditions around the circumference of a nanotube.

According to the appropriate periodic boundary conditions for the armchair $(n,n)$ SWCNT, the allowed wave vectors $k_{x,q}$ in the circumferential direction are defined by the expression [2]:

$$n\sqrt{3}k_{x,q}a = 2\pi q, \tag{38}$$

where $q = 1, \ldots, 2n$ ($q$ is an integer number).

Substitution of the values for the wave vectors $k_{x,q}$ into Eq. (36) leads to the following formula for the energy dispersion relations of armchair $(n,n)$ nanotubes:

$$E_q^{armchair}(k) = \pm\gamma_0\sqrt{1 + 4\cos\left(\frac{ka}{2}\right)\cos\left(\frac{q\pi}{n}\right) + 4\cos^2\left(\frac{ka}{2}\right)}, \tag{39}$$

where $q = 1, \ldots, 2n$ stems from the discrete part of the wave vector and $k$ is the continuous part of the one-dimensional wave vector along the SWCNT axis. The vector $k$ changes in the range $-\frac{\pi}{a} < k \leqslant \frac{\pi}{a}$. The

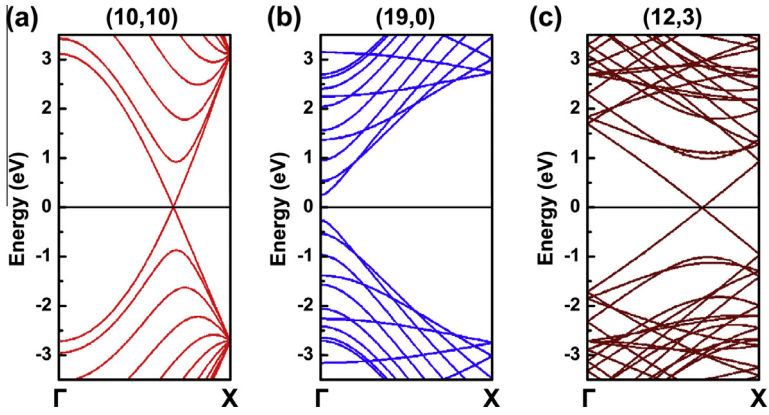


**Fig. 8.** Band structures of (10,10) armchair (a), (19,0) zigzag (b) and (12,3) chiral (c) SWCNTs, represented along the ΓX direction. They were obtained by the nearest-neighbor tight-binding calculation with $\gamma_0 = 2.7$ eV. The Fermi level is positioned at zero energy. For the (10,10) nanotube (a), the valence and conduction bands cross on the Fermi level at $k = \frac{2\pi}{3a}$, which is the point located at two-thirds of the distance between the center of the first Brillouin zone ($k = 0$, Γ point) to the zone boundary ($k = \frac{\pi}{a}$, X point). As a result, the (10,10) SWCNT has metallic properties. Moreover, the energy bands show a large degeneracy at the zone boundary (X point). For the (19,0) nanotube (b), the valence and conduction bands do not cross within the ΓX direction (from $k = 0$ to the zone boundary at $k = \frac{\pi}{\sqrt{3}a}$). There is a finite energy gap at the Γ point. As a result, the (19,0) SWCNT has semiconducting properties. For the (12,3) nanotube (c), the valence and conduction bands cross at $k = 2\pi/3|\mathbf{T}|$, which is at two-thirds of the distance between the zone center ($k = 0$, Γ point) to the zone boundary at $k = \pi/|\mathbf{T}|$ (X point). As a result, the (12,3) SWCNT shows a metallic behavior. The data are replotted from Ref. [72].

points $k = \pm\frac{\pi}{a}$ correspond to the edges of the first Brillouin zone of armchair nanotubes, which are labeled *X* [2,63].

According to calculations, for the (*n*,*n*) armchair nanotubes there are 4*n* energy subbands, described by Eq. (39), with 2*n* valence and 2*n* conduction bands [2].

In the points $k = \pm\frac{\pi}{a}$ the energy dispersion relations given in Eq. (39) are represented as:

$$E_q^{armchair}\left(k = \pm\frac{\pi}{a}\right) = \pm\gamma_0. \tag{40}$$

This means that for the armchair (*n*,*n*) nanotubes all energy bands are degenerate at the Brillouin zone boundaries (at the X points) [2,63].

The valence and conduction bands of all armchair SWCNTs cross at $k = \pm\frac{2\pi}{3a}$, at points that are located at two-thirds of the distance between the zone center ($k = 0$, Γ point) to the zone boundaries [2,63]. Indeed, in the points $k = \pm\frac{2\pi}{3a}$ the energy dispersion relations in Eq. (39) turn into the following form:

$$E_q^{armchair}\left(k = \pm\frac{2\pi}{3a}\right) = \pm\gamma_0\sqrt{2 + 2\cos\left(\frac{q\pi}{n}\right)}. \tag{41}$$

This means that the highest valence band and the lowest conduction band degenerate at this k point, where the bands cross the Fermi level, when $q = n$ for all *n* values. Thus, all armchair (*n*,*n*) nanotubes have metallic properties.

The typical band structure of armchair nanotubes is illustrated in Fig. 8a by an example of the band structure of the (10,10) nanotube, represented along the ΓX direction [72].

The energy dispersion relations of zigzag (*n*,0) SWCNTs can be obtained by writing the appropriate periodic boundary conditions on the wave vector $k_y$ in the circumferential direction [2]:

$$nk_{y,q}a = 2\pi q, \tag{42}$$

where $q = 1, \ldots, 2n$ (*q* is an integer number).

Substitution of the discrete allowed values $k_{y,q}$ into Eq. (36) yields the energy dispersion relations for the $4n$ energy subbands of the $(n,0)$ zigzag nanotubes:

$$E_q^{zigzag}(k) = \pm\gamma_0\sqrt{1 + 4\cos\left(\frac{\sqrt{3}ka}{2}\right)\cos\left(\frac{q\pi}{n}\right) + 4\cos^2\left(\frac{q\pi}{n}\right)}, \tag{43}$$

where $q = 1, \ldots, 2n$ and the one-dimensional wave vector $k$ along the SWCNT axis changes in the range $-\frac{\pi}{\sqrt{3}a} < k \leqslant \frac{\pi}{\sqrt{3}a}$. The points $k = \pm\frac{\pi}{\sqrt{3}a}$ correspond to the edges of the first Brillouin zone of zigzag nanotubes (X points) [2].

In the zone center ($k = 0$, $\Gamma$ point) the energy dispersion relations given in Eq. (43) are written as:

$$E_q^{zigzag}(k = 0) = \pm\gamma_0\left(1 + 2\cos\left(\frac{q\pi}{n}\right)\right). \tag{44}$$

As follows from Eq. (44), the valence band and conduction band of SWCNTs cross at the Fermi level, when $q = 2n/3$. This means that for all $(n,0)$ zigzag nanotubes the energy gap at $k = 0$ becomes zero, when $n = 3l$ ($l$ is an integer number), and nanotubes show metallic properties. When $n \neq 3l$, an energy gap opens at $k = 0$, and SWCNTs demonstrate semiconducting properties [2,63].

Fig. 8b shows the band structure of the (19,0) zigzag nanotube, represented along the ΓX direction [72]. It exhibits a finite energy gap at Γ point (because 19 is not a multiple of 3). Therefore, this nanotube has a semiconducting behavior.

It should be noted that the general rules for metallicity of armchair and zigzag nanotubes, considered above, are also valid for chiral $(n,m)$ SWCNTs. The valence and conduction bands of metallic chiral nanotubes cross on the Fermi level at the points $k = 0$ (the center of the first Brillouin zone) or $k = \pm 2\pi/3|\mathbf{T}|$ (at two-thirds of the distance between the zone center $k = 0$ to the zone boundaries $k = \pm\pi/|\mathbf{T}|$) [2,63]. From geometrical reasons, the band degeneracy occurs at $k = 0$, when $d_R = d$, where $d$ is the highest common divisor of $n$ and $m$, and at $k = \pm 2\pi/3|\mathbf{T}|$, when $d_R = 3d$ [2]. These $k$ values are also the locations of the energy gaps in semiconducting chiral SWCNTs. Fig. 8c demonstrates the band structure of the (12,3) chiral nanotube, represented along the ΓX direction [72]. Since for this nanotube $(n - m) = 9$ is a multiple of 3 and $d_R = 3d$, it has metallic properties with a band crossing at $k = \pm 2\pi/3|\mathbf{T}|$. It is worth noticing that the number of energy subbands for this chiral (12,3) nanotube is significantly larger than for the armchair (10,10) and zigzag (19,0) SWCNTs (Fig. 8a and b), which is a consequence of larger number of the cutting lines of the first Brillouin zone, as was discussed above.

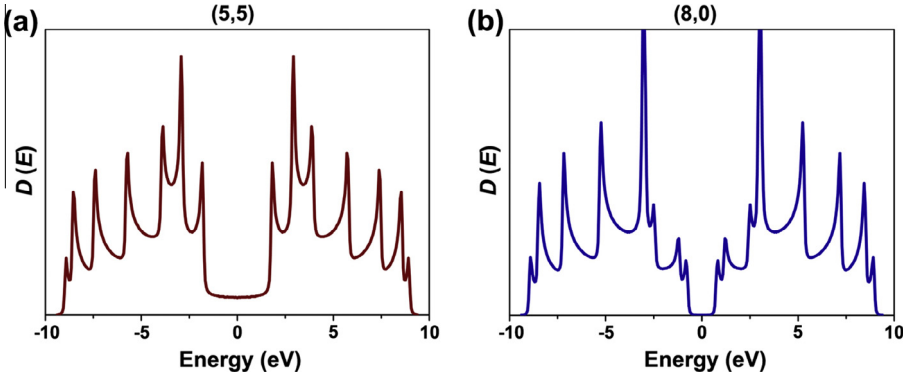


**Fig. 9.** The electronic density of states of the (5,5) armchair (a) and (8,0) zigzag (b) nanotubes, calculated using a tight-binding model. The Fermi level is positioned at zero energy. The densities of states of both nanotubes display van Hove singularities, which are characteristic of one-dimensional systems. The (5,5) SWCNT has a finite density of states at the Fermi level, and, therefore, it shows metallic properties. The (8,0) SWCNT has zero density of states at the Fermi level and, therefore, it shows semiconducting behavior. The data are replotted from Ref. [74].

### 3.5. Density of states of metallic and semiconducting SWCNTs

The electronic density of states (DOS) of SWCNTs is derived from the one-dimensional case of Eq. (16) applied to the energy dispersion relations in Eq. (37). The density of states $D(E)$ of nanotubes is represented in the following form:

$$D(E) = (|\mathbf{T}|/2\pi N)\sum_{\pm}\sum_{\nu=1}^{N}\int \frac{1}{\left|\frac{dE_{1D}^{\pm}(k)}{dk}\right|}\delta(E_{1D}^{\pm}(k) - E)dE, \tag{45}$$

where the summation is performed for the $N$ conduction (+) and valence (−) one-dimensional subbands, and the resulting value $D(E)$ is in units of states/carbon atom/eV [68,69].

The shape of the DOS is known to depend significantly on dimensionality of the system. The density of states of SWCNTs as the one-dimensional system is characterized by "spikes" (the so-called van Hove singularities, vHs) at energies close to band edges [2,63,68,69]. Every time when energy dispersion relations have local maxima or minima, the denominator in Eq. (45) vanishes and a spike appears in the density of states. The vHs in the valence and conduction bands of SWCNTs are placed symmetrically relatively to the Fermi level [2]. The positions of vHs depend on the nanotube diameter and metallicity (therefore, also on their chirality) [69]. The vHs close to the Fermi level come from the energy dispersion relations along the cutting lines near the K points of the first Brillouin zone of graphene [68]. For the metallic nanotubes the cutting line goes through the K point, as is was discussed above, and this leads to the zero energy gap. As a result, the density of states of metallic SWCNTs at the Fermi level has a finite value [2,63,68,69]. This value is constant and inversely proportional to the nanotube diameter [68]:

$$D(E_F) = \frac{a}{2\pi^2\gamma_0 d_t}. \tag{46}$$

In contrast, for semiconducting nanotubes the cutting lines do not cross the K point, and their density of states has a zero value at the Fermi level [2,63,68,69]. The energy extremum of each subband near the K point corresponds to a peak of van Hove singularity [69].

Fig. 9 demonstrates the electronic density of states of the armchair (5,5) and zigzag (8,0) nanotubes [73,74]. The (5,5) nanotube is metallic and, therefore, it has a non-zero DOS at the Fermi level. The (8,0) SWCNT is semiconducting with a large band gap and zero DOS at the Fermi level.

The energy difference $\Delta E$ between the highest vHs in the valence band and the lowest vHs in the conduction band for semiconducting nanotubes ($E_{11}^{S}$) and metallic SWCNTs ($E_{11}^{M}$) is in first order obtained as follows [68,69]:

$$E_{11}^{S} = \frac{2a_{c-c}\gamma_0}{d_t} \quad \text{and} \quad E_{11}^{M} = \frac{6a_{c-c}\gamma_0}{d_t}. \tag{47}$$

Therefore, these energies are inversely proportional to the nanotube diameter. We denote van Hove singularities in the valence and conduction bands that are symmetrically placed relatively to the Fermi level by the numbers $i$ ($i$ is a non-zero integer number), starting from the Fermi level. In accordance to the selection rules, the dominant parallel polarized optical transitions in semiconducting nanotubes ($E_{ii}^{S}$) and metallic SWCNTs ($E_{ii}^{M}$) can occur only between the symmetrical $i$-th vHs in the valence band and conduction band [68]. Semiconducting nanotubes of given diameter exhibit optical transitions with energies $E_{11}^{S}$, $2E_{11}^{S}$, $4E_{11}^{S}$, $5E_{11}^{S}$, $7E_{11}^{S}$, ... and metallic SWCNTs have optical transitions with energies $E_{11}^{M}$, $2E_{11}^{M}$, ... [69].

Fig. 10 demonstrates the plot of the energies of optical transitions $\Delta E$ between vHs in the valence band and the conduction band as a function of nanotube diameter $d_t$ for semiconducting ($E_{ii}^{S}$) and metallic ($E_{ii}^{M}$) SWCNTs of all possible chiralities ($n$,$m$) with diameters in the range from 0.7 to 3 nm. It was obtained by authors of Ref. [69] on the basis of the plot firstly reported by Kataura et al. [75]. The dependencies in Fig. 10 (which are called the Kataura plot) are based on the tight-binding model of Eqs. (34) and (35), with $\gamma_0 = 2.9$ eV and $s = 0$. The crosses and open circles correspond to semiconducting and metallic SWCNTs, respectively. It is seen that the energies of optical transitions

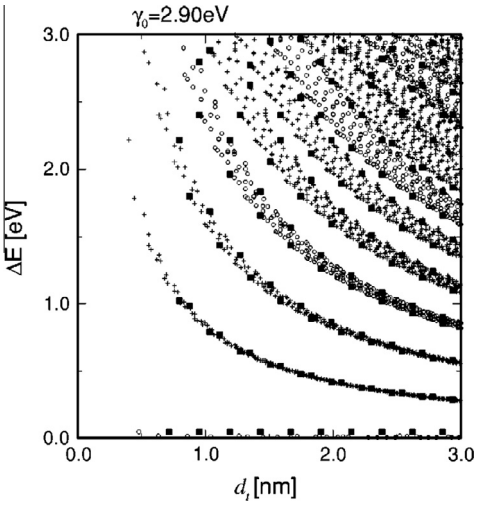


**Fig. 10.** The calculation of the energies of optical transitions $\Delta E$ between vHs in the valence band and the conduction band as a function of nanotube diameter $d_t$ for semiconducting ($E_{ii}^S$) and metallic ($E_{ii}^M$) SWCNTs of all possible chiralities ($n$,$m$) with diameters in the range from 0.7 to 3 nm (based on the report by Kataura et al. [75]). The plot is obtained using the tight-binding model with the parameters $\gamma_0 = 2.9$ eV and $s = 0$. The crosses and open circles correspond to semiconducting and metallic SWCNTs, respectively. The black squares denote the energies of zigzag SWCNTs that define the width of each curve. Along the abscissa there are the points for metallic SWCNTs with zero energy gap. Reprinted figure with permission from Saito R et al. Phys Rev B 2000;61:2981. Copyright 2000 by the American Physical Society [69].

decrease inversely proportional with increasing the diameter of nanotube. The width of the $E_{ii}^S$ and $E_{ii}^M$ curves at a constant diameter increases with increasing the energy and increasing the $i$ number. Also, the width of curves increases with decreasing the diameter. The black squares denote the energies of optical transitions for zigzag SWCNTs that define the width of each curve [69]. It should be noted that this plot is very useful for determining the diameter and chirality of SWCNTs from the optical absorption spectra and the resonant excitation energy of SWCNTs with particular diameters and chiralities in the Raman spectra, which is discussed in the following sections.

It is worth noticing that van Hove singularities as a characteristic feature of the density of states of SWCNTs are observed by different experimental techniques, such as scanning tunneling spectroscopy (STS) [76], electron energy loss spectroscopy (EELS) [77], optical absorption spectroscopy [75], photoluminescence spectroscopy [78], X-ray absorption spectroscopy [79] and ultraviolet photoelectron spectroscopy [80]. Their modification (disappearance, reducing, change in energies of the electronic transitions) testifies directly about changes in the electronic properties of nanotubes, which are considered below.

## 4. The methods of modification of SWCNT electronic properties

This section is dedicated to a description of different approaches to tune the SWCNT electronic properties.

### *4.1. Substitution of carbon atoms of SWCNT walls by other atoms*

The substitution of carbon atoms of SWCNT walls is one of the first methods developed to modify the electronic properties of nanotubes. The first article dedicated to the substitution of atoms of SWCNT walls [81] was published directly after the discovery of SWCNTs [1,82].

To date, the substitution of carbon atoms of SWCNT walls by nitrogen [83–93] and boron [90,94–101] was reported. It was shown that the modification of the SWCNT electronic structure is

defined by the type of the doping element and its concentration [102]. Firstly the influence of the element type will be considered. Nitrogen is on the right hand side neighbor of carbon in the periodic table. If it substitutes a carbon atom of a nanotube directly (Fig. 11a), donor doping of nanotubes takes place, and the additional electron gives rise to sharp localized states above the Fermi level [102]. Indeed, the same results were obtained in a number of reports [102–106]. However, this is not the only way to incorporate nitrogen atoms into the hexagonal lattice of carbon atoms of SWCNTs. The substitution of carbon atoms by nitrogen can be accompanied by defect formations in the nanotube walls, which lead to a rearrangement of carbon atoms (Fig. 11b and c), as a result the nitrogen atom is connected with only two carbon atoms [102,103,106,107]. When such a type of substitution is realized, the doping levels may appear either below or above the SWCNT Fermi level as dependent on the new wall structure, leading to acceptor or donor doping of nanotubes, respectively. It was demonstrated theoretically [104,108] and investigated experimentally [87,90,92,93].

Boron is the left hand neighbor of carbon in the periodic table, and is expected to mainly substitute carbon atoms in $sp^2$ configuration directly [102] and cause acceptor doping of nanotubes. Indeed, in Ref. [81] published in 1993 it was demonstrated theoretically that an acceptor level positioned 0.16 eV above the SWCNT Fermi level was formed in the case of nanotube doping by boron (1.25 at. % B). Later, the electronic structure of boron-substituted SWCNTs was studied in detail in Refs. [90,96,97,99,101].

The concentration of doping element is the second parameter that influences the modification of the SWCNT electronic structure. It was shown that in the case of low doping levels (for example, 0.2 at.% N [83] or 0.3 at.% N [84]) the modification of the SWCNT electronic structure can be considered within the rigid band model [102,103,109]. It means that the direct band structure modifications are negligible and that the band structure of the nanotubes with substituted carbon atoms can be obtained by the corresponding up- or downshift of the Fermi level in the band structure of pristine SWCNTs. But in the case of high doping levels this model can no longer be applied, because of the formation of so-called heteronanotubes [102,103].

The detailed experimental and theoretical investigation of the electronic structure of boron-substituted SWCNTs with different doping levels (up to 25%) was reported in Ref. [99]. Fig. 12 demonstrates the modification of the band structure and density of states of a semiconducting (16,0) nanotube with increasing the boron concentration [99]. For the undoped SWCNT (Fig. 12a), the Fermi level is positioned in the middle of the band gap, and the DOS is symmetric around the band gap for the first and second van Hove singularities. Boron doping of nanotubes causes a systematic downshift of the Fermi level into the valence band of the pristine SWCNT, which becomes larger with increasing boron concentrations from 6.25% (Fig. 12b) to 12.5% (Fig. 12c) and 25% (Fig. 12d). At the highest doping level, a new hexagonal $BC_3$ compound is formed. In this compound the relative downshift value of the Fermi level amounts to 2.2 eV (Fig. 12d). The rigid band model breaks down

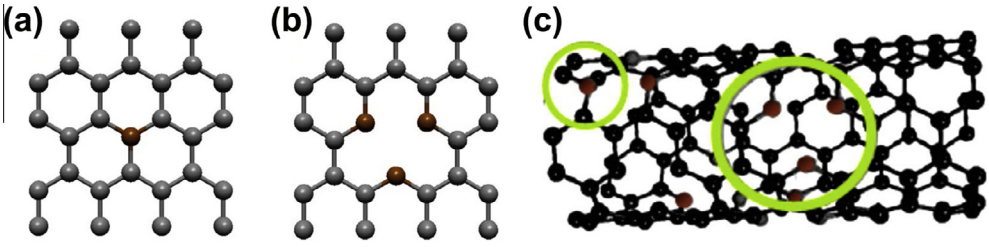


**Fig. 11.** Nitrogen can be introduced in the SWCNT walls in different ways. The first substitution configuration is (a) direct substitution, when nitrogen atoms (represented by red balls) replace directly carbon atoms (represented by gray balls) in the hexagonal lattice of SWCNT walls. The second substitution configuration is (b) pyridine-like bond formation, when the incorporated nitrogen atoms create defects in the SWCNT walls and are only connected with two carbon atoms. The structural model of a nanotube (c) demonstrates both types of substitutions of carbon atoms (black balls) by nitrogen atoms (red balls), which are marked by green circles. Reprinted figure with permission from Ayala P et al. Rev Mod Phys 2010;82:1843. Copyright 2010 by the American Physical Society [102].

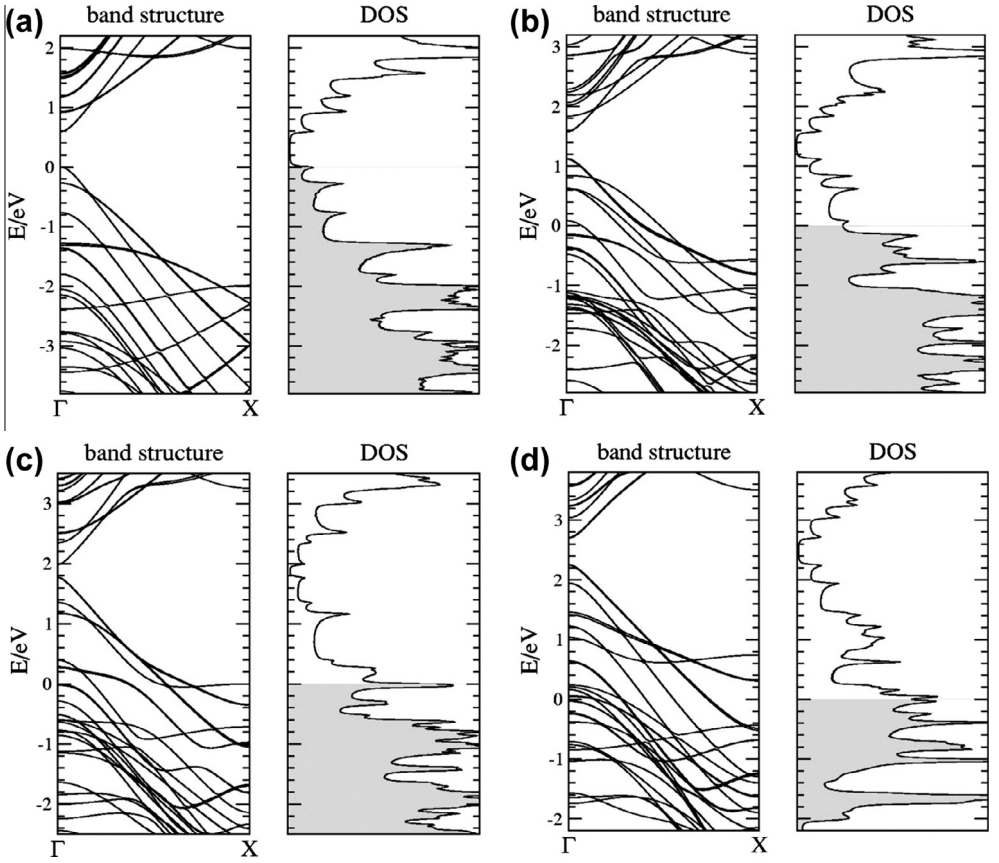


**Fig. 12.** Band structure and density of states of a (16,0) SWCNT with (a) 0%, (b) 6.25%, (c) 12.5%, and (d) 25% boron doping. The Fermi level, which is positioned at zero energy for the undoped nanotube, shifts into the valence band upon boron doping (filled states are colored in gray). The shift of the Fermi level increases with increasing the boron concentration. At the largest doping level (25%), a heteronanotube $BC_3$ is formed, and acceptor bands and new vHs appear above the highest occupied state of the undoped SWCNT. Reprinted figure with permission from Fuentes GG et al. Phys Rev B 2004;69:245403. Copyright 2004 by the American Physical Society [99].

in this case, because new bands and van Hove singularities emerge above the highest occupied state of the pristine SWCNT from the hybridization of boron acceptor levels with carbon levels [99].

It is worth noticing that the substitution of carbon atoms of the SWCNT walls may increase the oxidation resistance of nanotubes and also create new chemical pathways involving the dopant atoms [56].

### *4.2. Covalent and non-covalent modification of SWCNT outer surface*

The modification of the outer surface of SWCNTs may be performed in two ways. The first approach is attaching different functional groups using chemical (usually covalent) bonds (so-called chemisorption) [110]. The second approach is wrapping the nanotubes by different molecules or adsorption of molecules on the SWCNT walls without the formation of chemical bonds (so-called physisorption). Both these ways of the modification of the outer surface of SWCNTs may lead to changes in the electronic structure of nanotubes.

Firstly the covalent modification of the outer surface of SWCNTs will be considered. It was shown that the nanotubes can react with different classes of chemical compounds [111–135]. There are a

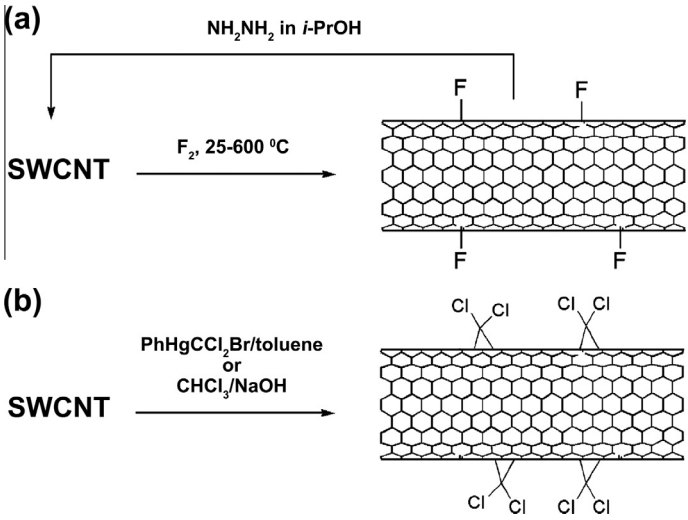


**Fig. 13.** (a) Reaction scheme for fluorination and defunctionalization of SWCNTs. The fluorination of SWCNTs by elemental fluorine at temperatures in the range between room temperature and 600 °C results in the attachment of fluorine to carbon atoms of the SWCNT walls. This reaction is reversible, and fluorine atoms can be removed from the nanotube surface *via* the treatment of nanotubes by hydrazine solution in propanol-2 with subsequent thermal treatment. (b) The scheme for cycloaddition reaction with dichlorocarbene, which is generated *in situ* using a phenyl(bromodichloro methyl)mercury reagent or a chloroform/sodium hydroxide mixture. Adapted with permission from Tasis D et al. Chem Rev 2006;106:1105. Copyright 2006 American Chemical Society [110].

number of reports dedicated to the investigation of the electronic properties of SWCNTs with outer surface modified *via* the halogenation and cycloaddition.

It was found that the fluorination of SWCNTs by elemental fluorine at temperatures in the range between room temperature and 600 °C [136–142] led to the attachment of fluorine to carbon atoms of the SWCNT walls (Fig. 13a). It was demonstrated that this reaction was reversible, and fluorine atoms could be removed from the nanotube surface *via* the treatment of nanotubes by hydrazine solution in propanol-2 with subsequent thermal treatment (Fig. 13a) [137,138,141,143,144].

The fluorination process of nanotubes was studied in detail by X-ray photoelectron spectroscopy [145–149], X-ray absorption spectroscopy [146,150], transmission electron microscopy [138], scanning tunnel microscopy [151] and theoretical calculations [152–159]. It was demonstrated that the fluorination of SWCNTs led to $sp^3$ rehybridization of carbon atoms and turned metallic and semiconducting SWCNTs into insulators [110].

The iodination of SWCNTs was reported in Ref. [160]. Iodine covalently bound to the nanotube surface was prepared *via* steps of oxidation and a subsequent modified Hunsdieker reaction with elemental iodine and iodosobenzene-diacetate. XPS, UV–vis–NIR and Raman spectroscopy confirmed that the functionalized nanotubes retained their characteristic electronic properties.

It was shown that the cycloaddition of organic molecules to the outer surface of SWCNTs can lead to a charge transfer between functional groups and the nanotube walls [110,161–166]. For example, the method of attachment of dichlorocarbene was reported in Ref. [163]. The organic substance was generated *in situ* using a chloroform/sodium hydroxide mixture or a phenyl(bromodichloro methyl) mercury reagent (Fig. 13b) [110]. Chemical analysis proved the presence of chlorine in the sample. The XPS and far-infrared spectroscopy data demonstrated that about 2% of the carbon atoms were covalently bonded with functional groups, and it led to a significant modification of the electronic structure of metallic SWCNTs.

The non-covalent modification of outer surface of SWCNTs can be performed *via* wrapping by polymers [111,135], surfactants [167–169], polynuclear aromatic compounds [170–174], and biomolecules [126] or *via* gas adsorption. The interaction mechanism is either van der Waals forces or $\pi$–$\pi$ stacking [110].

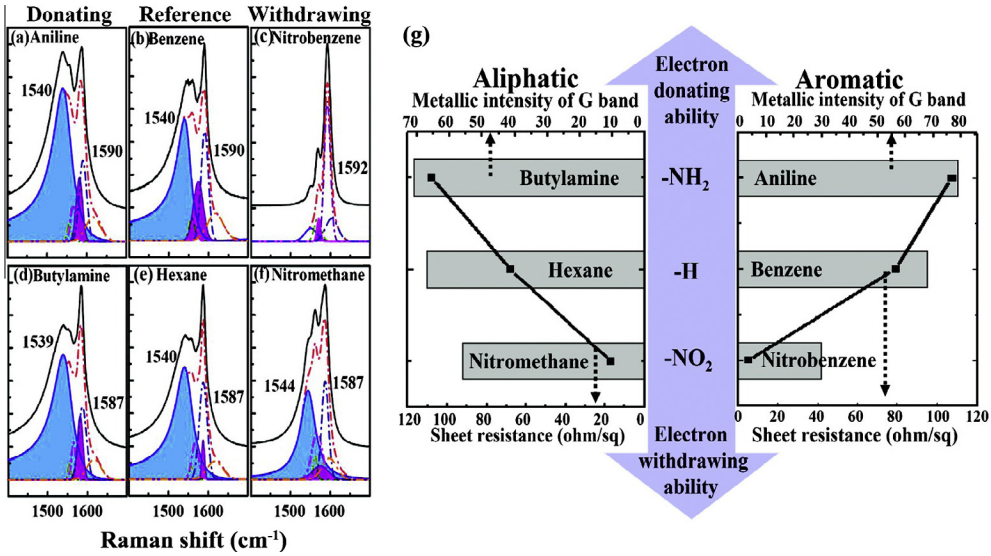


**Fig. 14.** The G-band of the Raman spectra of the SWCNT samples treated in aromatic solvents – aniline (a), benzene (b) and nitrobenzene (c) and aliphatic solvents – butylamine (d), hexane (e) and nitromethane (f) with electron-donating and electron-withdrawing functional groups, obtained at a laser energy of 1.96 eV. The spectra are deconvoluted into six components: five symmetric peaks (one metallic (shaded area in pink) and four semiconducting (open area)) and one metallic BWF peak (shaded area in blue). The numbers denote the positions of the peaks. (g) The relationship between the intensity of the metallic component of the G-band (denoted by gray column bars) and the sheet resistance (denoted by black squares that are connected by lines) for the aliphatic and aromatic solvents. The parameters increase for the solvents containing the electron-donating $–NH_2$ group and decrease for the solvents containing the electron-withdrawing $–NO_2$ group, as compared to the reference solvents without functional groups. Adapted with permission from Shin HJ et al. J Am Chem Soc 2008;130:2062. Copyright 2008 American Chemical Society [179].

There are several reports dedicated to the investigation of the modification of the electronic properties of nanotubes as a result of gas adsorption on their outer surface [175,176] and the presence of solvents [177–179].

The measurement of the electrical resistance of SWCNTs in nitrogen dioxide or ammonia atmosphere was performed in Ref. [176]. It was shown that the values were higher or lower, respectively, than the ones obtained as result of reference measurements in vacuum. It was demonstrated in Ref. [175] that the results of the measurements of the electrical resistance, thermoelectrical force and local density of states carried out in vacuum and in air were sufficiently different. The values changed reversibly even in the case of an insignificant change in the concentration of adsorbed gases. It even led to the transition of semiconducting nanotubes into metallic state. On the basis of the obtained data, the authors of Refs. [175,176] proposed the possible application of SWCNTs as gas sensors.

It was demonstrated in Refs. [177,178] that even such widely used dispersing agents like sodium dodecyl sulfate and polythiophen can result in changes in the electronic structure of SWCNTs. Authors of Ref. [179] investigated the influence of aromatic and aliphatic solvents containing donor and acceptor groups on the electronic structure of nanotubes. The analysis of Raman spectra of nanotubes in different solvent solutions was performed. The Raman active G-line was deconvoluted into six components, including five symmetric peaks (one metallic and four semiconducting) and one metallic BWF peak. In the spectra acquired at a 1.96 eV-laser for solvents with an aromatic backbone the shaded area of the metallic components increased to 79% for aniline and decreased to 30% for nitrobenzene, with respect to the reference – benzene (68%) (Fig. 14a–c). The metallic BWF component was completely suppressed for nitrobenzene. For solvents with an aliphatic backbone the metallic contribution was increased to 71% for butylamine, and the spectrum of SWCNTs in nitromethane showed no significant difference to the reference (hexane, 67%) (Fig. 14d–f). The increase or decrease of intensities of the

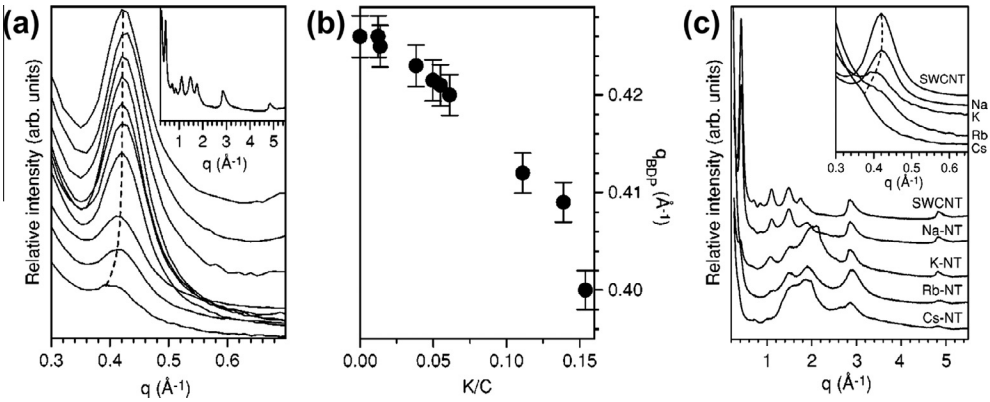


**Fig. 15.** (a) The modification of the first bundle diffraction peak of the pristine and successively potassium-intercalated SWCNTs with increasing the potassium content from K/C = 0 to K/C = 0.154 (from top to bottom). The position of the peak is traced by the dashed line. The inset demonstrates the diffraction pattern of the pristine SWCNTs in a wide momentum transfer region. (b) The relation between the momentum transfer of the bundle diffraction peak position ($q_{BDP}$) and the relative atomic ratio between potassium and carbon. The peak position shifts toward smaller momentum transfers with increasing the potassium concentration. (c) The electron diffraction patterns of the pristine SWCNTs and nanotubes fully intercalated by sodium, potassium, rubidium and cesium. The inset demonstrates the first bundle diffraction peak. This peak shifts toward smaller momentum transfers in the line with Na–K–Rb–Cs, as denoted by the dashed line. Reprinted figure with permission from Liu X et al. Phys Rev B 2003;67:125403. Copyright 2003 by the American Physical Society [195].

metallic components was attributed to donor or acceptor doping of nanotubes by different solvents, respectively [179]. The XPS and conductivity measurements data were in agreement with the Raman spectroscopy data, and proved that the charge transfer took place between the SWCNT walls and solvent molecules that led to a shift of the Fermi level. The modification of the electronic properties depended on the type of solvent. The use of aniline and butylamine containing the $-NH_2$ group led to donor doping of the SWCNTs, the use of nitrobenzene and nitromethane containing the $-NO_2$ group resulted in acceptor doping of the nanotubes. At the same time, benzene and hexane did not influence the electronic structure of the SWCNTs (Fig. 14g). Also, the effect of charge transfer in the solvent with an aliphatic backbone was weaker than in the solvent with an aromatic backbone [179].

### *4.3. Intercalation of SWCNT bundles*

The intercalation process refers to the incorporation of substances into triangularly shaped cavities inbetween the nanotubes in a bundle. The intercalation of SWCNT bundles was first reported in 1997. An increased electrical conductivity was observed for potassium and bromine-intercalated nanotubes in Ref. [180]. In Ref. [181], a softening of the G-line of the Raman spectra of potassium and rubidium-intercalated SWCNTs or stiffening of the G-line for bromine-intercalated nanotubes as compared to the pristine SWCNTs heralded the charge transfer between dopants and nanotubes. Later on, it was demonstrated that donor doping of SWCNTs can be achieved *via* the intercalation of SWCNTs by alkali metals, such as lithium, sodium, potassium, rubidium, cesium, and also barium [58,121,163,182–207]. At the same time, acceptor doping of nanotubes can be realized *via* the intercalation of bromine, iodine, iron trichloride, nitric acid, sulfuric acid, hydrochloric acid and gold trichloride molecules [28,163,177,182,188,193,199,208–219].

The intercalation usually does not result in the change in the structure of individual nanotubes. But according to the X-ray and electron diffraction data, this process leads to an expansion of the hexagonal packing of nanotubes in the bundles [183,184,188,189,194,198]. It was demonstrated that the expansion of bundles increases with an increase in the doping level and also radii of the introduced alkali metal ions [188]. Fig. 15 shows the electron diffraction data of the pristine nanotubes and the SWCNTs intercalated by different alkali metals [195]. The inset in Fig. 15a shows the diffraction data

of the pristine SWCNTs. The lower momentum transfers $q$ originate from the hexagonal order of the individual SWCNTs within the bundles and the higher $q$ come from the internal structure of the rolled-up graphene sheets. Fig. 15a demonstrates the modification of the first diffraction peak of the pristine and successively potassium-intercalated SWCNTs with increasing relative atomic ratio between potassium and carbon (K/C). The downshift of this peak with increasing potassium content from K/C = 0 (top curve) to K/C = 0.154 (bottom curve) corresponds to an expansion of the intertube distance in the bundle [195]. Fig. 15b traces the position of the first bundle peak ($q_{BDP}$) as a function of the potassium concentration. Fig. 15c compares the electron diffraction of the SWCNTs fully intercalated by different alkali metals: sodium, potassium, rubidium and cesium. It is clearly seen that the intensity of the first Bragg peak decreases from sodium to cesium [195]. The inset of Fig. 15c compares the first bundle peak of the SWCNTs fully intercalated with different metals. The metal atomic radii are in-line with the bundle lattice expansion and hence the downshift of the first bundle peak [195].

It was shown that the intercalation of nitric acid into the SWCNT bundle leads to the increase of intertube distance in a bundle by 0.185 nm after treatment with the concentrated solution for 2 h [208]. The same tendency was observed in the case of nanotube treatment with the concentrated solution of sulfuric acid [188]. Besides, it was found that the intercalation process is reversible. However, the long treatment of nanotubes with the acid solution (more than 12 h) resulted in their destruction [208], which was probably caused by an oxidation of nanotubes and defect formation in the SWCNT walls [10,129].

It was demonstrated that the maximal doping level that can be achieved at the intercalation of nanotube bundles by alkali metals, such as potassium, rubidium and cesium corresponds to the empirical formula $MC_7$ [195]. This is slightly higher than the value for fully potassium-intercalated graphite ($KC_8$) [220,221] and is a bit different from the value for intercalated fullerenes ($K_6C_{60}$) [222]. In the case of lithium intercalation, the maximal metal concentration depends on the synthesis method, and it may correspond to $LiC_6$ [191,197] or $Li_{1.2}C_6$ [186] stoichiometries. It was shown in Ref. [213] that the maximal intercalation level of SWCNTs by bromine corresponds to $BrC_7$. In the case of the intercalation of nanotube bundles by melted iodine, $IC_{12}$ stoichiometry was achieved [211].

A number of methods were used to investigate the electronic properties of SWCNTs intercalated by donor and acceptor substances. These techniques include electron energy loss spectroscopy [185,195,196,198,205,216,223,224], X-ray photoelectron spectroscopy [58,192,201,202,206,207], Raman spectroscopy [163,180–182,193,199,209,211,217,225–228], optical spectroscopy [163,191,197,213,216,224,229], electron spin resonance [189,190,204,230,231], and transport measurements [180,184,186,194,224,232]. The unaltered core-level excitations of alkali intercalated SWCNT bundles confirm the absence of rehybridization in the SWCNT $\pi$-system. The valence band is not perturbed by the intercalated metals [200]. It testifies that the intercalation does not lead to the formation of chemical bonds between incorporated atoms and the SWCNT walls. However, it was demonstrated in Ref. [196] that barium intercalation into the SWCNT bundles results in local interactions between metal atoms and nanotubes. It was shown that intercalation can lead to significant shifts of the SWCNT Fermi level by up to ±1.3 eV [200], as a result of donor or acceptor doping.

It was found that alkali metal intercalation changed the optical response of the nanotubes in a systematic way [200]. The intensity of the optical excitations depended on the doping level, because of the different Fermi energies in the intercalated nanotubes. The appearance of a charge carrier plasmon in the loss function of intercalated SWCNTs was observed. The plasmon energy increased with the doping level and decreased with the ionic radius of the alkali metal [200]. Fig. 16a shows the dependence of the loss function on carbon to potassium atomic ratio (C/K) [195]. The broad peak at 6 eV is the $\pi$ plasmon, which corresponds to a collective excitation of the $\pi$ electrons of nanotubes. The three peaks that are visible in the loss function of the pristine SWCNTs below 3 eV arise from electronic interband excitations between van Hove singularities. The lowest interband transitions are gradually depleted with increasing potassium content (Fig. 16a). This was explained by a charge transfer according to the rigid band shift: the conduction band of intercalated SWCNTs are populated with electrons, this leads to the suppression of previously allowed electronic excitations as their final states are filled up [195]. For high doping levels, also the electronic transition between the second van Hove singularities of semiconducting SWCNTs vanishes (Fig. 16b) [200]. This situation corresponds to the doping

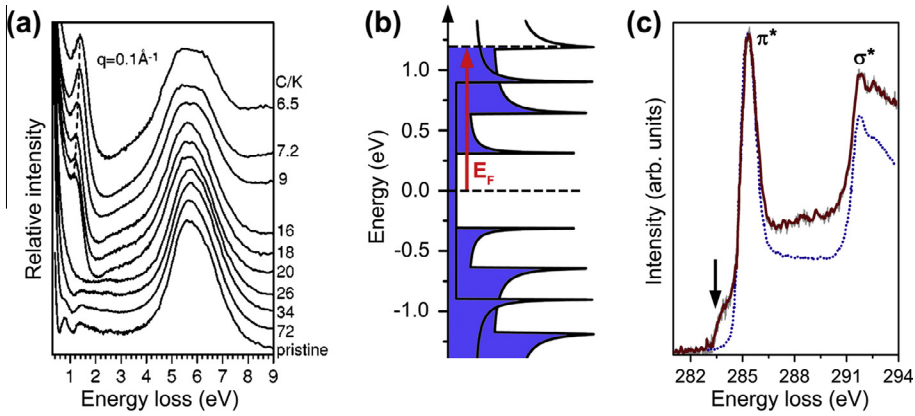


**Fig. 16.** (a) The loss function of pristine SWCNTs and potassium-intercalated nanotubes with different doping levels at $q = 0.1$ Å$^{-1}$, the carbon to potassium ratio (C/K) increases from bottom to top as denoted on the right side. At the doping levels larger than C/K $\approx$ 26, the Drude plasmon appears in the loss function at the energy between 1 and 2 eV. It shifts to higher energies with increasing the potassium concentration, as marked by the dashed line. Reprinted figure with permission from Liu X et al. Phys Rev B 2003;67:125403. Copyright 2003 by the American Physical Society [195]. (b) Scheme of the shift of the Fermi level of SWCNTs ($E_F$) as result of potassium intercalation. At high potassium concentrations, the Fermi level (denoted by the dashed line) shifts in the conduction band above the second vHs for semiconducting SWCNTs and the first vHs for metallic SWCNTs. Because these vHs are filled, as colored in blue, the corresponding optical transitions are suppressed. Figure is redrawn from Ref. [200]. (c) The C 1*s* core-level excitations of pristine (blue dotted line) and $FeCl_3$-intercalated SWCNTs (dark red solid line). The spectrum of intercalated nanotubes includes a new feature positioned at lower energies than the $\pi^*$ resonance, as highlighted by the arrow. The data are replotted from Ref. [216].

level of C/K $\approx$ 26 [200]. Up to this potassium content, the overall shape of the loss function of nanotubes does not change. However, at further increase in the doping level the so-called charge carrier or Drude plasmon associated with the collective excitation of the introduced quasi-free electrons emerges in the loss function in the energy range between 1 and 2 eV (Fig. 16a) [195]. It shifts to higher energies with increasing doping levels, which is consistent with the increase of the density of quasi-free electrons [195].

As for the intercalation of nanotube bundles with alkali metals, for *p*-type dopants, such as $FeCl_3$, an ionic transfer between the SWCNT walls and intercalated salt accompanied by the shift of nanotube Fermi level were found. In the case of $FeCl_3$, the formation of new empty states in the nanotube valence band was observed. Fig. 16c shows the C 1*s* core level excitations of pristine and iron trichloride-intercalated SWCNTs [216]. The spectrum of intercalated nanotubes includes a new peak positioned at lower energies than the $\pi^*$ resonance, as shown by the arrow, which corresponds to electronic transitions into empty $\pi$-orbitals. Also, the spectrum of intercalated nanotubes demonstrates the shift of the $\pi^*$ resonance toward higher energies, which may be caused by rise of the carbon 1*s* binding energy due to the decreased net charge on the carbon atoms of intercalated SWCNTs [216]. It should be noted that the maximal doping level for iron trichloride intercalation is much less as compared to the alkali metal-intercalated SWCNTs, which is caused by the larger size of $FeCl_3$ molecules [200].

It was found that the intercalation of sulfuric, nitric and hydrochloric acids into the SWCNT bundles leads to *p*-doping of nanotubes [210], which is accompanied by the formation of an acceptor level below the SWCNT Fermi level [233] and a charge transfer from the nanotube walls [208,219].

### *4.4. Filling the SWCNT channels*

The method of filling the SWCNTs is based on the encapsulation of different simple substances and chemical compounds into the internal channels of nanotubes. This method is very promising for the directional modification of the electronic properties of SWCNTs. This is caused by the following reasons. Firstly, the list of substances that can be potentially incorporated inside the SWCNT channels

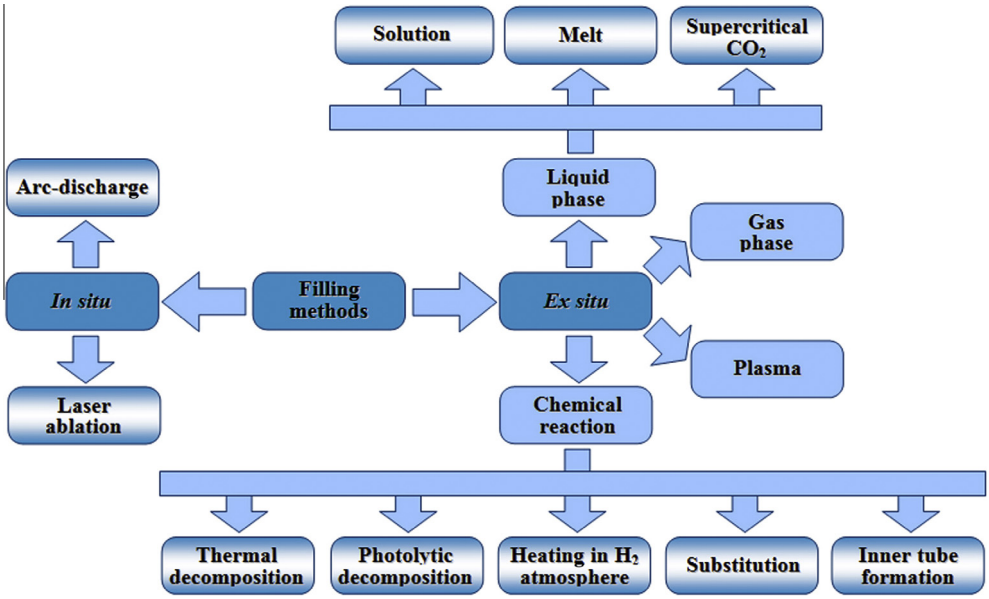


**Fig. 17.** The overview of filling methods of the SWCNT channels. They are divided into two groups: the *in situ* and the *ex situ* methods. The *in situ* method includes the arc-discharge and laser ablation approaches. The *ex situ* method includes approaches from gas phase, liquid phase, using plasma and chemical reactions inside the SWCNT channels. The liquid phase filling is conducted using solutions, melts or supercritical $CO_2$. The chemical reactions inside SWCNTs involve the thermal or photolytic decomposition of a precursor, its heating in hydrogen atmosphere, substitution reactions and inner tube formation.

is very extensive, and it opens the way to donor and acceptor doping of nanotubes and controlling the doping level *via* filling the SWCNTs with substances possessing required chemical and physical properties (see Sections 5, 6.1.1 and 6.2.1). Secondly, the filling methods for desired substances are well-established (see Section 5). And thirdly, the large filling degrees of nanotube channels can be achieved by a suitable encapsulation process, which may lead to a significant modification of the electronic structure of SWCNTs (see Sections 6.1.2 and 6.2.2).

### *4.5. Nanochemical reactions inside the SWCNT channels*

Nanochemical reactions encompass the filling of the SWCNT channels and the subsequent chemical transformation of the encapsulated substance to tune the electronic properties of nanotubes. The chemical reaction inside the SWCNT channels allows varying the Fermi level of nanotubes (i.e., increase or decrease it) as well as switching the doping type (i.e., from *n*- to *p*-type, or vice versa). Thus, it allows fine tuning of the electronic structure of SWCNTs by choosing an appropriate precursor and conditions for the nanochemical reaction (see Section 7).

## 5. Synthesis of filled nanotubes

This section is dedicated to a description of filling methods of nanotubes, including the nanochemical reactions inside the SWCNT channels.

According to the literature data, several methods are used to fill the SWCNT channels, which differ in the filling procedure, aggregate state of the used substances and other parameters. These approaches include the *in situ* method and the *ex situ* filling methods from gas phase, liquid phase, using plasma and chemical reactions inside the SWCNT channels. Fig. 17 shows the scheme illustrating the classification of filling methods of SWCNTs. Table 1 summarizes the filling methods of SWCNTs

**Table 1**
The filling methods of SWCNTs and examples of substances that were encapsulated into the nanotube cavities using these approaches.

| Filling method | | Type of substance | | Example | Reference |
|---|---|---|---|---|---|
| *In situ* | Arc-discharge method | Molecule | Fullerene | $C_{60}$, $C_{80}$ | [12,14,234] |
| | | Simple substance | Metal | Bi | [20] |
| | Laser ablation | Molecule | Fullerene | $C_{60}$, $C_{70}$ | [5,13,14,235] |
| *Ex situ* | *Gas phase* | | | | |
| | | Molecule | Fullerene | $C_{60}$, $C_{70}$, $C_{78}$, $C_{80}$, $C_{82}$, $C_{90}$ | [8–10,236–241] |
| | | | Azafullerene | $C_{59}N$ | [242] |
| | | | Doped fullerene | $C_{60}$/K, $C_{60}$/$FeCl_3$ | [243–245] |
| | | | Endohedral fullerene | Ca@$C_{82}$, La@$C_{82}$, Ce@$C_{82}$, Sm@$C_{82}$, Gd@$C_{82}$, Dy@$C_{82}$, $La_2$@$C_{80}$, $Ti_2$@$C_{80}$, $Sc_2$@$C_{84}$, $Gd_2$@$C_{92}$ | [8,15,49,237,239,246–256] |
| | | | Exohedral fullerene | $C_{60}Cs$ | [16] |
| | | | Metallocene | Ferrocene $(C_5H_5)_2Fe$, cobaltocene $(C_5H_5)_2Co$, $(C_5H_4C_2H_5)_2Co$, cerocene $(C_5H_5)_3Ce$ | [7,47,50,51,257–269] |
| | | | Metal acetylacetonate | $Pt(C_5H_7O_2)_2$ | [270] |
| | | | Other molecules | Ortho-carborane, TDAE[a], TMTSF[b], TTF[c], DNBN[d], TCNQ[e], $F_4$TCNQ[f], pentacene, tetracene, anthracene | [11,48] |
| | | Simple substance | Nonmetal | Se | [17] |
| | | | Metal | K, Bi, Eu | [20,271–273] |
| | | Chemical compound | Halogenide | $ZrCl_4$ | [23,24] |
| | | | Oxide | $Re_xO_y$ | [18] |
| | *Liquid phase* | | | | |
| | Solution | Molecule | Carbyne | $C_{10}H_2$ | [274] |
| | | | Fullerene | $C_{60}$ | [14,241,275,276] |
| | | | Endohedral fullerene | N@$C_{60}$ | [241] |
| | | | | $Sc_3N$@$C_{80}$, $Dy_3N$@$C_{80}$, $Er_xSc_{3-x}N$@$C_{80}$ | [277–279] |
| | | | Exohedral fullerene | Complex compounds of $C_{60}$ with Re and Os carbonyls | [280–282] |
| | | | Functionalized fullerene | $C_{60}$ with organic complex compound of cadmium | [283] |
| | | | Functionalized endohedral fullerene | $Sc_3N$@$C_{80}$ with organic groups | [277] |
| | | | Metallocene | Ferrocene $(C_5H_5)_2Fe$ | [258,284] |

(*continued on next page*)

**Table 1** (*continued*)

| Filling method | Type of substance | | Example | | Reference |
|---|---|---|---|---|---|
| | | Metal acetylacetonate | $Pt(C_5H_7O_2)_2$, $Co(C_5H_7O_2)_2$ | | [266,270,285] |
| | | Other molecules | Porphyrin complex compounds of zinc (II) and platinum (II), rhodamine, chlorophyll, β-carotene | | [286–289] |
| | Chemical compound | Halogenide | $FeCl_3$, $RuCl_3$, $PtCl_4$ | | [6,19,290,291] |
| | | Oxide | $CrO_3$ | | [46,292] |
| | | Nitrate | $AgNO_3$, $Cu(NO_3)_2$, $Bi(NO_3)_3$, $UO_2(NO_3)_2$ | | [19,20,22,45,46,293–296] |
| | | Acetate | $UO_2(CH_3COO)_2$ | | [45] |
| Supercritical $CO_2$ | Molecule | Fullerene | $C_{60}$ | | [297–299] |
| | | Azafullerene | $C_{59}N$ | | [242] |
| | | Endohedral fullerene | $Er_3N@C_{80}$ | | [299] |
| | | Exohedral fullerene | $C_{60}O$ | | [300] |
| | | Functionalized fullerene | $C_{61}(COOH)_2$, $C_{61}(COOC_2H_5)_2$ | | [298,299] |
| | | | $C_{60}$ with alkyl chains | | [301] |
| Melt | Simple substance | Nonmetal | $I_2$, S, Se, Te | | [28,31,302,303] |
| | Chemical compound | Halogenide | $SnF_2$, (Na/Cs/Cu/Ag/Tl)Cl, (Fe/Co/Ni/Mn/Pd/Zn/Cd)$Cl_2$, (Y/Au/La/Nd/Sm/Eu/Gd/Tb/Ho/Tm/Er/Yb)$Cl_3$, $Al_2Cl_6$, (Zr/Hf/Pt/Th)$Cl_4$, $MoCl_5$, $WCl_6$, $(KCl)_x(UCl_4)_y$, (Cs/Cu/Ag)Br, (Fe/Co/Ni/Mn/Zn/Cd)$Br_2$, (Li/Na/K/Rb/Cs/Cu/Ag)I, (Ca/Sr/Ba/Fe/Co/Zn/Cd/Pb)$I_2$, $LaI_3$, $Al_2I_6$, $SnI_4$, $AgCl_{1-x}I_x$, $AgCl_xBr_yI_z$ | | [19,21,24,26,27,29,30,32–35,37–44,56,304–322] |
| | | Chalcogenide | HgTe, SnSe, SnTe, GaSe, $Bi_2Te_3$, $MnTe_2$, $CdBr_{2-x}Te_x$ | | [24,33,36,315,323–328] |
| | | Oxide | PbO, $Sb_2O_3$, $Cr_2O_3$ | | [25,329–331] |
| | | Hydroxide | CsOH, KOH | | [45] |
| *Plasma* | | | | | |
| | Simple substance | Metal | Cs | | [332,333] |
| | | Metal/nonmetal | Cs/I | | [334] |
| | Molecule | Fullerene | $C_{60}$ | | [335] |
| | Mixed | Metal/fullerene | $Cs/C_{60}$ | | [334] |
| *Chemical reaction* | | | *Precursor* | *Product* | |
| Thermal decomposition | Simple substance | Metal | $AgNO_3$ | Ag | [19,22,46,293,294,296,315] |
| | | | $W(CO)_6$ | W | [336,337] |
| | | | $Re_2(CO)_{10}$ | Re | [336,337] |
| | | | $Os_3(CO)_{12}$ | Os | [336,337] |
| | | | $ErCl_3$ | Er | [304] |

**Table 1** (*continued*)

| Filling method | Type of substance | | Example | | Reference |
|---|---|---|---|---|---|
| Photolytic decomposition | | | AgCl | Ag | [21] |
| Heating in $H_2$ atmosphere | | | $Bi(NO_3)_3$ | Bi | [20] |
| | | | $Cu(NO_3)_2$ | Cu | [293,295] |
| | | | $FeCl_3$ | Fe | [290,291] |
| | | | $Co(acac)_2$ | Co | [285] |
| | | | $RuCl_3$ | Ru | [6] |
| | | | $PdCl_2$ | Pd | [19] |
| | | | $Re_xO_y$ | Re | [18] |
| | | | $HAuCl_4$ | Au | [19] |
| | | | $H_2PtCl_6$ | Pt | [19] |
| Substitution | Chemical compound | Chalcogenide | $CdI_2$, $ZnI_2$, $PbI_2$ | CdS, ZnTe, PbTe | [338] |
| Chemical reaction with the DWCNT formation | Molecule | Fullerene | $C_{60}$ | Inner tube | [339–348] |
| | | | $C_{70}$ | Inner tube | [341,342] |
| | | Endohedral fullerene | $Gd@C_{82}$ | Gd inside inner tube | [49,250,256] |
| | | Metallocene | $(C_5H_5)_2Fe$ | Iron carbide inside inner tube | [50,257–261,264–268,284] |
| | | | $(C_5H_5)_3Ce$ | Ce inside inner tube | [51,269] |
| | | Metal acetylacetonate | $Pt(C_5H_7O_2)_2$ | Pt inside inner tube | [266,270] |
| | | Other molecules | Toluene + $C_{60}$ | Inner tube | [349] |
| | | | Anthracene | Inner tube | [350] |

[a] TDAE = tetrakis(dimethylamino)ethylene.
[b] TMTSF = tetramethyl-tetraselenefulvalene.
[c] TTF = tetrathiafulvalene.
[d] DNBN = 3,5-dinitrobenzonitrile.
[e] TCNQ = tetracyano-*p*-quinodimethane.
[f] $F_4$TCNQ = tetrafluorocyano-*p*-quinodimethane.

and examples of substances that were encapsulated into the nanotube cavities using these approaches.

### 5.1. In situ filling the SWCNT channels

On the one hand, the *in situ* method is the simplest one-step approach to fill the SWCNT channels. On the other hand, it is obvious that this advantage shorts the list of the substances that can be encapsulated inside the SWCNT cavities and limits the opportunity to vary parameters of the filling procedure. Most probably that is why there are only several reports dedicated to the *in situ* filling of SWCNTs. One of these examples is the encapsulation of metallic bismuth into the nanotube channels during their synthesis by the arc-discharge method [20]. To fill the SWCNTs, the authors added bismuth to cobalt that was used as a catalyst. Bismuth was incorporated into the SWCNT channels during the high-temperature gas phase reaction. However, the achieved filling degree turned out to be very low (about 1%). Another example of the *in situ* filling of SWCNTs is a spontaneous trapping of fullerene molecules inside the nanotube channels during their synthesis by the arc-discharge [12,14,234] and laser ablation [5,13,14,235] methods.

### 5.2. Ex situ filling the SWCNT channels

In contrast to the *in situ* filling method, the *ex situ* approach allows encapsulating different simple substances, molecules and chemical compounds inside the SWCNT channels due to the possibility of varying the synthesis parameters and choosing the specific type of substances and nanotubes.

#### 5.2.1. Opening the SWCNT ends

Because the ends of synthesized SWCNTs are usually closed by fullerene caps, the procedure of opening the SWCNT ends has to be carried out before their filling. This process can be performed in two ways: using gaseous (air, oxygen, ozone [8,45,351]) or liquid (concentrated acids – hydrochloric, sulfuric, nitric or their mixtures [6,8,10,236,352,353]) oxidizers. It should be noted that these reagents are usually used for the purification of synthesized SWCNTs, but this process does not necessarily lead to an effective opening of the nanotube ends [56].

The process parameters which are important during the opening of the SWCNT ends are the type of oxidizer, as well as time and temperature of the treatment. It is obvious that the oxidation of nanotubes starts from their ends, where topological defects are localized. Fullerene caps contain pentagons of carbon atoms which are the most reactive parts of SWCNTs [56]. However, longer oxidizing treatment can lead to the formation of defects in the SWCNT walls and their destruction.

In general, the process parameters depend on the nanotube diameter and methods of their synthesis and purification. It was shown in a number of papers [8,55,56] that the gas phase oxidation is not only the simpler, but also more effective method of opening the SWCNT ends than the liquid phase approach. Besides, it was found that amorphous particles forming during the liquid-phase opening process may cover the SWCNT walls and block their ends [10,55]. Because of these facts, the annealing of nanotubes in air at temperatures between 400 and 500 °C for 30–60 min was the most frequently employed procedure for the opening of SWCNT ends. It was used in most papers that are considered below.

#### 5.2.2. Filling the SWCNTs from gas phase

This approach is based on the filling of the SWCNTs by a substance in gas state at a temperature higher than its boiling or sublimation point. During the process, the vapor of a substance condenses and diffuses inside the SWCNT channels, and crystallizes upon cooling the system. This method is well-established and it allows achieving high filling degrees of SWCNTs. However, the list of substances that can be incorporated inside the SWCNT channels using this approach is limited, because the maximal boiling or sublimation temperature of the substance cannot be higher than 1000–1200 °C (nanotubes start to degrade at higher temperatures). Besides, the substance should not decompose during evaporation or sublimation, and it should have a high vapor pressure at synthesis temperature in order to achieve high filling degrees of nanotube channels and also shorten the time of the synthesis procedure.

The gas phase filling method is the traditional approach to encapsulate fullerene molecules inside the nanotube channels. Using this method the SWCNT cavities were filled with $C_{60}$, $C_{70}$, $C_{78}$, $C_{80}$, $C_{82}$, $C_{90}$ fullerenes [8–10,236–241]. It was shown that the filling goes according to diffusion mechanism, and the filling degree can be as high as 100%. The effectiveness of this method was demonstrated by filling the SWCNT channels with molecules of azafullerenes ($C_{59}N$) [242], endohedral fullerenes ($M@C_{82}$, where M = Ca, La, Ce, Sm, Gd and Dy [8,15,49,237,239,246,247,249–252,256], $M_2@C_{80}$, where M = La and Ti [248,253], $Sc_2@C_{84}$ [254], $Gd_2@C_{92}$ [255]) and exohedral fullerenes ($C_{60}Cs$) [16], metallocenes (ferrocene $(C_5H_5)_2Fe$ [7,50,257–268], cobaltocene $(C_5H_5)_2Co$, $(C_5H_4C_2H_5)_2Co$ [47], cerocene $(C_5H_5)_3Ce$ [51,269]), metal acetylacetonates ($Pt(C_5H_7O_2)_2$) [270] and other molecules (orthocarborane [11], TDAE, TMTSF, TTF, DNBN, TCNQ, $F_4TCNQ$, pentacene, tetracene, anthracene [48]). Furthermore, using this method the SWCNTs were filled with simple substances (nonmetals – Se [17] and metals – K [273], Bi [20], Eu [271,272]), halogenides ($ZrCl_4$ [23,24]) and oxides ($Re_xO_y$ [18]) (Table 1).

Fig. 18 shows the HRTEM data of the SWCNTs filled using the gas phase method. Fig. 18a presents the micrograph of the $Gd@C_{82}$-filled nanotube [250]. The endohedral fullerene molecules are clearly

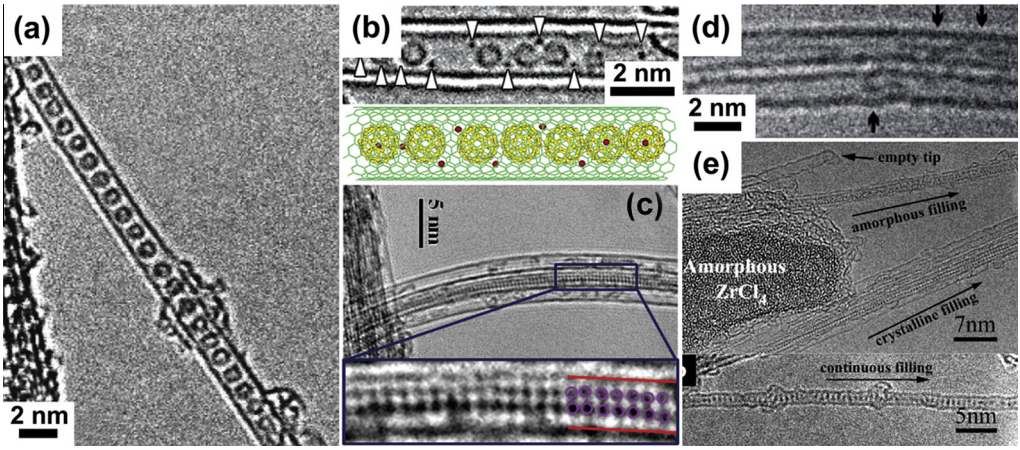


**Fig. 18.** The HRTEM data of SWCNTs filled using the gas phase method. (a) Endohedral fullerene Gd@$C_{82}$ molecules inside an individual nanotube. Adapted with permission from Kitaura R et al. Nano Lett 2008;8:693. Copyright 2008 American Chemical Society [250]. (b) Upper part: Exohedral fullerene $C_{60}$Cs molecules inside an individual SWCNT. The white arrows indicate the Cs metal atoms. Lower part: The schematics representing the HRTEM image. Fullerene molecules are shown in yellow, Cs atoms – in red, nanotube walls – in green color. Adapted with permission from Sun BY et al. J Am Chem Soc 2005;127:17972. Copyright 2005 American Chemical Society [16]. (c) Upper part: Eu nanowires inside a bundle of SWCNTs. Lower part: The magnified image of the area denoted by the blue rectangle. Red lines indicate the nanotube walls, and purple circles denote the encapsulated Eu atoms. Reprinted figure with permission from Nakanishi R et al. Phys Rev B 2012;86:115445. Copyright 2012 by the American Physical Society [272]. (d) Cobaltocene molecules inside two individual SWCNTs. The encapsulated molecules are marked by the arrows. Adapted by permission from Macmillan Publishers Ltd: Nat Mater, Li LJ et al. Nat Mater 2005;4:481, Copyright 2005 [47]. (e) Zirconium chloride-filled SWCNTs. Upper part: The image demonstrating an empty SWCNT, nanoparticle of not encapsulated $ZrCl_4$, nanotubes filled with amorphous $ZrCl_4$ and SWCNT bundle partially filled with crystalline $ZrCl_4$. Lower part: An individual continuously filled nanotube. Reprinted from Brown G et al. Appl Phys A 2003;76:457. Copyright 2003 Springer-Verlag, with kind permission from Springer Science and Business Media [24].

seen inside the SWCNT channel. They are densely packed and form a one-dimensional crystalline array. A typical filling degree of nanotubes as estimated from the HRTEM data is more than 90% [250].

Fig. 18b shows the micrograph of the individual SWCNT filled with exohedral fullerene $C_{60}$Cs [16]. Two parallel lines correspond to the nanotube walls, and the circle contrasts aligned within the SWCNT correspond to the entrapped $C_{60}$ molecules. Dark spots seen adjacent to the fullerene molecules are the exohedrally attached Cs metal atoms, as indicated by the white arrows. Below the micrograph in Fig. 18b there is the schematics representing the HRTEM image, where fullerene molecules are shown in yellow, Cs atoms – in red, nanotube walls – in green color [16].

Fig. 18c demonstrates the micrograph of the SWCNTs filled with Eu nanowires [272]. It is clearly seen that crystalline nanowires are formed inside the SWCNT channels, and no Eu atoms are observed on the outer surface of nanotubes. The magnified image of the area denoted by the blue rectangle shows a $2 \times 2$ structure of the metal nanowire. Red lines indicate the nanotube walls, and purple circles denote the encapsulated Eu atoms.

Fig. 18d presents the HRTEM image of the SWCNTs filled with cobaltocene molecules [47]. Two individual nanotubes are observed. The encapsulated molecules are clearly seen inside their channels as contrast elements, which are marked by the arrows.

Fig. 18e shows the micrographs of the $ZrCl_4$-filled SWCNTs [24]. The average filling degree of nanotubes in this sample was estimated to be about 20–30%. At the top of the upper image, an empty SWCNT is marked. Below this, a pair of overlapping nanotubes with amorphous filler is observed. To the center left of the image, a large nanoparticle of amorphous $ZrCl_4$ is seen, which corresponds to not encapsulated material. At the bottom of the upper image, a bundle of 8–10 nanotubes, one of which is filled with crystalline $ZrCl_4$, is observed. The lower image shows an individual

1.1 nm-diameter nanotube that is completely filled with zirconium chloride. The atoms of $ZrCl_4$ are clearly visible inside the SWCNT channel.

*5.2.3. Filling the SWCNTs from liquid phase*

This method is conducted *via* the filling of the SWCNT channels with solutions of substances in solvents under ambient conditions or in supercritical $CO_2$, or *via* the impregnation of nanotubes by melts of substances with subsequent slow cooling for their crystallization inside the SWCNT cavities. Because the synthesis parameters of liquid phase filling can be broadly varied, a long list of substances can be introduced inside the SWCNTs using this method, and it makes this approach the most popular filling method of nanotubes.

The synthesis parameters which are the most important during the filling of the SWCNTs with solutions are the solubility of desired substance in the solvent, the surface tension coefficient of the solution and its viscosity [56]. Because the surface tension coefficient of solvents is usually low enough (less than 80 mN/m), the choice of an appropriate solvent allows filling the SWCNT channels with different substances. For some substances, it is the only feasible way of incorporation inside the nanotubes. Employing this method allowed encapsulating inside the SWCNT cavities linear molecules $C_{10}H_2$ [274], fullerene $C_{60}$ [14,241,275,276], nitrogen-containing endohedral fullerenes ($N@C_{60}$ [241] and $Sc_3N@C_{80}$, $Ho_3N@C_{80}$, $Dy_3N@C_{80}$, $Er_xSc_{3-x}N@C_{80}$ [277–279]), exohedral fullerenes (complex compounds of $C_{60}$ with Re and Os carbonyls) [280–282] and functionalized fullerenes ($Sc_3N@C_{80}$ with organic groups [277] and $C_{60}$ with an organic complex compound of cadmium [283]), metallocenes (ferrocene) [258,284], metal acetylacetonates (acetylacetonates of platinum (II) [266,270] and cobalt (II) [285]) and other molecules (porphyrin complex compounds of zinc (II) and platinum (II) [286,287], rhodamine [287], chlorophyll [287], β-carotene [288,289]) (Table 1). The filling of the SWCNT channels with solutions of metal halogenides ($FeCl_3$ [290,291], $RuCl_3$ [6], $PtCl_4$ [19]), metal nitrates ($AgNO_3$ [19,22,46,293,294,296], $Cu(NO_3)_2$ [293,295], $Bi(NO_3)_3$ [20], $UO_2(NO_3)_2$ [45]) and metal acetates ($UO_2(CH_3COO)_2$ [45]) with further chemical transformation of salts (see Section 5.2.5) allowed synthesizing metallic nanoparticles inside the SWCNT channels. Furthermore, it was demonstrated that this method can be used to fill the nanotubes with chromium oxide $CrO_3$ [46,292].

Fig. 19a shows the HRTEM data of SWCNTs filled by the solution method. Fig. 19a1 presents the micrograph and structural diagram of the individual nanotube filled with complex compound of $C_{60}$ with osmium carbonyl [280]. It is clearly seen that the fullerene molecules are encapsulated inside the SWCNT channel. A chain of five molecules is observed in the middle part of the nanotube, as indicated by the white arrows. To the side of each $C_{60}$ cage, dark contrast features are visible, which correspond to metal atoms. The structural diagram shown to the right of the HRTEM image represents the observed orientation of the molecules inside the SWCNT channel.

Fig. 19a2 demonstrates the micrograph and structural diagram of the SWCNTs filled with endohedral fullerene $Ho_3N@C_{80}$ [277]. It is seen that the encapsulated molecules are densely packed within the SWCNT, so that there is only minimal van der Waals distance of ~0.3 nm between the neighboring molecules. The endohedral cluster $Ho_3N$ is clearly visible inside the molecules, where dark contrast elements correspond to the metal atoms. Authors of Ref. [277] noted that translational motion of the fullerene molecules inside the nanotube is suppressed as a result of the close packing. However, the orientations of the endohedral clusters can still vary, as clearly seen on the structural diagram representing the HRTEM image.

Fig. 19a3 shows the micrograph of the SWCNTs filled with chromium oxide $CrO_3$ [292]. A nanotube bundle is seen, where the outer nanotube from the bundle periphery exhibits obvious filling (as denoted by the arrow). Dark material is observed between the SWCNT walls, which corresponds to $CrO_3$. It is visible that the filling is segmented, and the encapsulated material has amorphous structure. The filling degree of nanotubes was estimated to be 25–30% [292].

In general, the solution method is effective, however it has several disadvantages. Firstly, the filled SWCNTs are contaminated with solvent molecules, which can be critical for their further investigations. Secondly, the filling degrees of SWCNT channels are usually not more than 30% [56], which is relatively low, for example, as compared to the filling method from melts. Thirdly, the morphology of encapsulated substances in the SWCNT channels is inhomogeneous.

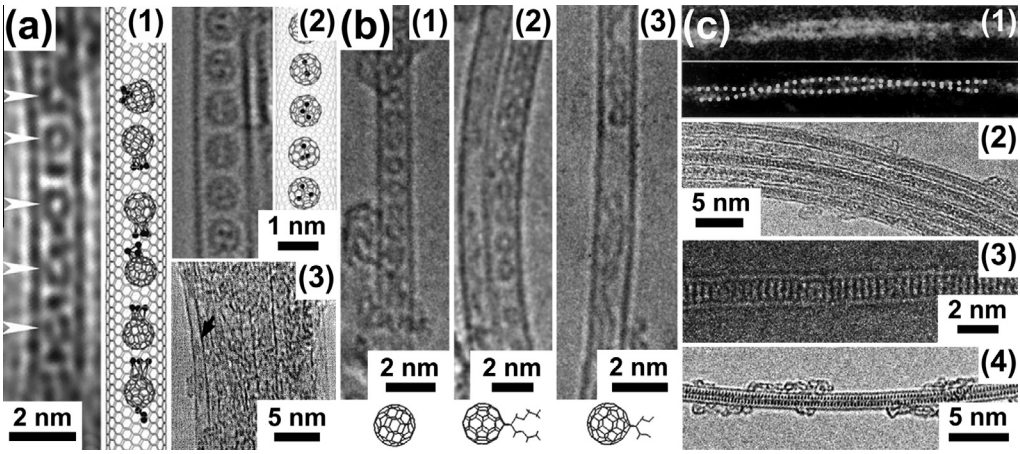


**Fig. 19.** The HRTEM data of SWCNTs filled by the liquid phase method. (a) The nanotubes filled *via* the solution approach. (1) Complex compound of $C_{60}$ with osmium carbonyl inside the SWCNT. Left part: The image demonstrating an individual filled SWCNT. The white arrows indicate five encapsulated molecules. Right part: The structural diagram representing the observed orientation of the molecules inside the SWCNT channel. Black dots correspond to Os atoms. Reprinted with permission from Chamberlain TW et al. Chem A: Eur J 2011;17:668. Copyright 2011 Wiley-VCH Verlag GmbH & Co. KGaA, Weinheim [280]. (2) Endohedral fullerene $Ho_3N@C_{80}$ inside the SWCNT. Left part: The micrograph showing an individual filled nanotube. Right part: The structural diagram representing the HRTEM image. Black dots correspond to Ho atoms. Adapted from Gimenez-Lopez MD et al. Chem Commun 2011;47:2116 with permission of The Royal Society of Chemistry [277]. (3) A bundle of SWCNTs filled with chromium oxide $CrO_3$. The arrow denotes the filled part of a nanotube from the bundle periphery. Adapted from Mittal J et al. Chem Phys Lett 2001;339:311. Copyright 2001, with permission from Elsevier [292]. (b) The nanotubes filled using solutions in supercritical $CO_2$ of (1) fullerene $C_{60}$, (2) $C_{61}(COOC_2H_5)_2$ and (3) $C_{61}(COOH)_2$. Below the micrographs, schematic structural models of the molecules are presented. Adapted from Britz DA et al. Chem Commun 2004:176 with permission of The Royal Society of Chemistry [298]. (c) The nanotubes filled *via* the melt approach. (1) Elementary iodine inside the SWCNTs. Upper part: High resolution atomic number-contrast scanning TEM image of a nanotube containing two strands of iodine. Lower part: The maximum entropy processed image with the reduced noise. The white dots are guide for eyes to see two chains of iodine atoms. Their periodicity is ~12.5 nm. Reprinted figure with permission from Fan X et al. Phys Rev Lett 2000;84:4621. Copyright 2000 by the American Physical Society [28]. (2) A bundle of SWCNTs filled with elementary tellurium. Reprinted from Chernysheva MV et al. Physica E 2008;40:2283. Copyright 2008, with permission from Elsevier [303]. (3) The 1D crystal of tin fluoride $SnF_2$ inside an individual SWCNT. Reprinted from Zakalyukin RM et al. Carbon 2008;46:1574. Copyright 2008, with permission from Elsevier [322]. (4) The 1D crystal of erbium chloride $ErCl_3$ inside an individual SWCNT. Adapted from Kitaura R et al. Nano Res 2008;1:152 [318].

Using supercritical $CO_2$ as a solvent in the solution filling process performed at high pressure (~150 bar) and usually low temperature (~50 °C) allowed encapsulating inside the SWCNTs fullerene $C_{60}$ [297–299] and its exotic derivatives, such as azafullerene $C_{59}N$ [242], endohedral fullerene $Er_3N@C_{80}$ [299], exohedral fullerene $C_{60}O$ [300] and functionalized fullerenes ($C_{61}(COOH)_2$, $C_{61}(COOC_2H_5)_2$ [298,299] and $C_{60}$ with alkyl chains [301]) (Table 1). The filling of the SWCNTs in supercritical carbon dioxide is a promising approach, because this solvent possesses very low viscosity and surface tension coefficient [56].

Fig. 19b demonstrates the HRTEM data of SWCNTs filled with $C_{60}$, $C_{61}(COOC_2H_5)_2$ and $C_{61}(COOH)_2$ in supercritical $CO_2$ and the schematic structural models of the molecules [298]. The micrograph of the $C_{60}$-filled nanotube (Fig. 19b1) represents the densely packed fullerene molecules inside the SWCNT channel, which are observed as circled contrast elements. The filling degree of nanotubes was estimated to be 30%. The image of the $C_{61}(COOC_2H_5)_2$-filled SWCNTs (Fig. 19b2) proves the encapsulation of the molecules inside the nanotubes. Authors of Ref. [298] noted that the functionalized fullerene molecules were more sensitive to the electron beam than $C_{60}$ molecules. They became elongated under HRTEM imaging conditions in a few seconds and then aggregated into polymeric chains, which is seen in Fig. 19b2. The estimated filling degree of nanotubes was 60%. The increase in the filling degree in comparison with $C_{60}$ was attributed to the presence of the diethyl ester functional groups. The micrograph in Fig. 19b3 shows the $C_{61}(COOH)_2$-filled SWCNTs. These molecule functionalized

with polar groups has significantly larger size than $C_{60}$ and $C_{61}(COOC_2H_5)_2$. As a result, the encapsulation of $C_{61}(COOH)_2$ inside the SWCNTs is sterically prohibited, and the filling degree of nanotubes was estimated to be less than 1% [298]. Authors of Ref. [298] noted that the $C_{61}(COOH)_2$ molecules were very unstable under the electron beam and degraded rapidly forming polymeric structures, which is observed in Fig. 19b3.

The method of filling the SWCNTs with melts of desired substances is as feasible as the solution filling method described above, moreover, using this approach allows achieving high filling degrees of the nanotube channels. The key parameters of the filling procedure are the melting temperature of the substance, surface tension coefficient of the melt and its viscosity. The melting point of the substance to insert cannot be higher than 1000–1200 °C, because the nanotubes start to degrade at higher temperatures. Also, it was shown that for the successful filling of SWCNTs with a substance the surface tension coefficient of its melt should not exceed 180 mN/m [55,56,110,354].

These parameters limit the list of substances that can be introduced into the nanotubes using the melt method. However, the use of this method allowed filling the SWCNT channels with a vast number of different substances, including simple substances (iodine [28,31,302], sulfur, selene and tellurium [303]), different metal halogenides (fluorides ($SnF_2$ [322]), chlorides ($M^{I}Cl$, where M = Na/Cs/Cu/Ag/Tl [21,41,56,306–308], $M^{II}Cl_2$, where M = Fe/Co/Ni/Mn/Pd/Zn/Cd [19,41,56,310,312–314,316,317,320], $M^{III}Cl_3$, where M = Y/Au/La/Nd/Sm/Eu/Gd/Tb/Ho/Tm/Er/Yb, $Al_2Cl_6$ [19,39,41,56,304,315,317,318,320,321], $M^{IV}Cl_4$, where M = Zr/Hf/Pt/Th [19,24,33,41,42,320], $M^{V}Cl_5$, where M = Mo [56], $M^{VI}Cl_6$, where M = W [41,56], $(KCl)_x(UCl_4)_y$ [21,44]), bromides ($M^{I}Br$, where M = Cs/Cu/Ag [21,41,306,307], $M^{II}Br_2$, where M = Fe/Co/Ni/Mn/Zn/Cd [310–314,316]), iodides ($M^{I}I$, where M = Li/Na/K/Rb/Cs/Cu/Ag [24,27,32–35,37,40–42,44,305–307,319], $M^{II}I_2$, where M = Ca/Sr/Ba/Fe/Co/Zn/Cd/Pb [24,29,33,38,42,43,310,314,316], $M^{III}I_3$, where M = La, $Al_2I_6$ [30,309,320], $M^{IV}I_4$, where M = Sn [41,56]) and their mixtures ($AgCl_{0.2}Br_{0.8}$ [21], $AgCl_{1-x}I_x$ [26,41,44] and $AgCl_xBr_yI_z$ [21,24,27,56])), chalcogenides (HgTe [324,327], SnSe [33], SnTe [36,323], GaSe [315,328], $MnTe_2$ [325,326], $Bi_2Te_3$ [315], $CdBr_{2-x}Te_x$ [24]), oxides (PbO [25], $Sb_2O_3$ [330,331], $Cr_2O_3$ [329]) and hydroxides (CsOH, KOH [45]) (Table 1). As for the solution filling method, the encapsulation of metal salt melts inside the SWCNTs and their subsequent chemical transformation allows filling the nanotube channels with metal nanoparticles, which cannot be incorporated inside the SWCNT channels using a one-step approach, because of their too high melting temperatures.

The filling process of nanotubes with melts usually requires a long period of time (several days), which is necessary for heating of the substance to a temperature higher than its melting point by several tens of degrees, exposure of the substance at this temperature and slow cooling down of the system. The optimization of time and temperature of the filling procedure allows achieving high filling degrees of the nanotube channels (up to 90%), and the optimization of cooling procedure of a system enables synthesizing one-dimensional nanocrystals with well-ordered structures and homogenous morphologies inside the SWCNT channels, which is difficult to achieve with the other filling methods.

Fig. 19c shows the HRTEM data of SWCNTs filled by the melt method. Fig. 19c1 presents the atomic number-contrast scanning TEM images of the iodine-filled nanotubes [28]. These dark field images, which were taken from an individual SWCNT, directly reveal the distribution of iodine atoms inside the nanotube channel due to large contrast between iodine and carbon. In the upper image two strands of iodine are visible. The observed variations in projected atomic positions and intensities, which make the image noisy, were explained by displacements of individual atoms during the imaging process [28]. The lower part of Fig. 19c1 represents the maximum entropy processed image with the reduced noise. Two chains of iodine atoms are observed, as indicated by the white dots. The projected spacing between the chains modulates along the tube axis, and two constrictions are seen. This testifies to a helical structure of the chains in three dimensions. The period of the modulation was measured to be ~12.5 nm [28]. Authors of Ref. [28] noted that different periodicities were observed for different nanotubes. This was explained by the fact that the iodine chains adopted preferred orientations with respect to the tube walls inside SWCNTs of different chiralities.

Fig. 19c2 demonstrates the HRTEM image of a bundle of tellurium-filled SWCNTs [303]. Dark contrast elements are observed inside the nanotube channels, which corresponds to continuous filling of SWCNTs. A certain periodicity is visible for the contrast elements, however the structure of 1D

crystals is not perfect. Authors of Ref. [303] explained this observation by the disproportion of inner diameter of SWCNT channel and Te ionic radius.

Fig. 19c3 shows the micrograph of an individual SWCNT filled with tin fluoride $SnF_2$ [322]. The ordered arrangement of contrast elements is clearly seen inside the nanotube channel. They correspond to structure fragments of the encapsulated compound. This proves the formation of the 1D $SnF_2$ nanocrystal with well-ordered structure within the SWCNT walls. The X-ray diffraction analysis also showed the existence of the $SnF_2$ crystalline phase in the sample [322].

Fig. 19c4 presents the HRTEM image of the $ErCl_3$-filled nanotube [318]. Two columns of dark ellipsoidal contrast elements aligned in a regular fashion are clearly visible inside the SWCNT channel. This regular array indicates the formation of 1D $ErCl_3$ crystal. The chemical composition of the filler was confirmed by the energy-dispersive X-ray analysis. The filling degree of nanotubes estimated from the HRTEM data was more than 90% [318].

*5.2.4. Filling the SWCNTs using plasma*

The SWCNTs can be filled *via* their exposure to ions generated in plasma. This method was successfully applied for the filling of nanotubes with metallic cesium [332–334], iodine [334], fullerene $C_{60}$ [334,335] and simultaneous encapsulation of several substances [334]. The high filling degrees of nanotube channels (50% for fullerene $C_{60}$) were achieved in a process that was carried out for short period of time (1 h). It should be noted that this filling method does not require preliminary opening of the SWCNT ends, because accelerated ions possessing kinetic energy of about 150 eV (for $Cs^+$) can penetrate into the SWCNT channels through their walls [56]. Fig. 20 shows the typical HRTEM images of the SWCNTs filled with atoms and molecules using plasma [334]. Fig. 20a demonstrates the micrograph of fullerene $C_{60}$-filled SWCNTs, where molecules are clearly seen inside the nanotube channel. The encapsulated cesium and iodine atoms were found to form chainlike structures inside the SWCNTs, as shown in Fig. 20b, d and c, e, respectively. The micrographs of the SWCNTs filled simultaneously with two different substances – $C_{60}$ molecules and Cs atoms are presented in Fig. 20f and g. They demonstrate that one-dimensional rowlike structures of cesium atoms and clearly aligned fullerene $C_{60}$ molecules are contiguously encapsulated inside the SWCNT channel. The junction area of Cs atoms and $C_{60}$ molecules is emphasized in the inset in Fig. 20f.

*5.2.5. Chemical reactions inside the SWCNT channels*

If a substance cannot be incorporated into the SWCNTs in a one-step approach, the filling can be performed *via* chemical reactions inside SWCNT channels. This filling method is very promising for the encapsulation of metals and other high-melting substances inside the SWCNTs. At first the nanotubes are filled with precursors for the desired substances by one of the aforementioned approaches. And after that their chemical modification is performed, which can be realized in several ways.

The first of these ways is the thermal decomposition of inserted compounds. It was shown that annealing the nanotubes filled with silver nitrate by the solution method at temperatures of 300–350 °C allows synthesizing silver nanoparticles inside the SWCNTs [19,22,46,293,294,296,315]. The other example is the synthesis of W, Re and Os clusters inside the nanotube channels *via* the thermal decomposition of metal carbonyls introduced into the SWCNTs by the gas phase filling method [336,337] (Table 1). Fig. 21a demonstrates the micrograph of the Os cluster-filled nanotubes [336]. The metal nanoparticles with a spheroidal shape are observed inside the SWCNT channels. Their average diameter is ~1 nm, and the size and shape distribution is relatively monodispersed. On the basis of the HRTEM data authors of Ref. [336] concluded that 85–95% of SWCNTs are filled with the metallic nanoparticles, which are crystalline structures exhibiting clear faceting and staking of atomic planes and hetero-epitaxial relations to the nanotube walls. The host SWCNTs act as both a template and stabilizer for the nanoparticles, controlling their size and morphology.

The chemical modification of a precursor can also be conducted by its photolytic decomposition. This approach was demonstrated in Ref. [21]. The authors firstly filled the SWCNTs with silver chloride by the melt method and then decomposed it for the formation of metallic silver. Fig. 21b shows the micrograph of the obtained silver-filled SWCNTs. The observed individual large diameter nanotube ($d_t$ = 3.8 nm, which corresponds, for instance, to a (28,28) SWCNT) is completely filled with 17 layers

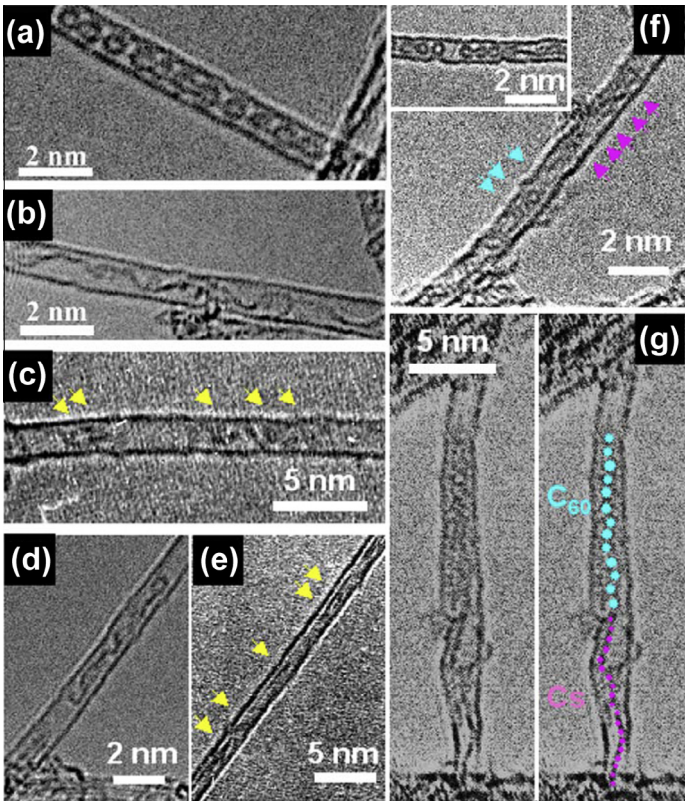


**Fig. 20.** The HRTEM data of SWCNTs filled using plasma with $C_{60}$ fullerene molecules (a), chains of cesium atoms (b and d), iodine atoms (c and e), $C_{60}$ molecules and Cs atoms simultaneously (f and g). The yellow arrows in (c and e) denote the encapsulated iodine atoms. The light blue and pink arrows and dots in (f and g) are guide for eyes to see the incorporated $C_{60}$ molecules and Cs atoms, respectively. The inset in (f) emphasizes the junction area of $C_{60}$ molecules and Cs atoms. Reprinted with permission from Kato T et al. Appl Phys Lett 2009;95:083109. Copyright 2009, AIP Publishing LLC [334].

of silver metal. The *d*-spacing of the filler was measured to be 2.04 ± 0.05 Å, as denoted on the micrograph, which corresponds to the (200) *d*-spacing of silver metal [21].

The most often used method of the chemical transformation of incorporated precursors is their heating in a reducing atmosphere. The precursors can be encapsulated into the SWCNT channels by the gas phase or liquid phase filling methods (from solution or melt). The chemical nature of precursors may be different. It was shown that the formation of metallic nanoparticles inside the SWCNT channels can be achieved *via* the heating in a hydrogen flow of nanotubes filled with metal nitrates ($Bi(NO_3)_3$ [20], $Cu(NO_3)_2$ [293,295]), metal chlorides ($FeCl_3$ [290,291], $RuCl_3$ [6], $PdCl_2$ [19], $HAuCl_4$ [19], $H_2PtCl_6$ [19]), metal oxides ($Re_xO_y$ [18]) and organometallic compounds ($Co(C_5H_7O_2)_2$ [285]) (Table 1). Fig. 21c demonstrates the micrograph of the Ru-filled SWCNTs obtained from the $RuCl_3$ precursor [6]. An elongated Ru crystallite is observed inside the channel of one nanotube at the edge of a bundle of SWCNTs. The metal crystallite exhibits a preferred orientation with its *d*(101) lattice fringe aligning parallel to the SWCNT axis [6]. Fig. 21d shows the HRTEM image of the Au-filled SWCNTs obtained from the $HAuCl_4$ precursor [19]. The gold nanowires are observed inside the SWCNTs. They are single crystalline. The image reveals the resolved lattice of gold with a spacing of ~0.23 nm, corresponding to the (111) planes [19]. Fig. 21e demonstrates the micrograph of the Re-filled SWCNTs obtained from the rhenium oxide precursor [18]. The observed individual nanotube is filled with a long metallic nanowire that is composed of various agglomerated crystallites with different lattice orientations, as shown on the image by the white lines. The abrupt changes in crystallite orientations

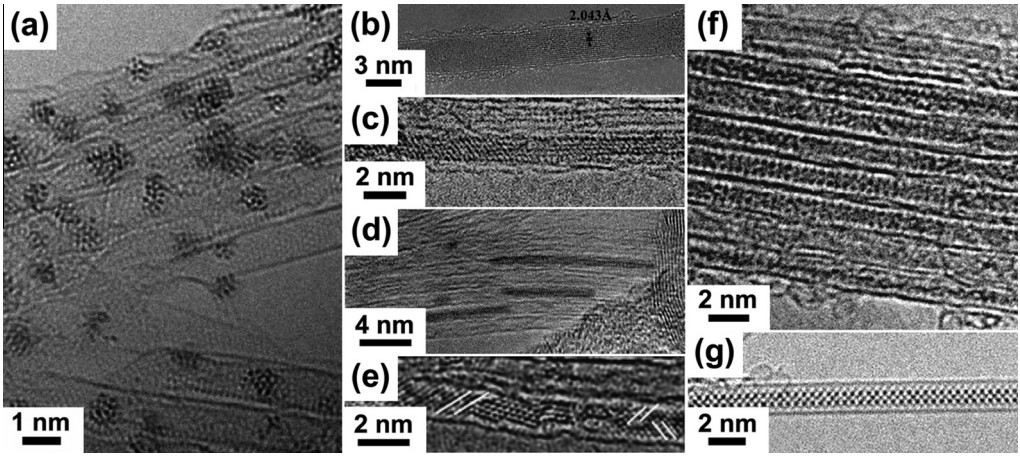


**Fig. 21.** The HRTEM data of SWCNTs filled *via* chemical reactions inside their channels with osmium nanoparticles (a) (adapted from Chamberlain TW et al. Chem Sci 2012;3:1919 with permission of The Royal Society of Chemistry [336]), silver crystallite (b) (adapted from Sloan J et al. Chem Commun 1999:699 with permission of The Royal Society of Chemistry [21]), ruthenium crystallite (c) (adapted from Sloan J et al. Chem Commun 1998:347 with permission of The Royal Society of Chemistry [6]), gold nanowires (d) (adapted with permission from Govindaraj A et al. Chem Mater 2000;12:202. Copyright 2000 American Chemical Society [19]), rhenium nanowire (e) (adapted with permission from Costa PMFJ et al. Chem Mater 2005;17:6579. Copyright 2005 American Chemical Society [18]), cadmium sulfide (f) and lead telluride (g) 1D crystals (adapted with permission from Eliseev AA et al. Chem Mater 2009;21:5001. Copyright 2009 American Chemical Society [338]). In (b) the measured (200) *d*-spacing of the silver crystallite is indicated. In (e) the white lines denote different lattice orientations of various agglomerated crystallites forming the rhenium nanowire.

are accompanied by localized distortions of the nanotube walls. The lattice spacings for the encapsulated crystallites were well defined and in agreement with those of rhenium metal [18].

It was demonstrated in Ref. [338] that the substitution reaction can be carried out inside the SWCNT channels. On the first step of the synthesis, the SWCNTs were filled with low-melting cadmium, zinc or lead iodides. After that, the obtained nanostructures were filled with melts of sulfur or tellurium. It led to the substitution of iodine atoms to chalcogene atoms. Finally, the nanotubes filled with one-dimensional nanocrystals of high-melting CdS, ZnTe and PbTe were obtained, which could not be encapsulated into the SWCNTs *via* a one-step filling method because of their too high melting temperatures [338]. Fig. 21f shows the micrograph of a bundle of the CdS-filled SWCNTs. The periodically placed contrast elements are clearly visible inside the SWCNT channels, which correspond to the continuous one-dimensional CdS crystals. The HRTEM image of an individual nanotube filled with PbTe is presented in Fig. 21g. It demonstrates rows of contrast elements periodically located within the SWCNT channel. This confirms a perfect structure of the encapsulated one-dimensional crystal. Authors of Ref. [338] noted that local energy dispersive X-ray analysis proved the chemical compositions of the desired compounds inside the nanotubes.

The special group of chemical reactions carrying out inside the SWCNT channels is reactions yielding DWCNTs (i.e., with inner tube growth inside the outer SWCNTs). It was firstly demonstrated in 2001 that the DWCNTs can be formed by the transformation of carbon-rich precursor molecules inside the SWCNTs [339]. There it was shown that the annealing at 1000 °C of $C_{60}$ peapods, synthesized by the gas phase method, leads to the growth of inner tubes in a high yield. Later on, other authors reported on the synthesis and investigation of the growth process and structure of DWCNTs formed from SWCNTs filled with $C_{60}$ [340–348] and $C_{70}$ [341,342] fullerene molecules. The interest to these nanostructures was caused by the fact that the growth of inner tubes took place in a highly shielded environment and without any additional catalyst [340,345], which is very special as compared to traditional methods of the DWCNT synthesis. It opened the way to the detailed investigation of nanotube formation in a clean room of about 1.4 nm width [345]. Besides, filling SWCNTs with isotope-labeled fullerene molecules provided the possibility to produce DWCNTs with $^{13}C$ enriched inner and natural $^{12}C$ outer tubes [341].

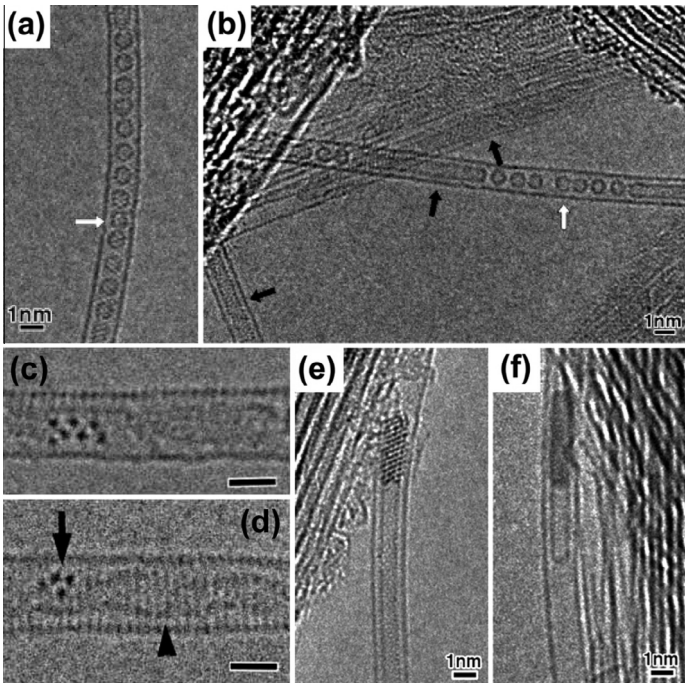


**Fig. 22.** The HRTEM images of DWCNTs grown from the filled SWCNTs. Fullerene $C_{60}$-filled SWCNTs transformed to DWCNTs by annealing at 1250 °C for 5 min (a) and 25 min (b). The white arrows indicate the fullerene molecules that are in the process of coalescence. The black arrows denote the formed DWCNTs. Adapted with permission from Pfeiffer R et al. Nano Lett 2007;7:2428. Copyright 2007 American Chemical Society [345]. Ce-containing DWCNTs obtained by annealing of cerocene-filled SWCNTs at 1000 °C (c and d). The scale bar is 1 nm. In (d) the black arrows show the grown inner tube and the encapsulated cerium. Reprinted figure with permission from Shiozawa H et al. Phys Rev Lett 2009;102:046804. Copyright 2009 by the American Physical Society [51]. Pt-containing DWCNTs obtained as result of *ex situ* annealing of Pt acetylacetonate-filled SWCNTs at 700 °C (e) and *in situ* annealing at temperatures up to 760 °C (f). Reprinted with permission from Shiozawa H et al. Adv Mater 2010;22:3685. Copyright 2010 Wiley-VCH Verlag GmbH & Co. KGaA, Weinheim [266].

The HRTEM images in Fig. 22a and b illustrate the process of the DWCNT growth from fullerene $C_{60}$-filled SWCNTs after annealing at 1250 °C for 5 min and 25 min, respectively [345]. After 5 min, there are still a considerable number of pristine fullerene $C_{60}$ molecules inside the SWCNT channel. However, coalescence has already started to a certain degree, as denoted by the white arrow (Fig. 22a). After 25 min, the DWCNTs dominate clearly in the sample, as indicated by the black arrows. Also, there are still some fullerenes left that are in the process of clustering together, as shown by the white arrow (Fig. 22b).

It was demonstrated that the DWCNTs can be also formed using fullerene derivatives as precursors. In Refs. [49,250,256], endohedral fullerene $Gd@C_{82}$ was chosen as a precursor. The molecules were incorporated into the SWCNT channels using the gas phase filling method. After that, the high-vacuum high-temperature heat treatment at 1300–1400 °C of the filled nanotubes was performed, which led to the formation of DWCNTs encapsulating Gd nanowires.

It was shown that the DWCNTs can be formed *via* the chemical transformation of metallocenes inserted into the SWCNT channels. In 2007, the DWCNTs were firstly formed as result of the thermal treatment of SWCNTs filled with ferrocene molecules by the gas phase approach [264]. Later on, other authors reported on the synthesis and investigation of similar samples [50,257–261,265–268,284]. It was demonstrated that metallocene molecules were decomposed upon annealing, and they acted as catalyst source and provided carbon atoms for the inner tube growth at the same time. The annealing of ferrocene-filled SWCNTs led to the formation of iron carbide-filled DWCNTs at temperatures as low

as 600 °C. The possibility of the DWCNT formation was also reported for the nanotubes filled with cerocene by the gas phase method [51,269]. Fig. 22c and d demonstrates the HRTEM images of individual Ce-containing DWCNTs obtained by annealing of cerocene-filled SWCNTs at 1000 °C [51]. The indulating lines clearly seen in between the outer tube walls correspond to the grown inner nanotubes. The observed dark dots are from the encapsulated cerium.

The growth of inner tubes was also observed during the thermal treatment of SWCNTs filled with platinum acetylacetonate [266,270]. This chemical compound was introduced into the SWCNT channels using the methods from solution [266,270] or gas phase [270]. The annealing of filled nanotubes at temperatures higher than 700 °C led to the formation of platinum-containing DWCNTs. As in the case of metallocenes, platinum acetylacetonate acted as the source of catalyst and carbon for the growth of inner nanotubes. Fig. 22e demonstrates the HRTEM micrographs of Pt-containing DWCNTs obtained as result of *ex situ* annealing of Pt acetylacetonate-filled SWCNTs at 700 °C [266]. An inner nanotube is observed inside an outer SWCNT. The open end of the inner tube is connected to a nanocrystal inside the SWCNT. The interplanar distances of this nanocrystal agree with those of a platinum crystal. These data testify that the platinum nanocrystal nucleates and grows the inner nanotube. Fig. 22f shows the micrograph of Pt-containing DWCNTs obtained as result of *in situ* annealing of Pt acetylacetonate-filled SWCNTs at temperatures up to 760 °C [266]. As follows from the data, the inner tube wall remains terminated at the platinum nanocrystal even at the high growth temperature. The growth stops when there is no more carbon source, but the inner tube end remains on the Pt surface [266].

It was found that the DWCNTs can also be grown from precursors that contain neither catalytic nanoparticles nor preformed cap structures. The carbon atoms of toluene were shown in isotope-substitution experiments to enter the inner nanotube walls if the toluene was filled into the SWCNTs simultaneously with fullerene $C_{60}$ molecules [349]. Also, the transformation to DWCNTs was observed for anthracene [350].

## 6. Modification of SWCNT electronic properties by filling the channels

The filling of the SWCNT channels may lead to a charge transfer and the formation of chemical bonds between the encapsulated substances and the nanotube walls [53,355]. If the charge transfer takes place without chemical bonding, the modification of the nanotube electronic structure can be considered in the rigid band model as a simple shift of the SWCNT Fermi level. In general, there are three possible types of the modification of the SWCNT electronic properties that can happen as a result of filling their channels: (1) acceptor doping accompanied by the charge transfer from the nanotube walls to incorporated substances and lowering the SWCNT Fermi level, (2) donor doping accompanied by the charge transfer from the encapsulated substances to the SWCNTs and rising the nanotube Fermi level and (3) no doping of nanotubes.

The type of modification of the SWCNT electronic properties depends on the chemical and physical properties of the encapsulated substance. The different molecules (fullerenes, endohedral fullerenes, organic and organometallic molecules), simple substances (metals and nonmetals), chemical compounds (metal halogenides and chalcogenides, oxides) possess acceptor and donor properties. These substances can be inserted into the nanotube channels using the gas phase and liquid phase (solution and melt) filling methods, using plasma or *via* chemical reactions. In general, the filling method depends on the type of substance; that is why the methods of encapsulating potential acceptors and donors of electrons inside the SWCNTs differ.

There are reports dedicated to the experimental and theoretical investigations of the above listed types of modification of the electronic properties of filled SWCNTs. Experimental approaches allowed studying the modified electronic structure of SWCNTs on a qualitative level (i.e., identification of the charge transfer and its direction) and also quantitative level (i.e., measuring the work function, determination of the Fermi level position and its shift relative to the initial position). These investigations were performed using the state-of-the-art spectroscopic techniques, such as Raman spectroscopy, X-ray photoelectron spectroscopy, X-ray emission spectroscopy, optical absorption spectroscopy, X-ray absorption spectroscopy, ultraviolet photoelectron spectroscopy and photoluminescence

spectroscopy. The characteristic modification of spectra of filled nanotubes as compared to the ones of pristine SWCNTs testified to the corresponding changes in the electronic properties of SWCNTs. Theoretical investigations of the electronic properties of filled nanotubes were carried out using quantum-chemical modeling methods.

### 6.1. Acceptor doping

#### 6.1.1. Typical acceptors of electrons and methods of their encapsulation

According to the reports on the experimental and theoretical studies of the electronic properties of filled SWCNTs, the following substances have an acceptor doping effect on the SWCNTs: different molecules – organic molecules (tetracyano-*p*-quinodimethane (TCNQ) and tetrafluorocyano-*p*-quinodimethane ($F_4$TCNQ) [48,356]), fullerenes ($C_{60}$ [240,357–363], $C_{70}$, $C_{78}$, $C_{82}$ [360–362]), endohedral fullerenes (Gd@$C_{82}$ [49,256], La@$C_{82}$, K@$C_{60}$, Ca@$C_{60}$, Y@$C_{60}$ [358,360]), simple substances – nonmetals (S, Se, Te [303]), chemical compounds – metal oxides ($CrO_3$ [46]), metal halogenides ($SnF_2$ [322], AgCl, AgBr, AgI [306], $FeCl_2$, $FeBr_2$, $FeI_2$ [310], $CoBr_2$ [311], $NiCl_2$, $NiBr_2$ [312], $MnCl_2$, $MnBr_2$ [313], $ZnCl_2$, $ZnBr_2$, $ZnI_2$ [314], $TbCl_3$, $ZnCl_2$, $CdCl_2$ [317], $TmCl_3$ [315], $ErCl_3$ [304], CuCl, CuBr, CuI [307], CuI [305,319], $CdCl_2$, $CdBr_2$, $CdI_2$ [316], KI [364]) and metal chalcogenides (GaSe [315,328]).

To incorporate acceptors of electrons into the SWCNT channels, different methods were used. The encapsulation of fullerene $C_{60}$ [240,357], organic molecules (TCNQ and $F_4$TCNQ [48]) and endohedral fullerene Gd@$C_{82}$ [49,256] was performed by the gas phase approach. This method is a convenient way of the synthesis of samples for further spectroscopic investigations, because it allows achieving the high filling degrees of the nanotube channels and obtaining clean samples. The effectiveness of this method was demonstrated earlier by the incorporation of different molecules inside the SWCNTs (see Section 5.2.2). That is possibly why the gas phase method was chosen to fill the SWCNTs with fullerene and organic molecules for the investigation of their modified electronic properties. However, it should be noted that this method is not the only approach that allows incorporating such electron acceptors as fullerenes and their derivatives into the SWCNT channels. It was shown that fullerenes can be encapsulated into the nanotubes by the *in situ* method during arc-discharge [12,14,234] and laser ablation [5,13,14,235] synthesis of SWCNTs. Furthermore, fullerene $C_{60}$ can be introduced into the SWCNT hollow core by the liquid phase method using its solution in organic solvent [14,241,275,276] or supercritical $CO_2$ [297–299] and by the plasma filling method [335].

The most widely employed approach for the encapsulation of electron acceptors inside the SWCNTs is the liquid phase method using melts, whose effectiveness was proven previously by filling the nanotubes with different simple substances and chemical compounds (see Section 5.2.3). There are reports dedicated to the investigation of the electronic properties of the SWCNTs filled by this method with chalcogenes (S, Se, Te [303]), metal halogenides ($SnF_2$ [322], AgCl, AgBr, AgI [306], $FeCl_2$, $FeBr_2$, $FeI_2$ [310], $CoBr_2$ [311], $NiCl_2$, $NiBr_2$ [312], $MnCl_2$, $MnBr_2$ [313], $ZnCl_2$, $ZnBr_2$, $ZnI_2$ [314], $TbCl_3$, $ZnCl_2$, $CdCl_2$ [317], $TmCl_3$ [315], $ErCl_3$ [304], CuCl, CuBr, CuI [307], CuI [305,319], $CdCl_2$, $CdBr_2$, $CdI_2$ [316]) and metal chalcogenides (GaSe [315,328]). The homogenous filling of nanotube channels with large filling degrees allowed precisely studying the modified electronic properties of the SWCNTs. It is worth noticing that there are also examples for the introduction of some of the above listed electron acceptors into the SWCNTs by other filling methods. The possibility of the gas phase encapsulation of elemental selene inside the nanotubes was demonstrated in Ref. [17]. Also, iron chloride was introduced into the SWCNTs by the solution method in Refs. [290,291]. The encapsulation of chromium oxide $CrO_3$ carried out in Ref. [46] was also performed *via* the solution method. The choice of the solution filling method instead of the melt method was caused by the high melting temperature of chromium oxide.

Fig. 23 shows the HRTEM data of SWCNTs filled with electron acceptors. Fig. 23a presents the cross-sectional image of a bundle of SWCNTs filled with endohedral fullerene Gd@$C_{82}$ molecules [250]. Inside the nanotube channels, which are seen as dark circles, circle contrast elements of the incorporated molecules are clearly visible.

Fig. 23b demonstrates the HRTEM image of the SWCNTs filled with elemental tellurium [303]. A bundle of nanotubes is observed. Their channels are evidently filled, because dark material is seen

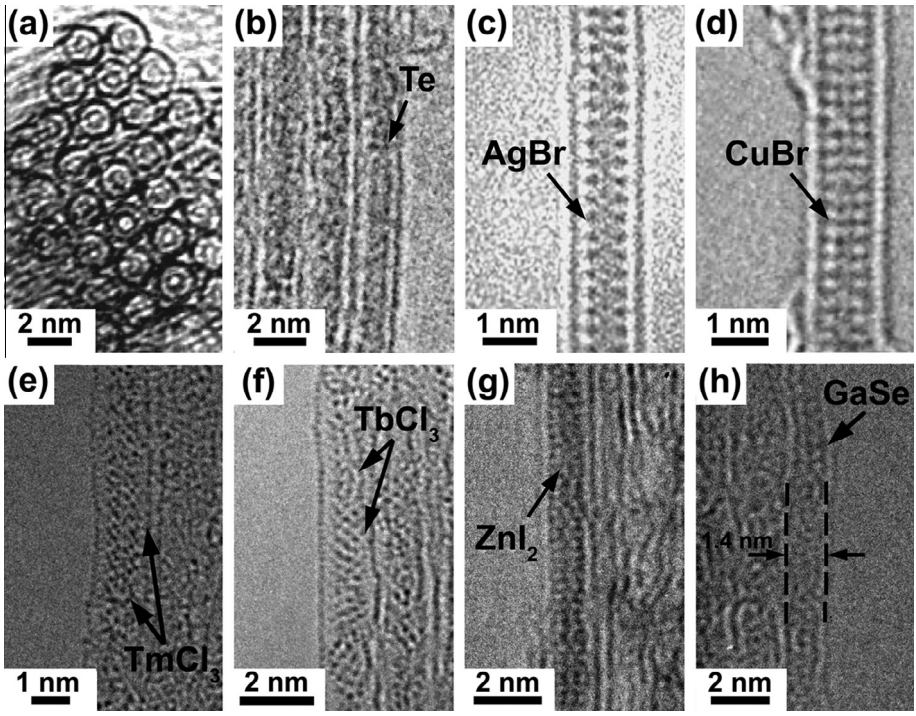


**Fig. 23.** The HRTEM data of SWCNTs filled with electron acceptors. (a) The cross-sectional image of a bundle of SWCNTs filled with endohedral fullerene Gd@$C_{82}$ molecules. Adapted with permission from Kitaura R et al. Nano Lett 2008;8:693. Copyright 2008 American Chemical Society [250]. (b) A bundle of SWCNTs filled with elemental tellurium. Adapted from Chernysheva MV et al. Physica E 2008;40:2283. Copyright 2008, with permission from Elsevier [303]. Individual SWCNTs filled with 1D crystals of silver bromide (c) (adapted from Eliseev AA et al. Carbon 2010;48:2708. Copyright 2010, with permission from Elsevier [306]) and copper bromide (d) (adapted from Eliseev AA et al. Carbon 2012;50:4021. Copyright 2012, with permission from Elsevier [307]). The SWCNTs from the bundle periphery filled with 1D crystals of thulium chloride (e) (reprinted from Kharlamova MV et al. Appl Phys A 2013;112:297. Copyright 2013 Springer-Verlag Berlin Heidelberg, with kind permission from Springer Science and Business Media [315]), terbium chloride (f) (reprinted from Kharlamova MV. Appl Phys A 2013;111:725. Copyright 2013 Springer-Verlag Berlin Heidelberg, with kind permission from Springer Science and Business Media [317]), zinc iodide (g) (the data are from Ref. [314]) and gallium selenide (h) (reprinted from Kharlamova MV et al. Appl Phys A 2013;112:297. Copyright 2013 Springer-Verlag Berlin Heidelberg, with kind permission from Springer Science and Business Media [315]). The arrows indicate the encapsulated materials. In (h) the nanotube walls are also marked by the dashed vertical lines, and the SWCNT diameter is shown by the horizontal arrows.

between the SWCNT walls, as denoted by the arrow. It is visible that the encapsulated Te does not form 1D crystals with well-ordered structure inside SWCNTs.

Fig. 23c shows the micrograph of an individual SWCNT filled with silver bromide [306]. It confirms the continuous encapsulation of AgBr into the nanotube channel (as indicated by the arrow) and absence of salt particles on the SWCNT external surface. The observed dark contrast elements are periodically placed within the nanotube channel, which testifies to the formation of the well-ordered 1D crystal. The visible pattern originates from the bromine atom arrangement. The reconstruction of the 1D crystal structure showed that the large bromide anions form a two-layered hexagonal closely-packed array, and silver cations are located in tetrahedral sites [306]. From an analysis of the HRTEM data for this sample, the filling degree of SWCNTs with AgBr and its crystallization factor were estimated to be ~60% [306].

Fig. 23d demonstrates the micrograph of an individual copper bromide-filled nanotube [307]. The ordered arrangement of contrast elements (denoted by the arrow) inside the channel confirms the growth of fine 1D CuBr crystal. Its modeled structure was represented as a column of hexagonal

**Table 2**
Typical acceptors of electrons, methods of their encapsulation inside the SWCNT channels and methods of investigation of the electronic properties of the obtained nanostructures.

| Type of substance | | Substance | Method of encapsulation | Methods of investigation of electronic properties[c] | Reference |
|---|---|---|---|---|---|
| Molecule | Organic molecule | TCNQ[a], $F_4$TCNQ[b] | Gas phase | OAS, RS | [48] |
| | | | – | QM | [356] |
| | Fullerene | $C_{60}$ | Gas phase | XAS | [357] |
| | | | | UPS | [240] |
| | | | – | QM | [358–363] |
| | | $C_{70}$, $C_{78}$, $C_{82}$ | – | QM | [360–362] |
| | Endohedral fullerene | Gd@$C_{82}$ | Gas phase | XPS, UPS, XAS | [49,256] |
| | | La@$C_{82}$, K@$C_{60}$, Ca@$C_{60}$, Y@$C_{60}$ | – | QM | [358,360] |
| Simple substance | Nonmetal | S, Se, Te | Liquid phase (melt) | RS | [303] |
| Chemical compound | Metal oxide | $CrO_3$ | Liquid phase (solution) | RS | [46] |
| | | | – | QM | [365] |
| | Metal halogenide | $SnF_2$ | Liquid phase (melt) | RS | [322] |
| | | AgCl, AgBr, AgI | | OAS, RS, RS + EC charging, XAS, XPS | [306] |
| | | $FeCl_2$, $FeBr_2$, $FeI_2$ | | OAS, RS, XAS, XPS | [310] |
| | | $CoBr_2$ | | OAS, RS, XPS | [311] |
| | | $NiCl_2$, $NiBr_2$ | | OAS, RS, XAS, XPS | [312] |
| | | $MnCl_2$, $MnBr_2$ | | OAS, RS, XPS | [313] |
| | | $ZnCl_2$, $ZnBr_2$, $ZnI_2$ | | OAS, RS, XAS, XPS, WF, UPS | [314] |
| | | $TbCl_3$, $ZnCl_2$, $CdCl_2$ | | OAS, RS, XPS | [317] |
| | | $TmCl_3$ | | RS, XPS | [315] |
| | | $ErCl_3$ | | XPS, UPS, XAS | [304] |
| | | CuCl, CuBr, CuI | | XAS, XES, OAS, RS, RS + EC charging, XPS, WF, UPS | [307] |
| | | CuI | | RS | [305,319] |
| | | $CdCl_2$, $CdBr_2$, $CdI_2$ | | OAS, RS, XAS, XPS | [316] |
| | | KI | – | QM | [364] |
| | Metal chalcogenide | GaSe | Liquid phase (melt) | OAS, RS, XAS, XPS | [315,328] |

[a] TCNQ = tetracyano-*p*-quinodimethane.
[b] $F_4$TCNQ = tetrafluorocyano-*p*-quinodimethane.
[c] OAS = optical absorption spectroscopy, RS (+EC charging) = Raman spectroscopy (with electrochemical charging), QM = quantum-chemical modeling, XAS = X-ray absorption spectroscopy, UPS = ultraviolet photoelectron spectroscopy, XPS = X-ray photoelectron spectroscopy, WF = work function measurements, XES = X-ray emission spectroscopy.

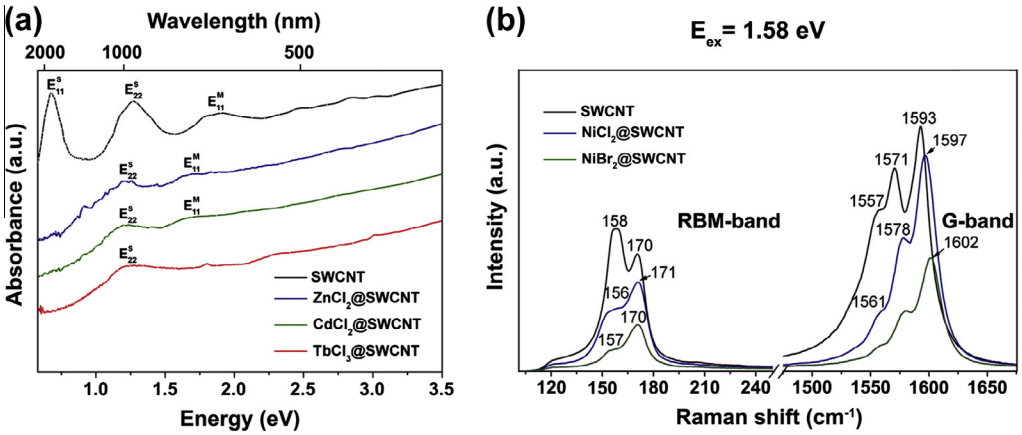


**Fig. 24.** (a) The optical absorption spectra of the pristine SWCNTs and $ZnCl_2$@SWCNT, $CdCl_2$@SWCNT and $TbCl_3$@SWCNT nanostructures. The peaks corresponding to the first and the second vHs of semiconducting SWCNTs and the first vHs of metallic SWCNTs are denoted by symbols $E^S_{11}$, $E^S_{22}$ and $E^M_{11}$, respectively. Reprinted from Kharlamova MV. Appl Phys A 2013;111:725. Copyright 2013 Springer-Verlag Berlin Heidelberg, with kind permission from Springer Science and Business Media [317]. (b) The RBM- and G-bands of the Raman spectra of the pristine SWCNTs and $NiX_2$@SWCNT samples measured at a laser excitation energy of 1.58 eV. The numbers denote the positions of the peaks. Reprinted with permission from Kharlamova MV et al. Phys Status Solidi B 2012;249:2328. Copyright 2012 Wiley-VCH Verlag GmbH & Co. KGaA, Weinheim [312].

closely-packed $(Br)_{3n}$ triangles with the copper cations located either in tetrahedral or octahedral positions [307]. The estimated filling degree of SWCNTs with CuBr and its crystallization factor amounted to 60% and 50%, respectively [307].

The HRTEM images of the SWCNTs filled with thulium chloride (Fig. 23e) [315], terbium chloride (Fig. 23f) [317], zinc iodide (Fig. 23g) [314] and gallium selenide (Fig. 23h) [315] show the SWCNTs from the bundle periphery. In all cases, contrast elements are seen inside the nanotube channels, as marked by the arrows, which proves the incorporation of the compounds inside the SWCNTs. Their ordered patterns testify to the formation of 1D crystals. No nanoparticles are visible on the external surface of SWCNTs. On the basis of the HRTEM data, the filling degree of nanotubes was estimated to be 70–80% for $TmCl_3$ [315], 50–60% for $TbCl_3$ [317] and 60% for $ZnI_2$ [314] and GaSe [315]. The local energy dispersive X-ray analysis confirmed the stoichiometry of the embedded compounds.

Table 2 summarizes typical acceptors of electrons, methods of their encapsulation inside the nanotube channels and methods of investigation of the electronic properties of the obtained nanostructures.

### *6.1.2. Characterization of electronic properties of SWCNTs filled with electron acceptors*

*6.1.2.1. Experimental methods.* The identification of the charge transfer and its direction in the nanotubes filled with electron acceptors was performed using optical absorption spectroscopy and Raman spectroscopy. The determination of the Fermi level and its shift as compared to the initial position was performed using Raman spectroscopy under electrochemical charging, X-ray photoelectron spectroscopy, ultraviolet photoelectron spectroscopy and work function measurements. The chemical bonding between the incorporated substances and the SWCNT walls was investigated using X-ray absorption spectroscopy.

Optical absorption spectroscopy (OAS) gives information about the presence of charge transfer in the filled nanotubes. Using this method it is impossible to determine the direction of charge transfer and to conclude which type of doping of SWCNTs takes place. However, optical absorption spectroscopy is a very useful approach for investigating the modification of the electronic properties of filled nanotubes. Fig. 24a shows the OAS spectra of the pristine nanotubes with a mean diameter of 1.4 nm and the SWCNTs filled with terbium, zinc and cadmium chlorides [317]. The spectrum of unfilled nanotubes has several characteristic peaks at energies in the range from 0.5 to 3 eV

corresponding to electronic transitions between van Hove singularities (vHs) of semiconducting and metallic nanotubes. According to the Kataura plot, for SWCNTs with a diameter of 1.4–1.6 nm the peak at the energy in the range from 0.6 to 0.8 eV can be assigned to the electronic transitions $E_{11}^{S}$ between the first vHs of semiconducting nanotubes. The peak at the energy of 1.0–1.4 eV corresponds to the electronic transitions $E_{22}^{S}$ between the second vHs of semiconducting nanotubes. The peak at the energy in the range of 1.7–2.0 eV belongs to the electronic transitions $E_{11}^{M}$ between the first vHs of metallic nanotubes. The peak at the energy of 2.3–2.5 eV corresponds to the electronic transitions $E_{33}^{S}$ between the third vHs of semiconducting nanotubes [75].

In the spectra of nanotubes filled with terbium, zinc and cadmium chlorides (Fig. 24a) the peak corresponding to the electron transitions between the first vHs of semiconducting nanotubes disappears, which testifies to the presence of the charge transfer in these nanostructures. It may occur from or to the nanotube walls. In the first case, the Fermi level of SWCNTs downshifts and the first vHs of the valence band of semiconducting nanotubes are emptied. The second case corresponds to an upshift of the SWCNT Fermi level accompanied by the filling of the first vHs of the conduction band of semiconducting nanotubes. The disappearance of the $E_{11}^{S}$ peak was also observed in the spectra of nanotubes filled with halogenides of iron [310], cobalt [311], nickel [312], manganese [313], zinc [314], silver [306], cadmium [316] and copper [307]. Also, the OAS spectra of the SWCNTs filled with organic molecules [48] were investigated (Table 2). These spectra demonstrated the decrease of intensity of the $E_{11}^{S}$ peak, which was explained by the presence of moderate charge transfer in the filled nanotubes.

Measuring the Raman spectra of filled SWCNTs at different laser wavelengths enables the resonance excitation of nanotubes of different diameters and conductivity type. It makes Raman spectroscopy a versatile tool to study the modified electronic properties of filled SWCNTs.

A Raman spectrum of SWCNTs consists of three main features [366]: a radial breathing mode (RBM) at frequencies typically below 200 $cm^{-1}$, which is assigned to synchronous radial vibrations of carbon atoms ($A_{1g}$ symmetry), a D-line between 1300 and 1350 $cm^{-1}$, which is optically forbidden, but is enabled at defect sites, and a G-band at frequencies of 1500–1600 $cm^{-1}$, which corresponds to C–C bond vibrations (A, $E_1$, $E_2$ symmetries [367]). The G-line is split into two most intense components [368]: the $G^-$-mode at low frequencies (about 1540 $cm^{-1}$) and the $G^+$-mode at high frequencies (about 1590 $cm^{-1}$). Both belong to longitudinal optical (LO) phonon (LO corresponds to the axial displacement of the atoms) in metallic ($G^-$) and semiconducting ($G^+$) SWCNTs [369]. The $G^+$ shows a shoulder on the low frequency side, it stems from the transversal optical (TO) phonon (TO corresponds to the circumferential displacement of the atoms) in semiconducting SWCNTs [369]. The shapes of the G-band of semiconducting and metallic SWCNTs are drastically different. The G-band of semiconducting nanotubes is a narrow symmetric peak with a Lorentzian shape. The G-band of metallic nanotubes has the broad asymmetric profile of a BWF function [366,370].

Fig. 24b shows the RBM- and G-bands of Raman spectra of pristine nanotubes and the SWCNTs filled with nickel halogenides, which were acquired at a laser energy of 1.58 eV [312]. The spectra of the filled nanotubes demonstrate the modification of peaks in the RBM-band, including the change of their shapes and shifts, which may be assigned to changes in the resonance excitation conditions of the SWCNTs as a result of filling their channels. Also, the spectra of the filled SWCNTs demonstrate the shift of the G-band peaks as well as a modification of their shapes. The same effects were observed in the Raman spectra of nanotubes filled with $CrO_3$ [46], CuCl, CuBr, CuI [305,307,319], S, Se, Te [303], $SnF_2$ [322], organic molecules [48], $FeCl_2$, $FeBr_2$, $FeI_2$ [310], $CoBr_2$ [311], $NiCl_2$, $NiBr_2$ [312], $MnCl_2$, $MnBr_2$ [313], $ZnCl_2$, $ZnBr_2$, $ZnI_2$ [314,317], $TbCl_3$ [317], $TmCl_3$ [315], AgCl, AgBr, AgI [306], $CdCl_2$, $CdBr_2$, $CdI_2$ [316,317] and GaSe [315,328]. In the earliest reports [46,48,303,305,319,322], it was discussed that the shift of the G-band peaks toward higher frequencies corresponded to the charge transfer from the nanotubes to the incorporated substances and the shift of the G-band peaks toward lower frequencies testified to the charge transfer from the encapsulated substances to the SWCNT walls. On the basis of this hypothesis, it was concluded that $CrO_3$ [46], S, Se, Te [303], CuI [305,319], $SnF_2$ [322] and organic molecules TCNQ and $F_4TCNQ$ [48] were electron acceptors. However, ambipolar electrochemical charging of SWCNTs showed that applying the positive potentials to the nanotubes, which is analogous to donor doping, may also lead to hardening of the G-band [371]. That is why

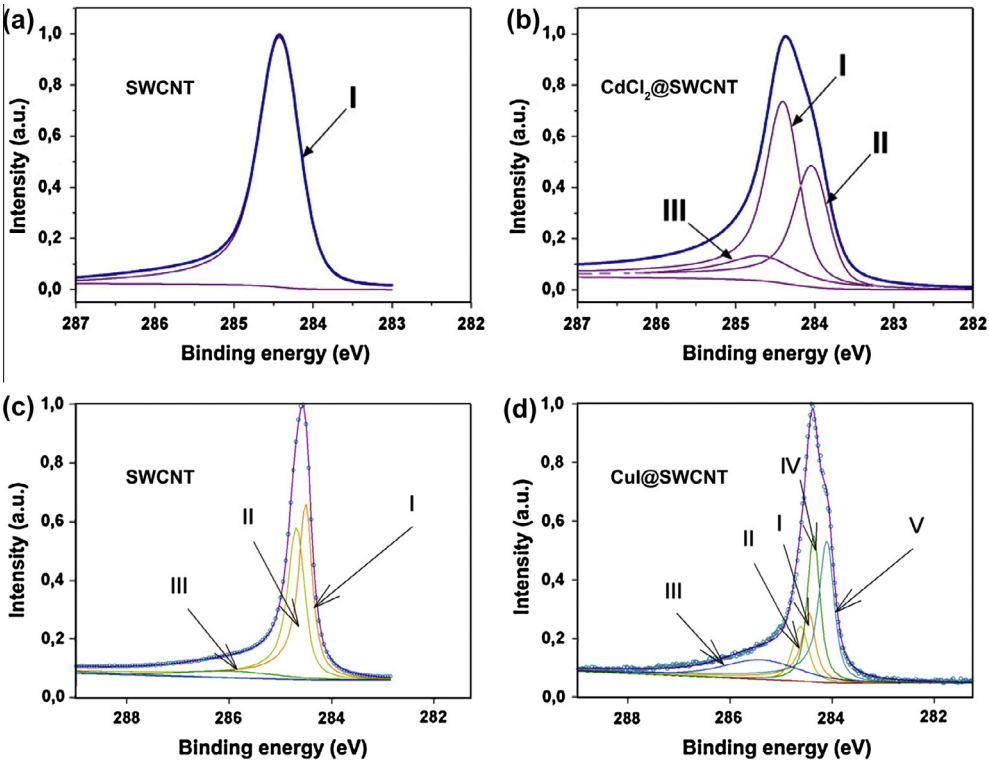


**Fig. 25.** The C 1*s* X-ray photoelectron spectra of (a) the pristine SWCNTs and (b) $CdCl_2$@SWCNT sample separated into the components of the mixture of metallic and semiconducting nanotubes. The component I corresponds to the unfilled SWCNTs, II – the filled SWCNTs, III – local interactions between the SWCNTs and encapsulated salt. Reprinted from Kharlamova MV et al. J Mater Sci 2013;48:8412. Copyright 2013 Springer Science + Business Media New York, with kind permission from Springer Science and Business Media [316]. The C 1*s* X-ray photoelectron spectra of (c) the pristine SWCNTs and (d) CuI@SWCNT nanocomposite separated into the individual components for metallic and semiconducting nanotubes. The components I and II correspond to the unfilled metallic and semiconducting nanotubes, respectively, the components IV and V – the filled semiconducting and metallic SWCNTs, accordingly. The component III corresponds to local interactions between the SWCNTs and the encapsulated salt. Reprinted from Eliseev AA et al. Carbon 2012;50:4021. Copyright 2012, with permission from Elsevier [307].

the conclusions about the direction of charge transfer in later reports [306,307,310–317,328] were no longer exclusively drawn from Raman spectroscopy (Table 2).

The charge transfer from the nanotube walls to the incorporated substances and shift of the SWCNT Fermi level was determined as a result of analysis of the C 1*s* X-ray photoelectron spectra of nanotubes filled with Gd@$C_{82}$ molecules [49,256], erbium chloride [304], halogenides of silver [306], cadmium [316,317], copper [307], iron [310], nickel [312], manganese [313], zinc [314,317], cobalt bromide [311], terbium chloride [317], thulium chloride [315] and gallium selenide [315,328], and comparison of the spectra of filled nanotubes with the spectrum of pristine SWCNTs, which is a narrow peak with the maximum at 284.65 eV binding energy and the FWHM of 0.4 eV [79] (Table 2).

Authors of reports [49,256,304] observed the shift, broadening and increase in asymmetry of the C 1*s* peak of filled SWCNTs, which were assigned to the charge transfer. In the case of the SWCNTs filled with halogenides of silver [306], copper [307], iron [310], nickel [312], manganese [313], zinc [314,317] and cadmium [316,317], cobalt bromide [311], terbium chloride [317], thulium chloride [315] and gallium selenide [315,328], the C 1*s* spectra were separated into several components. Fig. 25a and b shows the C 1*s* XPS spectra of the pristine and cadmium chloride-filled SWCNTs [316]. The spectrum of the filled nanotubes is separated into three components. The first component

corresponds to the unfilled SWCNTs, the second and third components belong to the filled nanotubes. The arising of the second component shifted to lower binding energies as compared to the first component is caused by a change in the work function of nanotubes as a result of filling their channels [316]. The increase of the work function is connected with lowering the SWCNT Fermi level, and it leads to the shift of the components of filled nanotubes toward lower binding energies. The origin of the third component was attributed to local interactions between carbon atoms of the SWCNTs and encapsulated substances [316].

In the case of copper halogenide-filled SWCNTs, the same conception was used for fitting the C 1*s* XPS spectra [307]. But measuring the spectra with high resolution allowed to single out the components corresponding to semiconducting and metallic SWCNTs. It was previously shown in Ref. [79] that the C 1*s* peak of mixed nanotubes can be separated into individual components of metallic and semiconducting nanotubes with maxima at 284.60 and 284.70 eV, and the FWHMs of 0.31 and 0.39 eV, respectively. The shift of the component of metallic SWCNTs by 0.1 eV toward lower binding energies as compared to the semiconducting component was explained by the different work functions in nanotubes of different conductivity type. Later on, the C 1*s* XPS spectra of purely metallic or semiconducting SWCNTs were reported in Ref. [372]. Their maxima and FWHMs were at 284.43 and 284.48 eV binding energies, and 0.26 and 0.32 eV, respectively. The C 1*s* peak of metallic SWCNTs had an asymmetry parameter of $\alpha = 0.11$ [372]. Taking into consideration these differences of the C 1*s* XPS spectra of nanotubes with different conductivity type, the spectra of copper halogenide-filled SWCNTs reported in Ref. [307] were separated into five components. The first and second components were assigned to the unfilled metallic and semiconducting nanotubes, respectively. The forth and fifth components belonged to the filled semiconducting and metallic SWCNTs, accordingly. The third component corresponded to local interactions between the SWCNT walls and the encapsulated salts. Fig. 25c and d shows the C 1*s* XPS spectra of the pristine nanotubes and copper halogenide-filled SWCNTs fitted with the metallic and semiconducting components [307]. The components of the filled nanotubes are shifted toward lower binding energies as compared to the components of the unfilled SWCNTs. This is analogous to the case of cadmium chloride considered above (Fig. 25b), and thus it testifies to lowering the Fermi level of both metallic and semiconducting nanotubes as a result of acceptor doping by the encapsulated copper halogenides.

The Fermi level shift of filled nanotubes can be determined from the data of Raman spectroscopy under electrochemical charging.

Electrochemical charging allows the direct modification of the electronic structure of nanotubes and accurate control of their doping level [373]. It leads to a change in the SWCNT Fermi level, which is proportional to the applied potential [373]. It was shown in Ref. [374] that the coefficient of proportionality is 0.4–0.7 eV/V. The combination of electrochemical charging with *in situ* Raman spectroscopy allows the detailed investigation of the modifications of the spectra of SWCNTs that correspond to a defined shift of their Fermi level [375].

The first measurement of Raman spectra of SWCNTs under electrochemical charging was carried out in 1999 [217]. As a matter of fact, the process of electrochemical charging was concomitted by the intercalation of sulfuric acid inside the SWCNT bundles, which was used as the electrolyte [373]. In 2000, the measurements were performed in common electrolytes, such as water [376] or tetrahydrofuran [231]. Later, a number of reports were published, which were dedicated to the investigation of the SWCNT properties under electrochemical charging in water [374,377–390], acetonitrile [391–395] and ionic liquids [396]. The SWCNTs were used as thin films deposited on inert metals (Au, Hg, Pt) [376,378,379,384–386,392–394,396] or as buckypaper [377,382,387–389,397]. In all cases, *in situ* experiments were performed using three-electrode electrochemical cells where the SWCNTs acted as the main electrode.

Employing Raman spectroscopy under electrochemical charging for the investigation of the electronic properties of the nanotubes filled with silver iodide [306] and copper halogenides [307] allowed the precise determination of the Fermi level shift. In the case of AgI the value equaled −0.6 eV [306], and in the case of copper iodide the Fermi level was shifted by −0.3 eV, whereas for copper chloride the shift reached −0.75 eV [307].

Fig. 26 demonstrates the Raman spectroscopy maps (two-dimensional dependence of the intensity of the G-band components versus Raman shift and applied potential) of the pristine nanotubes and

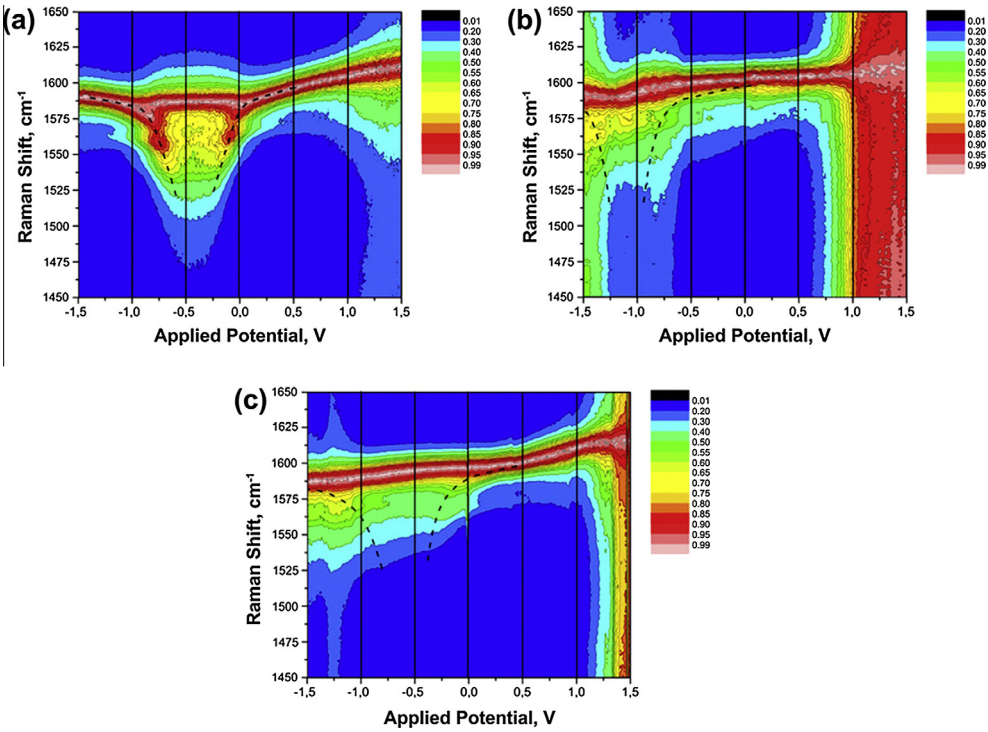


**Fig. 26.** Raman spectroscopy maps (two-dimensional dependence of the intensity of the G-band components versus Raman shift and applied potential) obtained under the electrochemical charging of the pristine SWCNTs (a), CuCl@SWCNT (b) and CuI@SWCNT (c) samples at the applied potentials in the range from −1.5 to 1.5 V. The maps include the joined positive and negative bias branches. The Raman spectra were normalized to the maximal intensity at frequencies in the range of 1450–1650 $cm^{-1}$ in order to achieve a better representation. The dashed lines follow the phonon branches. The maps illustrate a downshift of the Kohn anomaly for the copper halogenide-filled SWCNTs. Reprinted from Eliseev AA et al. Carbon 2012;50:4021. Copyright 2012, with permission from Elsevier [307].

SWCNTs filled with copper chloride and copper iodide [307]. The dependence of the position of the G-band peaks of the pristine SWCNTs on the applied potential includes two branches as shown in Fig. 26a. The first branch shifts toward higher frequencies at potentials above −0.35 V. The second branch is independent of the applied potential, which is typical for armchair nanotubes [398]. Thus, in the case of the pristine nanotubes the Kohn anomaly is located at −0.35 V. It was suggested in Ref. [307] that its shift to negative potentials was caused by the interaction of SWCNTs with electrolyte molecules. The Raman spectroscopy maps of the SWCNTs filled with copper chloride (Fig. 26b) and copper iodide (Fig. 26c) illustrate some broadening of the Raman spectra with the applied potential. However, the position of the Kohn anomaly can be still determined and it equals −1.1 V for CuCl and −0.65 V for CuI, respectively. The shift of the Kohn anomaly as compared to its position in the pristine nanotubes by −0.75 V for CuCl and −0.30 V for CuI was attributed to the corresponding downshift of the SWCNT Fermi level [307].

The shift of the SWCNT Fermi level can be directly determined *via* measuring the secondary electrons cutoff and valence band photoemission spectra of filled nanotubes.

The secondary electrons are the electrons that received their energy from collisions with photoelectrons; their cutoff corresponds to the work function of the sample. Fig. 27a shows the secondary electron cutoff spectra of the pristine nanotubes and the SWCNTs filled with zinc bromide [314]. The spectra are sharp peaks, whose maxima are placed at kinetic energies in the range of 4.5–5.0 eV. From these spectra, the work function was calculated as the value of kinetic energy at the half-maximum of

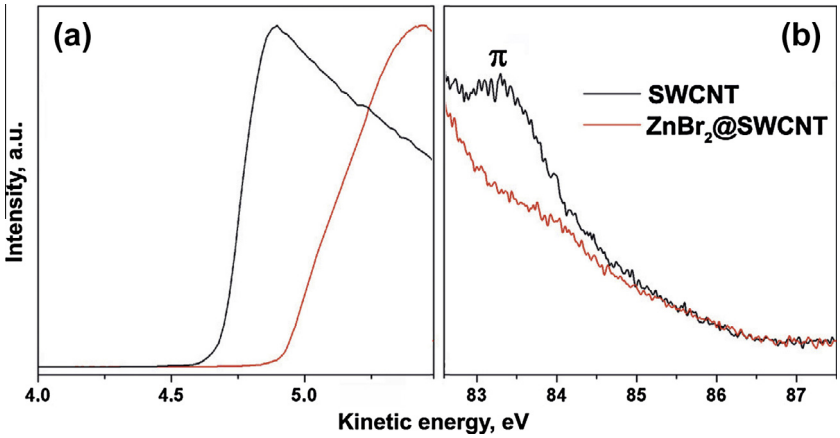


**Fig. 27.** The secondary electrons cutoff (a) and valence band (b) spectra of the pristine SWCNTs and $ZnBr_2$@SWCNT sample, recorded at an excitation energy of 86.7 eV. The secondary electrons cutoff spectra (a) were used for the calculation of the work function of nanotubes as the value of kinetic energy at the half-maximum of the peak. The π-resonance is labeled in the valence band spectra. Reprinted from Kharlamova MV et al. Eur Phys J B 2012;85:34. Copyright 2012 EDP Sciences, Società Italiana di Fisica, Springer-Verlag, with kind permission from Springer Science and Business Media [314].

the peak. According to the obtained data, the work function of the pristine nanotubes was 4.8 eV, and the value of the zinc bromide-filled SWCNTs was 5.1 eV [314]. In Ref. [307], the work function of the pristine and copper iodide, copper bromide and copper chloride-filled SWCNTs was measured by the same method, and the values were 4.6, 4.8, 5.2 and 5.25 eV, respectively. Because the variation of the work function is directly connected with the change in the SWCNT Fermi level, its shift as a result of acceptor doping was determined. The Fermi level shift of nanotubes filled with $ZnBr_2$, CuI, CuBr and CuCl amounted to −0.3, −0.2, −0.6 and −0.65 eV, accordingly [307,314].

The results of the valence band spectra measurements of the filled nanotubes were in agreement with the work function measurements. The valence band spectrum of the pristine nanotubes has the shape, which is characteristic of all $sp^2$ carbon, and includes two main peaks: the π- and σ-resonances. The π-resonance corresponds to photoelectron emission from the nanotube π-band. The σ-resonance belongs to photoelectron emission from the σ-band of SWCNTs [372]. Fig. 27b demonstrates the part of the valence band spectra containing the π-resonance of the pristine SWCNTs and nanotubes filled with zinc bromide [314]. The spectrum of the zinc bromide-filled nanotubes demonstrates a shift of the π-resonance toward higher kinetic energies by 0.3 eV. This tendency was explained by the downshift of the SWCNT Fermi level as result of the charge transfer from the nanotube walls to the incorporated zinc bromide [314]. Acceptor doping effect on the SWCNTs was also proven by the valence band spectra measurements for endohedral fullerene Gd@$C_{82}$ [49,256], erbium chloride [304], copper halogenides [307] and fullerene $C_{60}$ [240].

It was found that filling the SWCNT channels with electron acceptors may lead not only to the charge transfer from the nanotube walls to the encapsulated substances, but also to the formation of chemical bonds between them. X-ray absorption spectroscopy of the SWCNTs filled with copper halogenides showed that chemical bonds are formed in the filled nanotubes [307]. Fig. 28 demonstrates the C 1*s* and Cu 2*p* XAS spectra of the pristine and copper halogenide-filled nanotubes. The C 1*s* spectrum of the pristine nanotubes includes two main features: the resonance *A* located at a photon energy of 285.5 eV and the band *B*–*C* positioned at photon energies ranging from 291 to 293 eV (Fig. 28a). The resonance *A* corresponds to transitions of the C 1*s* electrons to the unoccupied $\pi^*$-band of SWCNTs. The band *B*–*C* accompanied by the less intensive features *D*–*F* belongs to electronic transitions to the nanotube $\sigma^*$-band [79]. The C 1*s* XAS spectrum of the filled nanotubes (Fig. 28a) is similar to the spectrum of the pristine SWCNTs in the range of the absorption features *B*–*F*. However, an additional peak $A^*$ appears at the low-energy side of the $\pi^*$-resonance *A*. It is located at a photon energy of ~284.0 eV. The emergence of this peak testifies to the formation of new localized states

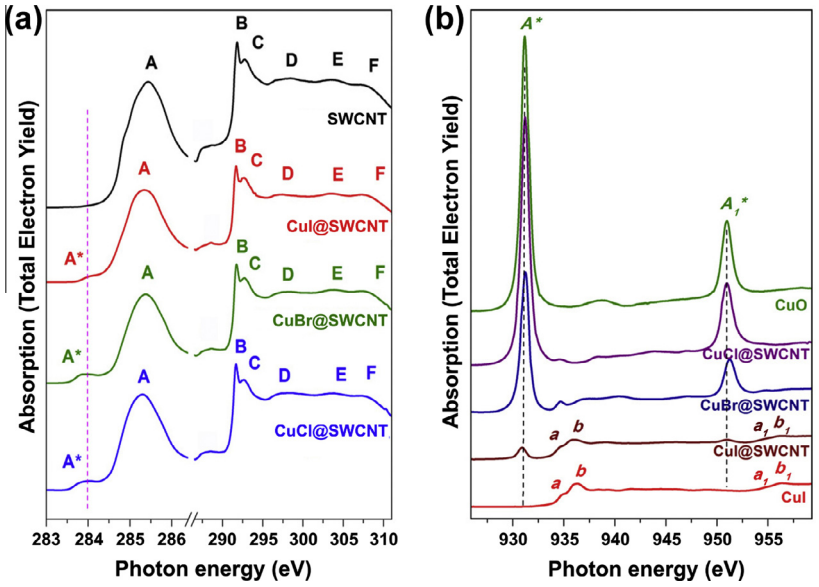


**Fig. 28.** (a) The C 1*s* X-ray absorption spectra of the pristine SWCNTs, CuCl@SWCNT, CuBr@SWCNT and CuI@SWCNT (the left part before the break in the photon energy scale is stretched). The peak *A* is the $\pi^*$-resonance that is assigned to transitions of the C 1*s* electrons to the unoccupied $\pi^*$-band of SWCNTs. The band *B*–*F* belongs to electronic transitions to the nanotube $\sigma^*$-band. The position of the new peak $A^*$ is denoted by the dashed vertical line. (b) The Cu 2*p* X-ray absorption spectra of CuCl@SWCNT, CuBr@SWCNT, CuI@SWCNT and reference samples CuI and CuO. The peaks $A^*$ and $A_1^*$ correspond to electronic transitions from the Cu2$p_{3/2}$ and Cu2$p_{1/2}$ core levels, respectively, to the same empty Cu 3*d* electronic states. Their positions are marked by the dashed vertical lines. The bands *a*–*b* and $a_1$–$b_1$ are assigned to the Cu2*p* → 4*s* electronic transitions. Reprinted from Eliseev AA et al. Carbon 2012;50:4021. Copyright 2012, with permission from Elsevier [307].

in the SWCNT band structure, which are caused by the hybridization of the carbon $\pi$-orbitals with the incorporated copper halogenides [307]. It should be noted that this new peak has a resemblance to the case of iron trichloride-intercalated SWCNT bundles, which was discussed earlier in Section 4.3.

Fig. 28b shows the Cu 2*p* XAS spectra of the copper halogenide-filled SWCNTs and the reference samples – CuO and CuI. The Cu 2*p* spectra of the copper halogenide-filled nanotubes demonstrate two main peaks located at photon energies of ~931 eV (labeled $A^*$) and ~951 eV (labeled $A_1^*$). They correspond to electronic transitions from the Cu2$p_{3/2}$ and Cu2$p_{1/2}$ core levels, respectively, to the same empty Cu 3*d* electronic states [307]. These peaks are not observed in the spectrum of CuI (Fig. 28b). They arise due to electronic transitions to empty Cu 3*d* electronic states, which are not present in CuI and appear in the filled SWCNTs as a result of a chemical interaction between the encapsulated substances and nanotubes. This causes a change in the valence electron configuration of the $Cu^+$ ion from $3d^{10}4s^0$ for CuI to $3d^{10-x}$ for the copper halide-filled SWCNT [307]. The spectrum of CuO, where the $Cu^{2+}$ ion has the valence electron configuration of $3d^9$ and the 3*d* shell is partially unfilled, also demonstrates the similar peaks $A^*$ and $A_1^*$ (Fig. 28b). Besides the appearance of the peaks $A^*$ and $A_1^*$, the Cu 2*p* spectra of the filled SWCNTs show a suppression of the bands *a*–*b* and $a_1$–$b_1$ that are observed for CuI and are assigned to the Cu2*p* → 4*s* electronic transitions. This is caused by a distortion of the structural groups – ionic tetrahedrons $CuI_4$ in the encapsulated salt [307].

The appearance of the additional peaks in the C 1*s* and Cu 2*p* XAS spectra of the copper halogenide-filled SWCNTs was explained by authors of Ref. [307] by the hybridization of the $\pi$-orbitals of SWCNTs and the Cu 3*d* orbitals of the incorporated salts. In this case, electronic transitions occur from the C 1*s* and Cu 2*p* levels to the same empty state of the CuX@SWCNT nanocomposite with a hybridized Cu3*d*–C2$p_z$ nature. It was shown that the energy positions of the new localized states are independent on the type of halogen atom. At the same time, the spectral weight of these localized states increases from copper iodide to copper bromide to copper chloride [307].

The C 1*s* XAS spectra of the SWCNTs filled with other electron acceptors were also reported. The list includes $C_{60}$ [357], Gd@$C_{82}$ [49,256], AgCl, AgBr, AgI [306], $FeCl_2$, $FeBr_2$, $FeI_2$ [310], $NiCl_2$, $NiBr_2$ [312], $ZnCl_2$, $ZnBr_2$, $ZnI_2$ [314], $CdCl_2$, $CdBr_2$, $CdI_2$ [316], $ErCl_3$ [304] and GaSe [328] (Table 2). In the case of the nanotubes filled with halogenides of silver [306], iron [310], nickel [312], zinc [314] and cadmium [316], a new peak located at lower energies as compared to the $\pi^*$-resonance emerged in the C 1*s* XAS spectra, as it was discussed above for the copper halogenide-filled SWCNTs. In these studies, it was also concluded that new localized states in the band structure of filled SWCNTs were formed due to the hybridization of carbon $\pi$-orbitals with the incorporated substances.

*6.1.2.2. Theoretical methods.* Employing theoretical methods for the investigation of the electronic properties of the SWCNTs filled with electron acceptors allowed performing the modeling of the band structure and density of states of filled nanotubes of different chiralities. Furthermore, it also allowed studying the dependence of the SWCNT electronic properties on their diameter and the structure of the encapsulated substances.

By quantum-chemical modeling, the electronic properties of armchair and zigzag nanotubes filled with fullerenes $C_{60}$ [358–363], $C_{70}$, $C_{78}$, $C_{82}$ [360–362] and endohedral fullerenes La@$C_{82}$, K@$C_{60}$, Ca@$C_{60}$, Y@$C_{60}$ [358,360] were simulated (Table 2). It was demonstrated that the modification of the electronic properties of the filled SWCNTs depended on the nanotube diameter. The encapsulation of fullerene $C_{60}$ inside the SWCNTs with a diameter larger than 1.18 nm resulted in a small charge transfer from the nanotubes to the incorporated molecules [363]. Also, it was found in Ref. [358] that the charge transfer from the SWCNTs to the encapsulated molecules was larger for endohedral fullerenes K@$C_{60}$, Ca@$C_{60}$, Y@$C_{60}$ than for fullerene $C_{60}$ molecules.

It was shown in Ref. [356] that the filling of the SWCNTs with electrophylic organic molecules (TCNQ and $F_4$TCNQ) led to acceptor doping of nanotubes. These calculations were in agreement with earlier reported experimental results [48]. Fig. 29 demonstrates the structural models and

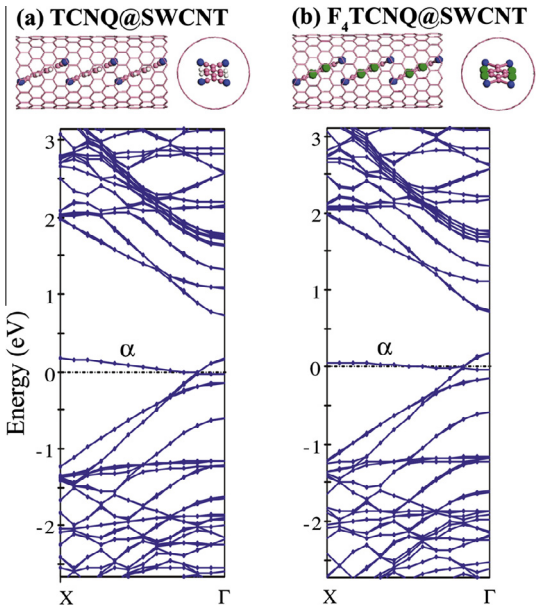


**Fig. 29.** Structural models and electronic band structures of (16,0) SWCNTs filled with TCNQ (a) and $F_4$TCNQ (b) molecules. In the optimized geometries the molecules are centrally located in the SWCNT channels. The oblique angles of the molecular planes relative to the SWCNT axis are 27–28°. Pink ball: C, white ball: H, blue ball: N, green ball: F. The band structures are represented along the X–Γ direction. The Fermi level of SWCNTs is denoted by the dotted line. The flat bands labeled α near the Fermi level are related to the lowest unoccupied molecular orbital states of the molecules. Reprinted figure with permission from Lu J et al. Phys Rev Lett 2004;93:116804. Copyright 2004 by the American Physical Society [356].

corresponding band structures of (16,0) nanotubes filled with TCNQ and $F_4$TCNQ molecules. The optimized geometries of the filled SWCNTs show that the nanotube wall is unchanged upon the encapsulation of the molecules, which are centrally located in the SWCNT channels. The optimized oblique angles of the molecular planes relative to the SWCNT axis are 27–28° [356]. In the band structures of the TCNQ@SWCNT (Fig. 29a) and $F_4$TCNQ@SWCNT (Fig. 29b) samples, the flat bands labeled α near the Fermi level of SWCNTs (marked by the dotted line) are related to the lowest unoccupied molecular orbital states of the molecules [356]. These α bands are partially occupied in the molecule-filled SWCNTs. This testifies to the charge transfer from the nanotube walls to the encapsulated molecules, i.e., acceptor doping of the SWCNTs [356]. The comparison of two band structures shows that the lower-lying α band is more populated in the $F_4$TCNQ@SWCNT sample (Fig. 29b). The conducted Mulliken population analysis confirmed that the charge transfer from the SWCNT walls to the encapsulated $F_4$TCNQ molecules is larger than to TCNQ molecules. The number of transferred electrons per molecule was 0.32 for TCNQ and 0.60 for $F_4$TCNQ. This was explained by larger adiabatic electron affinity of $F_4$TCNQ (3.38 eV) as compared to TCNQ (2.80 eV) [356].

The authors of Ref. [356] concluded that under ambient conditions the escaping process of TCNQ and $F_4$TCNQ molecules appears unlikely once they are encapsulated inside the SWCNTs. Also, the incorporation of these molecules inside nanotubes causes their air stability, because the outer nanotube walls preserve the molecules from oxidation.

There are also reports dedicated to the modeling of the electronic properties of nanotubes filled with chemical compounds. In Ref. [365], the band structure of (8,0) nanotubes filled with chromium oxide $CrO_3$ was calculated. It was found that the encapsulation of chromium oxide inside the nanotube cavities led to acceptor doping of the SWCNTs. These calculations agreed with the experimental observations reported in Ref. [46]. Also, it was demonstrated in Ref. [364] that the incorporation of potassium iodide into the SWCNT interior space caused a very small charge transfer from the nanotube walls to the nanocrystals.

### 6.2. Donor doping

#### 6.2.1. Typical donors of electrons and methods of their encapsulation

According to the data presented in reports on the experimental and theoretical investigations of the electronic properties of filled SWCNTs, the following substances have an electron donor effect on the nanotubes: molecules – organic molecules (tetrakis(dimethylamino)ethylene (TDAE) and tetrathiafulvalene (TTF) [48,356]) and organometallic molecules ($Co(C_5H_5)_2$, $Co(C_5H_4C_2H_5)_2$ [47,399,400], $Fe(C_5H_5)_2$ [50,260,262,263,265,267,399,400], $Ce(C_5H_5)_3$ [51,269], $M(C_5H_5)_2$, M = V, Cr, Mn, Ni [399]) and simple substances – metals (Ag [46,293,294,296,315,365,401], Cu [293,295], Eu [272,402], Li, K [403], Ti, Zn, Co, Ni, Fe, Mo, Gd, Cu [402,404–410]).

The incorporation of donors of electrons into the SWCNT channels was carried out using different methods. The filling of the nanotubes with organic molecules (TDAE, TTF [48,356]) and organometallic molecules ($Co(C_5H_5)_2$, $Co(C_5H_4C_2H_5)_2$ [47], $Fe(C_5H_5)_2$ [50,260,262,263,265,267], $Ce(C_5H_5)_3$ [51,269]) was performed *via* the gas phase method (see Section 5.2.2), which resulted in clean samples suitable for further spectroscopic investigations. It should be noted that it was also reported that the incorporation of ferrocene $Fe(C_5H_5)_2$ into the nanotubes can be performed by the liquid phase method using its solution in an organic solvent [284].

The encapsulation of metals (Ag [46,293,294,296,315] and Cu [293,295]) inside the SWCNTs was carried out *via* the liquid phase method (from metal nitrate solutions) with subsequent thermal treatment (see Section 5.2.5). This approach allowed obtaining clean samples (without metallic particles on the SWCNT outer surface) owing to the multistep sample washing procedure. It is worth noticing that it was reported that metallic silver inside the SWCNTs can also be obtained by the photolytic decomposition of the encapsulated silver chloride [21]. To introduce the europium into the SWCNT channels, the gas phase approach was used [272].

Fig. 30 shows the HRTEM micrographs of the SWCNTs filled with electron donors. Two individual nanotubes filled with $Co(C_5H_4C_2H_5)_2$ molecules are presented in Fig. 30a [47]. The encapsulated molecules are clearly seen inside the SWCNT channels, as indicated by the arrows. The micrograph in Fig. 30b demonstrates an individual ferrocene-filled nanotube [265]. Dark contrasts are observed

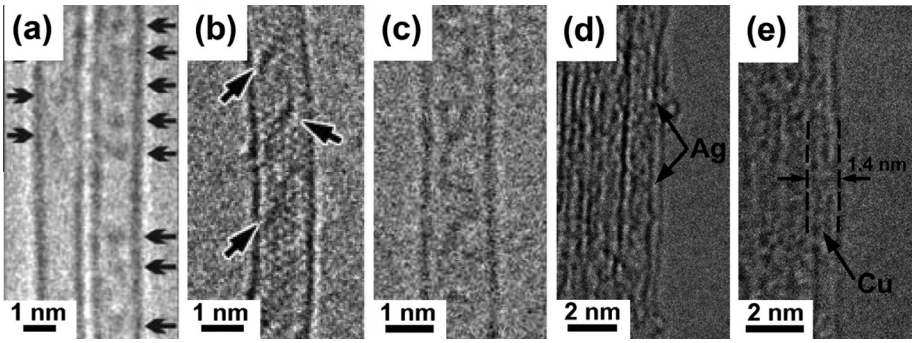


**Fig. 30.** The HRTEM images of SWCNTs filled with electron donors: bis(ethylcyclopentadienyl) cobalt $Co(C_5H_4C_2H_5)_2$ (a) (adapted by permission from Macmillan Publishers Ltd: Nat Mater, Li LJ et al. Nat Mater 2005;4:481, Copyright 2005 [47]), ferrocene $Fe(C_5H_5)_2$ (b) (reprinted with permission from Shiozawa H et al. Adv Mater 2008;20:1443. Copyright 2008 Wiley-VCH Verlag GmbH & Co. KGaA, Weinheim [265]), cerocene $Ce(C_5H_5)_3$ (c) (reprinted figure with permission from Shiozawa H et al. Phys Rev Lett 2009;102:046804. Copyright 2009 by the American Physical Society [51]), elemental silver (d) (the data are from Ref. [293]) and copper (e) (the data are from Ref. [295]). The arrows indicate the encapsulated substances. In (e) the nanotube walls are also marked by the dashed vertical lines, and the SWCNT diameter is shown by the horizontal arrows.

inside the SWCNT channel, as highlighted by the arrows. They are not observed outside the SWCNTs. This proves the successful encapsulation of $Fe(C_5H_5)_2$ molecules into the nanotubes. Fig. 30c demonstrates the HRTEM image of an individual cerocene-filled SWCNT [51]. Arrays of contrasts are easily discerned within the nanotube walls. They correspond to the incorporated $Ce(C_5H_5)_3$ molecules. Fig. 30d presents the micrograph of silver-filled SWCNTs [293]. It is seen that the SWCNT channel is filled, as denoted by the arrows. Fig. 30e demonstrates the HRTEM image of copper-filled nanotubes [295]. The nanotube walls are marked by the dashed vertical lines, and the SWCNT diameter is shown by the horizontal arrows. This micrograph confirms the presence of metal atoms within the nanotube walls, as denoted by the arrow.

Table 3 summarizes typical donors of electrons, methods of their encapsulation into the SWCNTs and methods of investigation of the electronic properties of the obtained nanostructures.

### *6.2.2. Characterization of electronic properties of SWCNTs filled with electron donors*

*6.2.2.1. Experimental methods.* The charge transfer and its direction in the nanotubes filled with electron donors were characterized by optical absorption spectroscopy, Raman spectroscopy, X-ray absorption spectroscopy and photoluminescence spectroscopy. The determination of the Fermi level position and its shift as compared to the initial position was carried out using X-ray photoelectron spectroscopy and ultraviolet photoelectron spectroscopy.

Fig. 31a shows the optical absorption spectra of the pristine SWCNTs, the nanotubes with open ends used for the filling, and ferrocene-filled SWCNTs [260]. The spectra have two regions – $E_{11}^S$ and $E_{22}^S$, each of which contains several peaks. The peaks located in the $E_{11}^S$ region correspond to electronic transitions between the first van Hove singularities of semiconducting SWCNTs, and the peaks located in the $E_{22}^S$ region belong to those between the second vHs of semiconducting tubes. Every single peak relates to an electronic transition between the corresponding vHs of semiconducting SWCNT with a specific chirality [260]. The spectrum of the nanotubes with open ends demonstrates a significant decrease in the intensity of peaks placed in the $E_{11}^S$ region at wavelengths in the range from 900 to 1100 nm, as well as the shift of these peaks to longer wavelengths as compared to the spectrum of the pristine SWCNTs. These changes were attributed to acceptor doping of nanotubes by adsorbed oxygen molecules, the formation of carbon–oxygen bonds and the filling of the SWCNT channels with water molecules from the solution, in which the nanotubes were dispersed for measuring the OAS spectra [260]. The case of acceptor doping of SWCNTs is analogous to the one considered above in Section 6.1.2. Acceptor doping of the nanotubes leads to removing the electrons from the valence band of SWCNTs, lowering the SWCNT Fermi level and the corresponding suppression of electronic

**Table 3**
Typical donors of electrons, methods of their encapsulation inside the SWCNT channels and methods of investigation of the electronic properties of the obtained nanostructures.

| Type of substance | | Substance | Method of encapsulation | Methods of investigation of electronic properties[c] | Reference |
|---|---|---|---|---|---|
| Molecule | Organic molecule | TDAE[a], TTF[b] | Gas phase | OAS, RS | [48] |
| | | | – | QM | [356] |
| | Organometallic molecule | $Co(C_5H_5)_2$, $Co(C_5H_4C_2H_5)_2$ | Gas phase | OAS, PLS | [47] |
| | | | – | QM | [399,400] |
| | | $Fe(C_5H_5)_2$ | Gas phase | UPS | [265] |
| | | | | XPS, UPS, XAS, QM | [50] |
| | | | | XPS, UPS, XAS | [262,263] |
| | | | | OAS, PLS, QM | [260] |
| | | | | XPS, XAS | [267] |
| | | | – | QM | [399,400] |
| | | $Ce(C_5H_5)_3$ | Gas phase | XPS, UPS, XAS | [51,269] |
| | | $M(C_5H_5)_2$, M = V, Cr, Mn, Ni | – | QM | [399] |
| Simple substance | Metal | Ag | Liquid phase ($AgNO_3$ solution + annealing) | RS | [46] |
| | | | | OAS, RS, XPS | [293,294,315] |
| | | | | XAS | [296] |
| | | | – | QM | [365,401] |
| | | Cu | Liquid phase ($Cu(NO_3)_2$ solution + annealing) | RS, XPS | [293,295] |
| | | Eu | Gas phase | XPS, UPS, XAS | [272] |
| | | | – | QM | [402] |
| | | Li, K | – | QM | [403] |
| | | Ti, Zn, Co, Ni, Fe, Mo, Gd, Cu | – | QM | [402,404–410] |

[a] TDAE = tetrakis(dimethylamino)ethylene.
[b] TTF = tetrathiafulvalene.
[c] OAS = optical absorption spectroscopy, RS = Raman spectroscopy, QM = quantum-chemical modeling, UPS = ultraviolet photoelectron spectroscopy, XPS = X-ray photoelectron spectroscopy, XAS = X-ray absorption spectroscopy, PLS = photoluminescence spectroscopy.

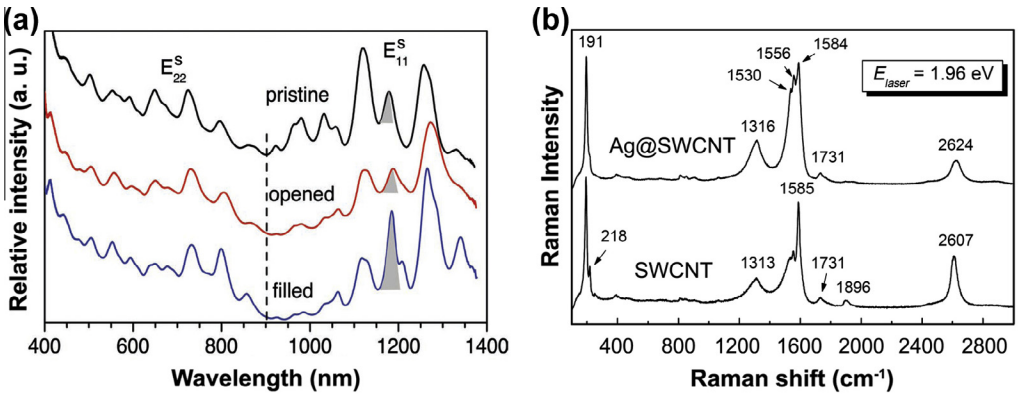


**Fig. 31.** (a) The optical absorption spectra of the pristine, open-ended and ferrocene-filled nanotubes suspended in bile salt water solution. The symbols $E_{11}^S$ and $E_{22}^S$ denote regions that contain peaks corresponding to the first and the second vHs of semiconducting SWCNTs of different chiralities, respectively. All spectra were normalized at the position of the minimum between $E_{11}^S$ and $E_{22}^S$ regions, as marked by the dashed vertical line. The gray area shows the $E_{11}^S$ peak, which exhibits the strongest intensity increase upon filling. Reprinted with permission from Liu XJ et al. Adv Funct Mater 2012;22:3202. Copyright 2012 Wiley-VCH Verlag GmbH & Co. KGaA, Weinheim [260]. (b) The resonance Raman spectra of the pristine and silver-filled SWCNTs obtained at $E_{laser}$ = 1.96 eV. The numbers denote the positions of the peaks. Reprinted from Corio P et al. Chem Phys Lett 2004;383:475. Copyright 2004, with permission from Elsevier [46].

transitions between valence and conduction bands of the open-ended nanotubes [260]. In the spectrum of ferrocene-filled SWCNTs (Fig. 31a), the peaks in the $E_{11}^S$ region maintain the red shift, but their intensity increases significantly as compared to the spectrum of the open-ended nanotubes. This testifies that the charge transfer occurs from the incorporated ferrocene molecules to the SWCNT walls, i.e., donor doping of nanotubes takes place [260].

Fig. 31b demonstrates the Raman spectra of pristine nanotubes and SWCNTs filled with silver, which were acquired at a laser energy of 1.96 eV [46]. The spectrum of the filled nanotubes shows the change in the intensities of the RBM peaks, as well as the shift of the G-band peaks and modification of the G-band profile. This is an evidence of a change in resonance excitation conditions of the filled nanotubes due to charge transfer. Such changes were also observed by other authors for SWCNTs filled with silver [293,294,315], organic molecules [48] and copper [293,295]. As it was noticed in Section 6.1.2, it is impossible to derive conclusive information about the direction of the charge transfer in the filled nanotubes from the Raman spectroscopy data. However, the softening of the G-band accompanied by the relative increase in intensity of the $G^-$-mode as compared to the $G^+$-mode (and change of the G-band profile from semiconducting to metallic type) may testify to donor doping of the nanotubes by the encapsulated substances [46,48,293–295,315].

Besides the charge transfer, the local interactions between carbon and metal atoms were found in the silver-filled SWCNTs. Authors of Ref. [296] observed a new additional peak between the $\pi^*$- and $\sigma^*$-resonances in the C 1*s* core level excitations of the filled nanotubes (Fig. 32a), which was attributed to the hybridization of valence orbitals of carbon and silver along with the charge transfer from the incorporated metallic nanoparticles to the SWCNTs.

The C 1*s* XAS spectra of the nanotubes filled with other electron donors were investigated. Among them are ferrocene [50,262,263,267], cerocene [51,269] and europium [272] (Table 3). Fig. 32b demonstrates the spectrum of the SWCNTs filled with cerocene in comparison with the spectrum of pristine nanotubes [269]. The spectrum of the filled nanotubes contains the $\pi^*$- and $\sigma^*$-resonances, which are characteristic of all $sp^2$ carbon. Performing the measurements with high resolution allowed investigating the fine structure of the $\pi^*$-resonance, where every single peak corresponds to an electronic transition from the C 1*s* core level to an individual van Hove singularity in the SWCNT conduction band [79]. Fig. 32c shows the part of the C 1*s* XAS spectra containing the $\pi^*$-resonance of the nanotubes filled with cerocene in comparison with the data of the pristine SWCNTs [269]. The peaks indicated in the spectra belong to the first, the second and the third vHs of semiconducting

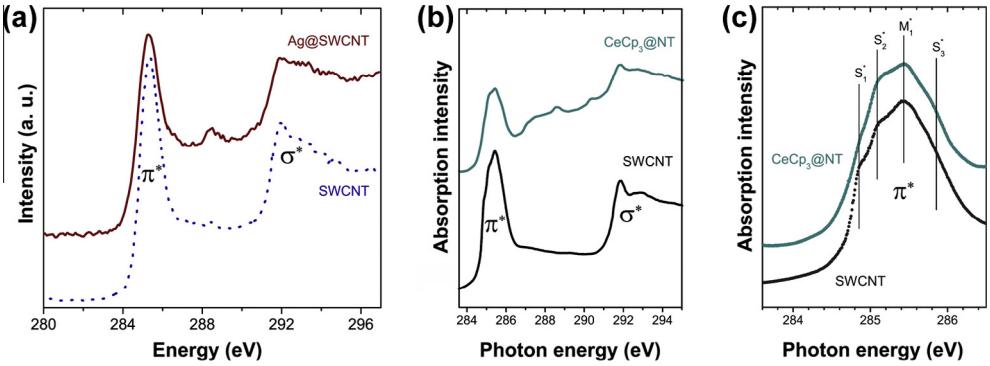


**Fig. 32.** (a) The core level excitations of the pristine (blue dotted line) and silver-filled SWCNTs (dark red solid line). The spectrum of the silver-filled SWCNTs demonstrates a new peak between the $\pi^*$- and $\sigma^*$-resonances. The data are replotted from Ref. [296]. (b) The C 1*s* X-ray absorption spectra of the pristine and cerocene-filled nanotubes, which include the $\pi^*$- and $\sigma^*$-resonances. Reprinted with permission from Shiozawa H et al. Phys Status Solidi B 2009;246:2626. Copyright 2009 Wiley-VCH Verlag GmbH & Co. KGaA, Weinheim [269]. (c) The region of the C 1*s* XAS spectra from (b) containing the $\pi^*$-resonance of the pristine and $CeCp_3$-filled SWCNTs. The positions of the peaks corresponding to the first, the second and the third vHs of semiconducting SWCNTs and the first vHs of metallic nanotubes ($S_1^*$, $S_2^*$, $S_3^*$ and $M_1^*$, respectively) are denoted by vertical lines. Reprinted with permission from Shiozawa H et al. Phys Status Solidi B 2009;246:2626. Copyright 2009 Wiley-VCH Verlag GmbH & Co. KGaA, Weinheim [269].

SWCNTs and the first vHs of metallic nanotubes ($S_1^*$, $S_2^*$, $S_3^*$ and $M_1^*$, respectively). The spectrum of the filled SWCNTs demonstrates the decrease in intensity of the component corresponding to the first van Hove singularity of semiconducting SWCNTs, which is caused by the charge transfer from the encapsulated substance to the nanotube walls. The same changes in the C 1*s* XAS spectra were reported for SWCNTs filled with Eu [272] and ferrocene [50,262,263].

Additional information on the charge transfer in filled nanotubes can be obtained by photoluminescence spectroscopy. Fig. 33 demonstrates the photoluminescence (PL) maps of the pristine nanotubes, the SWCNTs with open ends and the ferrocene-filled SWCNTs [260]. The photoluminescence maps (two-dimensional dependence of photoluminescence intensity on excitation and emission wavelengths) include characteristic maxima, each of which corresponds to SWCNTs of a certain chirality [78,411]. In general, the modification of these maps, such as the change in the photoluminescence intensity for nanotubes of specific chiralities and the shift of the corresponding maxima along the axes of emission and excitation wavelengths may be evidence of changes in the electronic properties of SWCNTs.

The comparison of the photoluminescence maps of the pristine SWCNTs (Fig. 33a) and the open-ended nanotubes (Fig. 33b) testifies to significant changes of spectral features for small diameter SWCNTs [260]. The photoluminescence intensity of tubes with chiralities of (8,3), (6,5) and (7,5) decreases substantially, and the maxima corresponding to (6,4) and (9,1) nanotubes vanish completely in the PL map of the open-ended nanotubes (Fig. 33b). This may be caused by the fact that the SWCNTs with small diameters are easier to be oxidized during the opening of their ends [260]. At the same time, there is an increase in the photoluminescence intensity of nanotubes of large diameters in the PL map of the SWCNTs with opened ends. Besides, this PL map demonstrates the shift of the maxima to longer emission and excitation wavelengths (Fig. 33b). This may be explained by the presence of water molecules inside the opened SWCNTs, which cause a reduction of electron–electron repulsion and exciton binding energies by dielectric screening resulting in the observed red shifts [260]. The shift values are bigger for the nanotubes of larger diameters, because they are more suitable for filling than smaller SWCNTs. It should be noted that among all the nanotubes on the PL map, only the SWCNTs with chiralities of (8,6), (9,5), (8,7), (11,1) and (10,5) have big enough diameter for the incorporation of ferrocene molecules. The molecules cannot be encapsulated into the SWCNTs of smaller diameters [260]. This is proven by the data of filled nanotubes (Fig. 33c). The PL map of the filled SWCNTs demonstrates a significant increase in the photoluminescence intensity of the nanotubes of large enough diameters reaching 170% for (8,6) SWCNTs and 270% for (9,5) SWCNTs

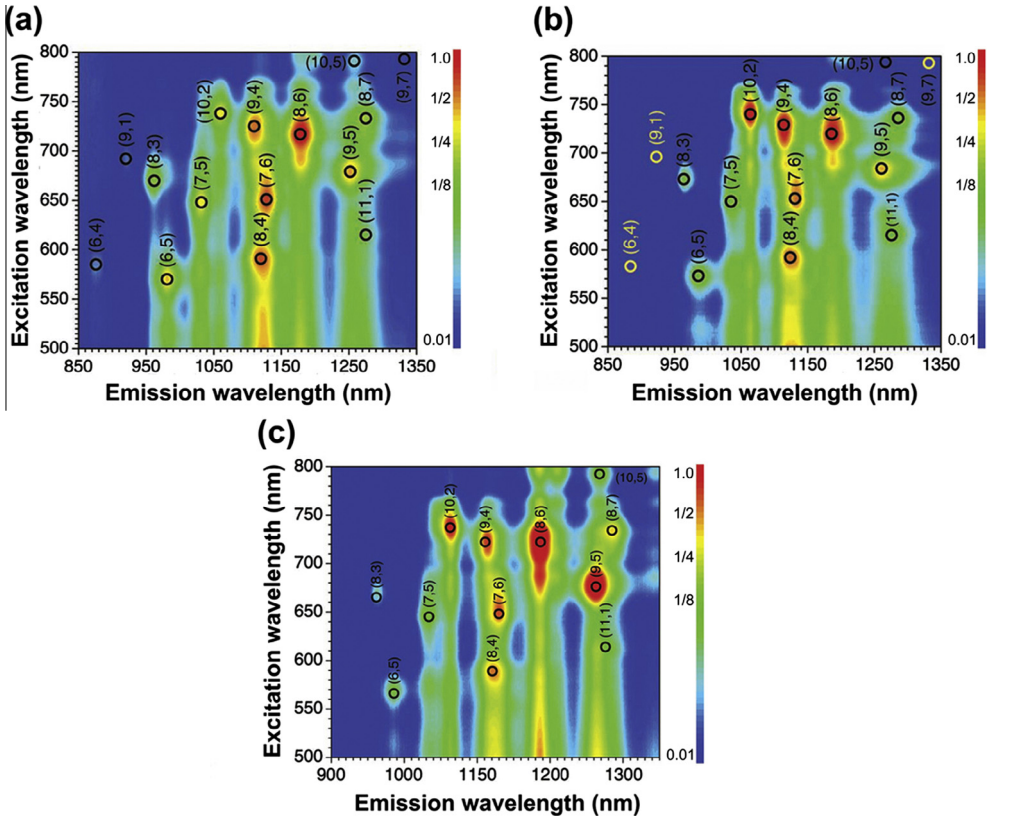


**Fig. 33.** The photoluminescence maps (two-dimensional dependence of photoluminescence intensity on excitation and emission wavelengths) of the pristine (a), opened (b) and ferrocene-filled SWCNTs (c) dispersed in bile salt water solution. The photoluminescence intensity is normalized to the optical density at 900 nm and plotted on a logarithmic scale. The circles denote the maxima, which correspond to the detected SWCNTs of certain chiralities. The chirality assignment is shown by labels. The yellow circles in (b) denote the maxima that disappeared in the opened SWCNTs, but are present in the pristine nanotubes. Reprinted with permission from Liu XJ et al. Adv Funct Mater 2012;22:3202. Copyright 2012 Wiley-VCH Verlag GmbH & Co. KGaA, Weinheim [260].

in comparison with the PL map of the open-ended nanotubes. Besides, the red shift of the maxima along the axis of emission wavelength is observed in the PL map of the ferrocene-filled SWCNTs (Fig. 33c). On the basis of these data, the authors of Ref. [260] drew the conclusion about the charge transfer from ferrocene molecules to the SWCNT walls, i.e., donor doping of nanotubes.

The information on the charge transfer and upshift of the SWCNT Fermi level as a result of their filling with electron donors can be derived from X-ray photoelectron spectroscopy measurements. There are reports on investigations of the C 1*s* XPS spectra of nanotubes filled with ferrocene [50,262,263,267], cerocene [51,269], europium [272], silver [293,294,315] and copper [293,295] (Table 3). In Refs. [50,51,262,263,267,269,272], the changes in position, width and shape of the C 1*s* peak were attributed to the modification of the electronic properties of nanotubes. Fig. 34a shows the C 1*s* XPS spectrum of cerocene-filled SWCNTs in comparison with the spectrum of the pristine nanotubes [269]. The spectrum of the filled SWCNTs demonstrates a slight shift of the maximum toward higher binding energies and an increase in the asymmetry and width of the C 1*s* peak, which is caused by the change in the nanotube work function as result of the charge transfer from the encapsulated molecules to the SWCNTs [269]. It is worth noticing that these changes resemble the ones observed at the intercalation of SWCNT bundles by alkali metals [58,192], which was discussed above in Section 4.3.

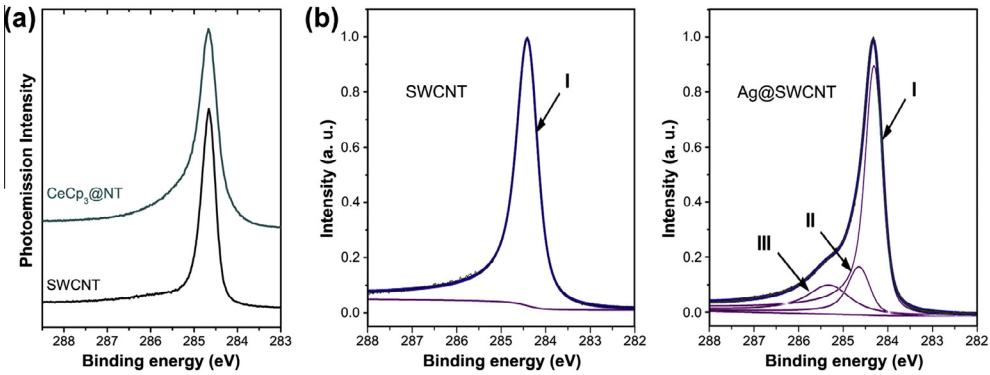


**Fig. 34.** (a) The C 1*s* X-ray photoelectron spectra of the pristine and cerocene-filled SWCNTs. Reprinted with permission from Shiozawa H et al. Phys Status Solidi B 2009;246:2626. Copyright 2009 Wiley-VCH Verlag GmbH & Co. KGaA, Weinheim [269]. (b) The C 1*s* XPS spectra of the pristine and silver-filled SWCNTs separated into the individual components. The component I corresponds to the unfilled SWCNTs. The component II belongs to the filled SWCNTs. The component III is caused by local interactions between the nanotube walls and atoms of the encapsulated metal. The data are replotted from Ref. [293].

For the SWCNTs filled with silver [293,294,315] and copper [293,295], the C 1*s* XPS spectra were separated into several components. Fig. 34b shows the spectrum of the silver-filled nanotubes in comparison with the spectrum of the pristine SWCNTs [293]. The spectrum of the pristine nanotubes can be fitted using one single component, whereas the spectrum of filled SWCNTs is separated into three components. The first component belongs to the unfilled nanotubes, and the second and the third components correspond to the silver-filled SWCNTs [293]. The maximum of the second component is shifted by 0.33 eV toward higher binding energies as compared to the position of the first component. The origin of this new component is analogous to the case discussed in Section 6.1.2 for the SWCNTs filled with metal halogenides. The only difference is that in the case of metal-filled nanotubes this new component appears at higher binding energies than the first component. This is caused by the change in the work function of SWCNTs as a result of increasing their Fermi level due to the charge transfer from the incorporated metallic nanoparticles [293]. The origin of the third component in the spectra was explained by possible local interactions between the nanotube walls and atoms of the encapsulated metal [293].

The determination of the shift value of the Fermi level of SWCNTs filled with electron donors was carried out using ultraviolet photoelectron spectroscopy. The valance band spectra were investigated for SWCNTs filled with ferrocene [50,262,263,265], cerocene [51,269] and europium [272] (Table 3). The high resolution measurements revealed three peaks near the Fermi level, which correspond to the individual van Hove singularities of SWCNTs [80,202]. Fig. 35 demonstrates the valence band spectra of the nanotubes filled with ferrocene molecules (Fig. 35a) [265] and europium atomic wires (AWs) (Fig. 35b) [272] in comparison with the spectra of the pristine SWCNTs. The peaks marked in the spectra belong to the first and the second vHs of semiconducting SWCNTs and to the first vHs of metallic nanotubes ($S_1$, $S_2$ and $M_1$, respectively). In the spectra of the filled SWCNTs, there is the shift of peaks of vHs to higher binding energies by 0.05 eV for ferrocene (Fig. 35a) and 0.1 eV for europium (Fig. 35b), which corresponds to increasing the Fermi level by these values. Besides, the increase of density of states on the Fermi level is clearly visible in the spectrum of europium-filled SWCNTs (Fig. 35b). The changes in the spectra of the filled nanotubes indicate the charge transfer from the incorporated substances to the SWCNT walls, i.e., donor doping of nanotubes [265,272]. It should be noted that these changes are similar to those observed at the intercalation of nanotube bundles by alkali metals [58,192,202,412], which was considered above in Section 4.3.

*6.2.2.2. Theoretical methods.* As a complementary approach to the experimental methods, the electronic structure of the SWCNTs filled with electron donors was investigated *via* quantum-chemical

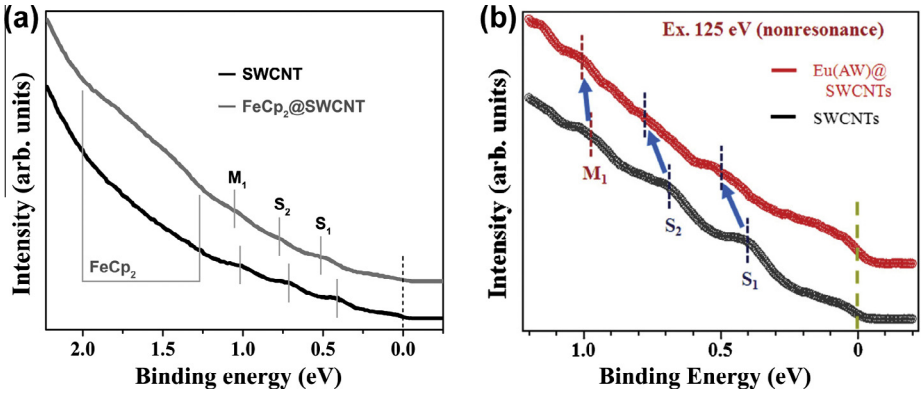


**Fig. 35.** (a) The ultraviolet photoelectron spectra of the pristine and ferrocene-filled SWCNTs. The solid vertical lines denote the positions of the peaks corresponding to the first and the second vHs of semiconducting SWCNTs and the first vHs of metallic nanotubes ($S_1$, $S_2$ and $M_1$, respectively). The spectrum of the filled SWCNTs demonstrates an additional trapezoidal structure at binding energies ranging from 1.7 to 2 eV, as shown on the plot, which stems from the highest occupied molecular orbital of ferrocene. The dashed vertical line marks the Fermi level. The data are replotted from Ref. [265]. (b) The UPS spectra of the pristine and europium-filled SWCNTs. The positions of the peaks of vHs of semiconducting and metallic nanotubes ($S_1$, $S_2$ and $M_1$) are denoted by the blue and red dashed vertical lines. The arrows show the shift of the peak positions for the filled SWCNTs. The dark yellow dashed vertical line marks the Fermi level. Reprinted figure with permission from Nakanishi R et al. Phys Rev B 2012;86:115445. Copyright 2012 by the American Physical Society [272].

modeling. Reports are dedicated to the modeling of the band structure and the DOS of filled nanotubes with specific chiralities, as well as the revealing of the correlation between the structure of the encapsulated metallic nanowires and their influence on the SWCNT electronic properties.

The authors of Ref. [356] found that the encapsulation of nucleophilic organic (TTF and TDAE) and organometallic (cobaltocene) molecules into the SWCNT channels led to donor doping of nanotubes. The donor doping effect on the SWCNTs of other metallocenes was demonstrated in Refs. [50,399,400] for compounds $M(C_5H_5)_2$, where M = V, Cr, Mn, Fe, Co, Ni.

The calculation of the band structures of metal-filled nanotubes $[Li@C_{24}]_n$ and $[K@C_{36}]_n$ was performed in Ref. [403]. The charge transfer from the nanotube walls to the incorporated metallic atoms was proven for these nanostructures. Similarly, the calculation of the band structure of silver-filled (8,0) nanotubes carried out in Ref. [365] showed that the incorporation of silver inside the SWCNT channels led to donor doping of the (8,0) nanotubes. This was in agreement with the experimental findings reported in Ref. [46]. Furthermore, there are other reports on the investigation of donor doping of SWCNTs by metals, such as Ti, Zn [405], Co, Ni [410], Fe [405,406,409], Mo [407], Gd [402,408], Eu [402], Cu [404], and Ag [401] (Table 3).

Fig. 36 shows the structural models and band structures of the pristine SWCNTs with a chirality of (8,8) and the nanotubes filled with iron nanowires ($Fe_n$@SWCNT), containing $n$ = 5, 9 and 13 metal atoms in the cross section [406]. As it is seen in the band structure in Fig. 36a, the (8,8) nanotube is metallic, since the $\pi$ and $\pi^*$ bands are touching at the Fermi level. Because of the differences in the work functions ($WF_{bulk\ Fe}$ = 4.5 eV and $WF_{SWCNT}$ = 4.8 eV), the filling of the SWCNTs with iron nanowires leads to the charge transfer from the iron atoms to the SWCNT walls [406]. As a result, the C-related bands are lowered in the band structures of the filled nanotubes, and the effect is more prominent for the nanotubes containing a larger number of iron atoms in their cross section (Fig. 36b–d). If the iron nanowires do not interact with the SWCNT walls, the band structure of the filled SWCNTs can be simply represented by a superposition of the individual band structures. This is the case for the $Fe_5$@SWCNT system (Fig. 36b). If the iron nanowire contains a larger number of atoms placed closer to the SWCNT wall, the hybridization between the $\pi$ orbitals of the carbon atoms and the *d* orbitals of the iron atoms occurs. This strongly perturbs the $\pi$ bands of nanotubes, especially for the $Fe_{13}$@SWCNT sample (Fig. 36c and d).

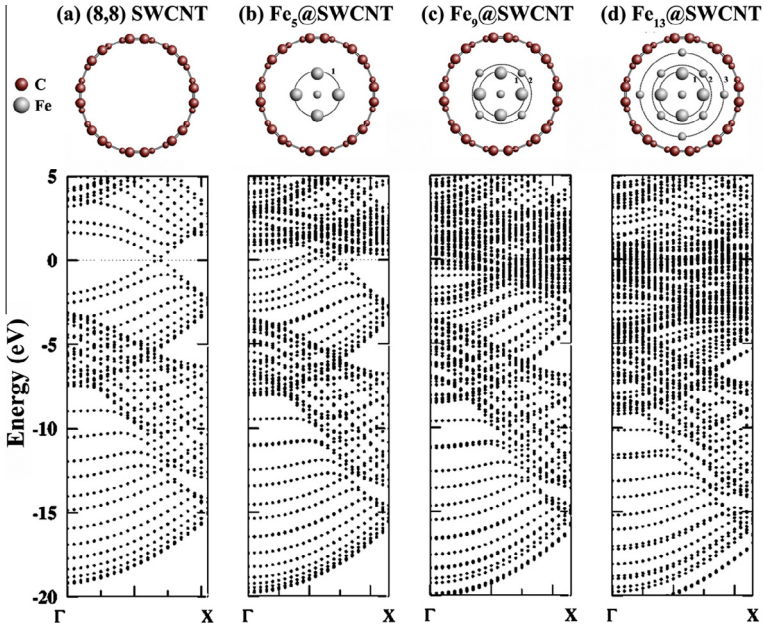


**Fig. 36.** The ball-and-stick cross-section models and calculated band structures of an empty (8,8) nanotube (a) and the (8,8) nanotubes filled with iron nanowires ($Fe_n$@SWCNT), containing $n$ = 5 (b), 9 (c) and 13 (d) metal atoms in the cross section. The structural models of iron nanowires are represented as one central Fe atom encircled by one, two or three shells with four Fe atoms each in the $Fe_5$@SWCNT, $Fe_9$@SWCNT and $Fe_{13}$@SWCNT samples, respectively. The Fe shells of nanowires are marked by dashed circles with corresponding numbers. The band structures are represented along the Γ–X direction. The Fermi level of SWCNTs is positioned at zero. Reprinted figure with permission from Kang YJ et al. Phys Rev B 2005;71:115441. Copyright 2005 by the American Physical Society [406].

### *6.3. No modification of electronic properties*

The encapsulation of some substances does not lead to the modification of the SWCNT electronic properties. In this case, the electronic structure of the incorporated substances is unperturbed, too. This opens the way to use the SWCNTs as templates for synthesizing unique one-dimensional structures, not interacting with the nanotube walls, for instance 1D nanocrystals with only a few atoms in their cross-sections that would not be stable on their own. Moreover, the internal channels of the SWCNTs are protecting the incorporated substances from reactions with the environment.

In Ref. [323], quasi-free-standing one-dimensional SnTe nanocrystals were grown inside the SWCNTs *via* the melt filling method. Fig. 37a–c shows the HRTEM micrographs of the obtained nanostructures. The low-magnification image (Fig. 37a) of the nanotube bundle proves the incorporation of tin telluride into the SWCNTs, because contrast elements are observed inside the nanotube channels. Moreover, the visible periodicity of the contrast elements demonstrates the crystallization of the encapsulated SnTe. The micrograph in Fig. 37b shows the cross-sectional view of the filled nanotube bundle. It also gives an evidence of the incorporation of tin telluride into the SWCNTs. Inside the SWCNT channels, which are seen as dark circles, contrast elements of the encapsulated SnTe that form circle patterns are clearly visible. The micrograph in Fig. 37c, which is a high-magnification image of the nanotube bundle observed in Fig. 37a (as denoted by the black rectangle in Fig. 37a), shows two individual nanotubes with a diameter of 1.35 nm. Three atoms are seen inside the SWCNT channel along the diameter direction. The distance between them is 0.33 nm, and the periodicity along the tube axis is 0.28 nm, as indicated on the micrograph. The measured 1D crystal period is essentially smaller than that in the bulk rocksalt structure (0.316 nm), which implies a significant bond lengths contraction along the SWCNT axis [323].

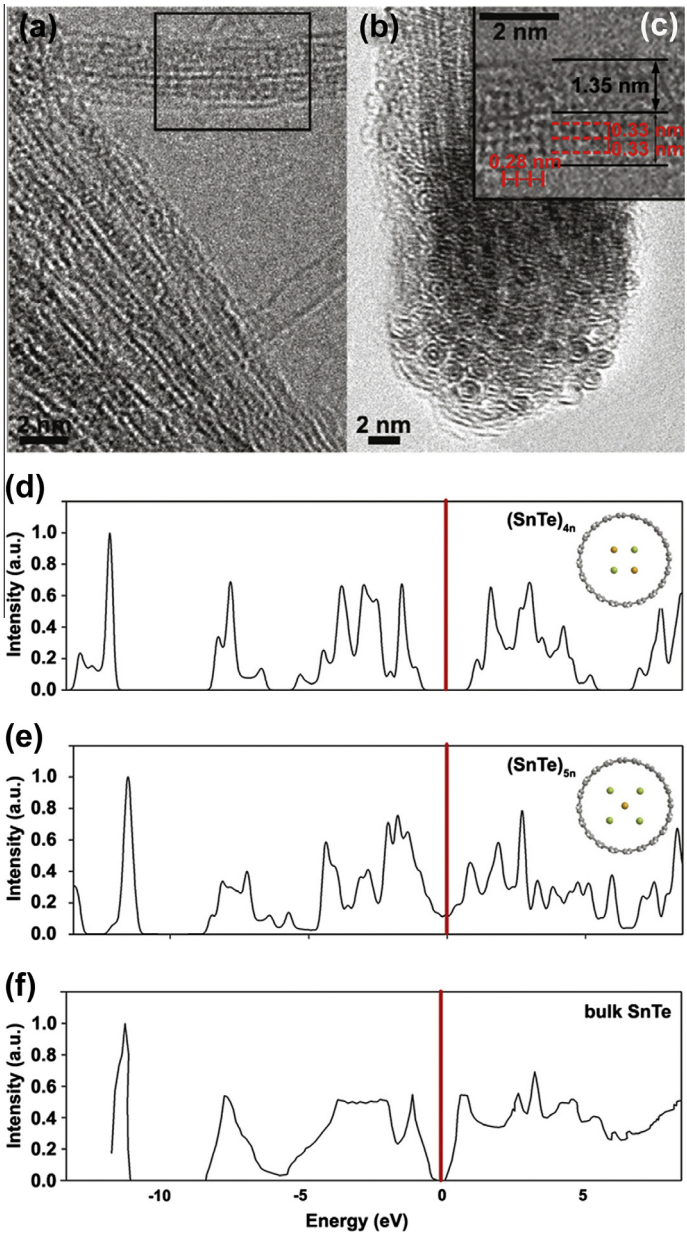


**Fig. 37.** The HRTEM micrographs of tin telluride-filled SWCNTs: (a) the filled SWCNT bundle, (b) cross-sectional view of the filled nanotube bundle, (c) high-magnification image of the nanotube bundle observed in (a), as denoted by the black rectangle. In the micrograph (c) the derived structural parameters are indicated: the nanotube diameter is 1.35 nm, the distance between atoms along the diameter direction is 0.33 nm and the periodicity along the tube axis is 0.28 nm. The calculated total density of states of the 1D nanocrystals $(SnTe)_{4n}$ (d), $(SnTe)_{5n}$ (e) and bulk tin telluride (f). The Fermi level is denoted by the red line. The insets show the optimized geometries of two structures of the 1D SnTe crystal. The carbon atoms are represented as gray balls, and tin and tellur atoms – as yellow and green balls. Adapted with permission from Yashina LV et al. J Phys Chem C 2011;115:3578. Copyright 2011 American Chemical Society [323].

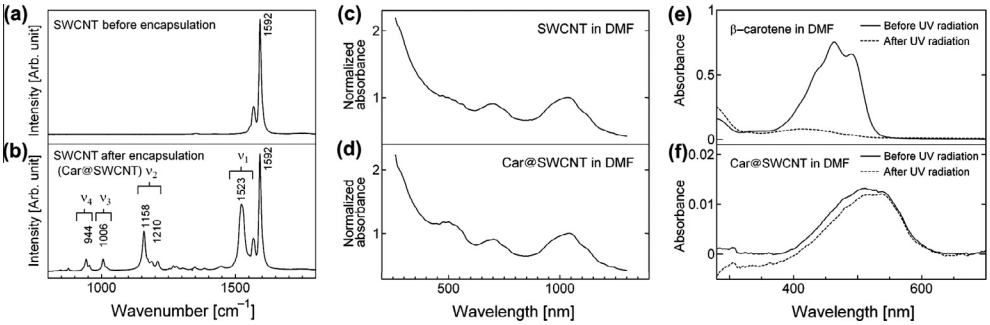


**Fig. 38.** The Raman spectra of the SWCNTs before (a) and after (b) the incorporation of β-carotene. The peaks $\nu_1$, $\nu_2$, $\nu_3$, and $\nu_4$ correspond to the characteristic Raman signal from β-carotene molecules. The numbers denote the peak positions. The optical absorption spectra of the pristine (c) and β-carotene-filled (d) SWCNTs in dimethylformamide (DMF) solution. The new peak at 488 nm in the spectrum (d) belongs to β-carotene. (e) The optical absorption spectra of β-carotene in the DMF solution before (solid line) and after (dotted line) the UV irradiation, which demonstrate the vanishing of the absorption band of β-carotene after the irradiation. (f) The difference optical absorption spectra between the β-carotene-filled nanotubes and pristine SWCNTs before (solid line) and after (dotted line) the UV irradiation, which demonstrate the keeping of the absorption band of the encapsulated β-carotene after the irradiation. Reprinted with permission from Yanagi K et al. Adv Mater 2006;18:437. Copyright 2006 Wiley-VCH Verlag GmbH & Co. KGaA, Weinheim [289].

The Raman spectroscopy, optical absorption spectroscopy and X-ray photoelectron spectroscopy data testified that the tin telluride-filled SWCNTs exhibit their pristine intrinsic electronic properties, because no significant differences were found between the spectra of the pristine and filled nanotubes. This allowed investigating the electronic structure of quasi-free-standing 1D SnTe crystals without taking into account the interaction with the outer SWCNTs.

Fig. 37d–f shows the DFT calculation results of the total density of states for the one-dimensional SnTe crystals with two suggested structures: $(SnTe)_{4n}$ and $(SnTe)_{5n}$ in comparison with the DOS of bulk SnTe [323]. The optimized geometries of two structures are presented in the insets. The structure $(SnTe)_{4n}$ (see the inset in Fig. 37d) has 4 atoms in the cross section and 8 atoms in a unit cell. The structure $(SnTe)_{5n}$ (see the inset in Fig. 37e) has 5 atoms in the cross section and 10 atoms in a unit cell. Both structures can be derived from the tin telluride bulk structure by cutting it along the [100] direction [323]. The crystal projection observed in Fig. 37c fits to the $(SnTe)_{5n}$ structure well. The quantum confinement effect predicts an increase in the band gap of 1D semiconductor crystals as compared to the bulk crystals. However, the DFT calculations showed that the $(SnTe)_{5n}$ crystal exhibits metallic properties with a non-zero density of states at the Fermi level (Fig. 37e). At the same time, the $(SnTe)_{4n}$ crystal possesses a band gap of 2 eV (Fig. 37d), which is much higher than the value of 0.19 eV of the rocksalt tin telluride crystal (Fig. 37f). The gapless state of the $(SnTe)_{5n}$ crystal was explained by the contribution of the edge atoms possessing low coordination number (which amounts to 3) [323].

It was found that the encapsulation of bismuth telluride ($Bi_2Te_3$) inside the SWCNT channels also does not lead to a modification of their electronic properties [315]. Authors made this conclusion on the basis of the Raman spectroscopy and XPS data that did not demonstrate sufficient differences in the spectra of unfilled and filled SWCNTs.

In Ref. [289], the nanohybrid consisting of highly stabilized β-carotene inside the SWCNT channels (Car@SWCNT) was prepared using the solution filling method. It was shown that this $\pi$-conjugated molecule, which is easily degraded under ambient conditions by reactions with radical species and trans-to-cis isomerizes under illumination by light or as a result of heat treatment [289], can be protected from these transformations by encapsulation inside the SWCNT channels. The filled nanotubes were investigated by Raman spectroscopy and optical absorption spectroscopy (Fig. 38a–d) [289]. No differences between the spectra of the pristine and filled nanotubes were found except for the appearance of additional peaks of β-carotene. In the Raman spectrum of the filled SWCNTs (Fig. 38b), there are four peaks ($\nu_1$, $\nu_2$, $\nu_3$, and $\nu_4$) that relate to the characteristic Raman signal from β-carotene

molecules. In the optical absorption spectrum of the filled nanotubes (Fig. 38d), there is one additional peak at 488 nm that belongs to β-carotene. These data testify to the filling of the SWCNTs with β-carotene molecules and show that no charge is transferred in the filled nanotubes [289]. Authors compared the UV radiation stabilities of free β-carotene and the molecule encapsulated inside the SWCNT channels. Fig. 38e and f shows the absorption spectra of two samples in dimethylformamide (DMF) solution before (solid line) and after (dotted line) the irradiation with UV light [289]. The absorption band of β-carotene in the DMF solution almost vanishes after the UV irradiation (Fig. 38e), whereas the absorption band of the encapsulated β-carotene is still kept after the irradiation (Fig. 38f). This clearly proves that the incorporation can suppress the light degradation of the molecule [289]. The demonstrated protection from degradation is a crucial step toward applications of π-conjugated molecules in photonic devices.

## 7. Tailoring the electronic properties by nanochemical reactions inside the SWCNT channels

Conducting chemical reactions inside the SWCNT channels allows controllable changing their electronic properties. This section is dedicated to discussing the modifications of the SWCNT electronic properties taking place as a result of chemical transformations of the encapsulated substances.

### *7.1. Nanochemical reactions with the formation of DWCNTs*

Among the chemical reactions carried out inside the SWCNT channels that lead to the modification of their electronic properties, the ones involving the formation of DWCNTs are most intensively studied. Indeed, an exposure to high temperatures may lead to a chemical transformation of the incorporated precursor that is accompanied by a change in its influence on the electronic properties of nanotubes. The subsequent growth of inner nanotubes also leads to the modification of the electronic properties of the nanostructure. The selection of conditions for the nanochemical reaction (type of precursor, temperature and duration) may give the possibility to tweak the SWCNT doping level and even to reverse the direction of charge transfer. This makes such nanotube-based hybrids promising components for future electronic devices.

#### *7.1.1. Transformation of precursors to inner tubes*

Different substances were found to be suitable precursors for the growth of DWCNTs: fullerenes ($C_{60}$ [339–348] and $C_{70}$ [341,342]), endohedral fullerenes ($Gd@C_{82}$ [49,250,256]), metallocenes (ferrocene [50,257–261,264–268,284], cerocene [51,269]), metal acetylacetonates ($Pt(C_5H_7O_2)_2$ [266,270]) and other molecules (toluene + $C_{60}$ [349], anthracene [350]), which were discussed in Section 5.2.5. The thermal treatment of the precursor-filled SWCNTs led to the formation of DWCNTs.

The main tool used to confirm the formation of inner tubes inside the SWCNTs is Raman spectroscopy. The position of peaks in the RBM band of the Raman spectra is inversely proportional to the nanotube diameter [413]. It means that the formation of inner tubes that possess smaller diameter than the outer SWCNTs corresponds to the appearance of additional peaks in the RBM band at higher frequencies. Fig. 39a compares the RBM-region of Raman spectra acquired at laser energy of 1.16 eV of the pristine, ferrocene-filled SWCNTs and the $FeCp_2$-filled sample annealed at 600 °C for 2 h and at 1150 °C for 1 h [265]. The Raman spectrum of ferrocene-filled SWCNTs contains the RBM peaks which are upshifted and broadened as compared to those of the pristine nanotubes, which is common for molecule-filled SWCNTs [265]. The Raman spectra of annealed samples demonstrate the appearance of additional peaks at frequencies in the range of 300–350 $cm^{-1}$, which were assigned to the RBM signals from the (6,5) and (7,3) inner nanotubes [265].

Further confirmation of the DWCNT formation was provided by the HRTEM data. Fig. 39b–d shows the micrographs of ferrocene-filled SWCNTs annealed at 600 °C for 2 h and 1150 °C for 1 h [265]. Fig. 39b demonstrates the growing inner tube (showing two parallel dark lines) as well as amorphous contrasts (corresponding to the precursor nanoparticles) inside a SWCNT. Fig. 39c shows an SWCNT containing the growing inner tube with capped end inside the channel. Fig. 39d displays the HRTEM image of the sample annealed at 1150 °C for 1 h showing a clean formed DWCNT.

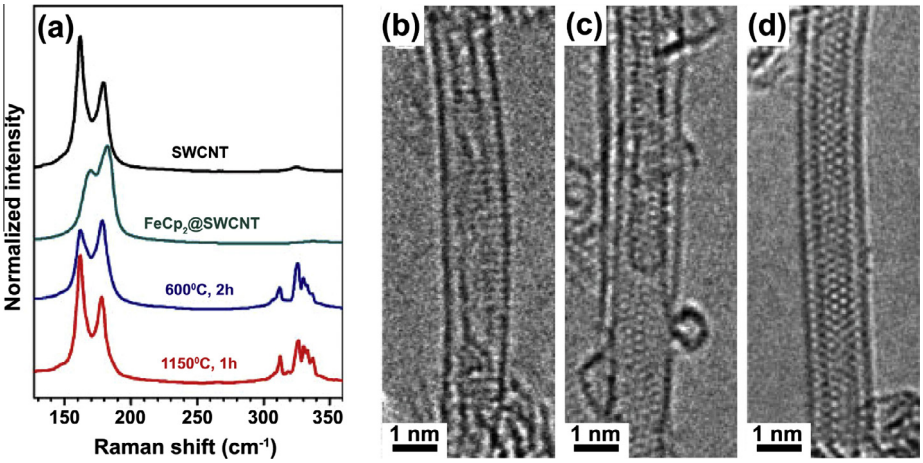


**Fig. 39.** (a) The RBM-region of Raman spectra acquired at a laser energy of 1.16 eV of the pristine, ferrocene-filled SWCNTs and $FeCp_2$-filled sample annealed at 600 °C for 2 h and at 1150 °C for 1 h. The new peaks in the spectra of the annealed samples at frequencies ranging from 300 to 350 $cm^{-1}$ correspond to the (6,5) and (7,3) inner nanotubes. The HRTEM micrographs of ferrocene-filled SWCNTs annealed at 600 °C for 2 h (b and c) and at 1150 °C for 1 h (d), which confirm the growth of inner tubes inside the SWCNTs. Reprinted with permission from Shiozawa H et al. Adv Mater 2008;20:1443. Copyright 2008 Wiley-VCH Verlag GmbH & Co. KGaA, Weinheim [265].

*7.1.2. Characterization of electronic properties of filled SWCNTs and DWCNTs*

The modification of the electronic properties of precursor-filled SWCNTs as a result of the DWCNT growth was investigated by X-ray photoemission spectroscopy, X-ray absorption spectroscopy and ultraviolet photoemission spectroscopy.

The possibility of switching between *p*- and *n*-doping as a result of precursor transformation inside the SWCNT channels was proven for Gd@$C_{82}$-filled nanotubes [49,256]. Encapsulated endohedral fullerenes caused *p*-doping of nanotubes, as it was discussed in Section 6.1.2. The thermal annealing of metallofullerene-filled SWCNTs led to the formation of Gd nanowires inside the DWCNTs, which, in turn, had strong *n*-doping effect on the nanotubes [49,256].

The use of resonant valence band photoemission spectroscopy across the Gd 4*d* edge allowed detailed studies of the density of states at the Fermi level for the Gd@$C_{82}$-filled SWCNTs and Gd-filled DWCNTs. This technique is based on the photoemission process that is resonantly enhanced by the participation of an electron excited in an X-ray absorption process. This additional electron ends up in the valence band and then another electron is ejected and contributes to the photoemission process [256]. Fig. 40 shows the series of the resonant valence band photoemission spectra recorded across the Gd 4*d* edge for the metallofullerene-filled SWCNTs and Gd nanowire-filled DWCNTs. The photon energies at which the spectra were acquired correspond to values before (135 eV), on- (149 eV) and after (180 eV) the resonance observed in the Gd 4*d* XAS response for both samples [256]. All spectra include the characteristic $\pi$- and $\sigma$-resonances of SWCNTs positioned at the binding energy of 3 and 8 eV, respectively. In the on-resonance spectra, an additional peak at the binding energy of 12 eV is observed, which corresponds to the resonance enhancement of the Gd 4*f* signal (the $4f^7$ multiplet) [256].

An enhancement of the photoemission response at the Fermi level on the Gd resonance is not observed for the Gd@$C_{82}$-filled SWCNTs (Fig. 40). This indicates that the Gd ions are isolated within the metallofullerenes and that the charge transfer to the fullerene cage does not result in the formation of metallic fullerene chains inside the SWCNTs [256]. In contrast, the spectra of the Gd-filled DWCNTs demonstrate a strong increase in the density of states at the Fermi level (as it is shown for example in the inset in Fig. 40 for the spectra recorded before the resonance). This fact proves that these samples have increased metallicity in comparison with the Gd@$C_{82}$-filled SWCNTs. The authors of Ref. [256] noted that the observation of the Fermi edge of the Gd-filled DWCNTs showed that the

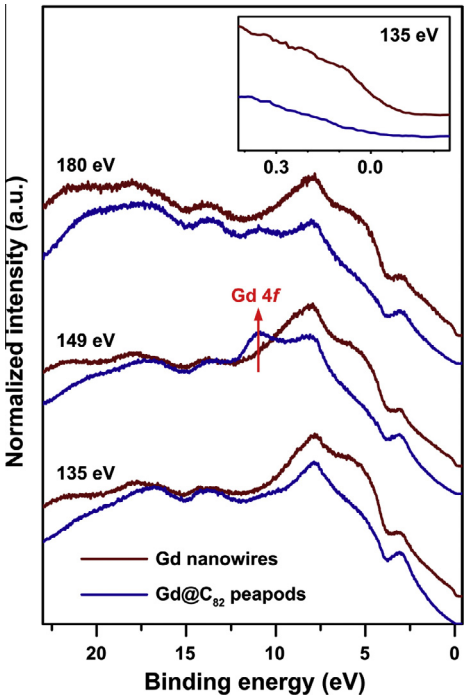


**Fig. 40.** The series of the resonant valence band photoemission spectra recorded across the Gd 4*d* edge for the Gd@$C_{82}$-filled SWCNTs (blue lines) and Gd nanowire-filled DWCNTs (dark red lines). The spectra are acquired at photon energies of 135 eV, 149 eV and 180 eV, which correspond to values before, on- and after the Gd 4*d* resonance. An additional peak at the binding energy of 12 eV (denoted by the red arrow) in the on-resonance spectra corresponds to the resonance enhancement of the Gd 4*f* signal (the $4f^7$ multiplet). The inset shows the vicinity of the Fermi level in the spectra recorded before the resonance. It demonstrates a strong increase of the density of states at the Fermi level for the Gd nanowire-filled DWCNTs. The data are replotted from Ref. [256].

nanotubes are highly doped. As a result, the nanotube bundle is driven into a metallic state, and in this case the charge transfer from the Gd nanowires induces the transition of the Tomonaga–Luttinger liquid ground state of a 1D metal [80,414,415] into a normal Fermi liquid state.

The possibility of increasing the SWCNT doping level *via* precursor transformation inside their channels was demonstrated for cerocene-filled nanotubes [51,269]. Incorporated cerocene caused *n*-doping of the nanotubes, which was discussed in Section 6.2.2. Authors of Ref. [51] found that the thermal decomposition of cerocene inside the SWCNT channels with formation of DWCNTs led to an enhancement of the density of conduction electrons; moreover, the transition of cerium-containing semiconducting nanotubes to the metallic state caused an increase in screening of the photoexcited core hole potential.

Fig. 41a and b demonstrates the photoemission spectra of the pristine, cerocene-filled SWCNTs and Ce-containing DWCNTs [51]. Fig. 41a compares the Ce $3d \rightarrow 4f$ on-resonance photoemission spectra of these samples. The spectra are similar and include a single peak placed at a binding energy of 2 eV belonging to the Ce $4f^1 \rightarrow 4f^0$ transition [51]. Fig. 41b compares the Ce 3*d* off-resonance spectra, which are different for the samples. The spectrum of Ce-containing DWCNTs demonstrates a significant increase of the DOS at the Fermi level as compared to the spectra of the pristine and cerocene-filled SWCNTs. This was interpreted as electron doping beyond the first van Hove singularity in the conduction band of semiconducting nanotubes, which led to the enhanced conductivity of the nanotube bundles [51]. These data were in agreement with the X-ray absorption spectroscopy results shown in Fig. 41c. The C 1*s* XAS spectra of annealed samples containing the peak of the $\pi^*$-resonance

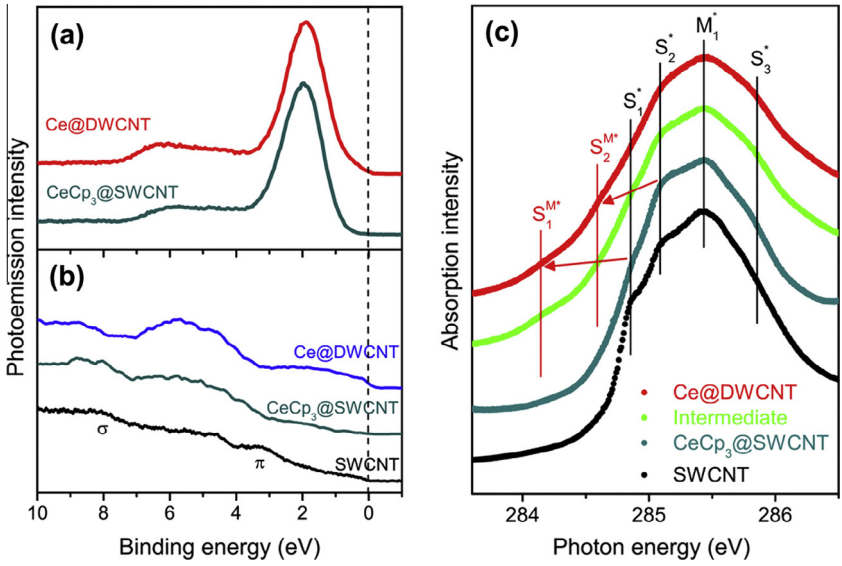


**Fig. 41.** The Ce 3*d* on-resonance (a) and off-resonance (b) photoemission spectra of the pristine, cerocene-filled SWCNTs and Ce-containing DWCNTs. The positions of the $\pi$ and $\sigma$ resonances are marked in the off-resonance spectra. The dashed vertical line denotes the Fermi level. (c) The C 1*s* X-ray absorption spectra containing the $\pi^*$-resonance of the pristine, cerocene-filled SWCNTs and the annealed samples (intermediate sample and Ce-containing DWCNTs). The positions of the peaks corresponding to the first, the second and the third vHs of semiconducting SWCNTs and the first vHs of metallic nanotubes ($S_1^*$, $S_2^*$, $S_3^*$ and $M_1^*$, respectively) are denoted by black vertical lines. The annealed samples demonstrate the suppression of the $S_1^*$ and $S_2^*$ peaks and appearance of two new peaks$S_1^{M^*}$ and $S_2^{M^*}$, as shown by arrows. The positions of new peaks are marked by red vertical lines. Reprinted figure with permission from Shiozawa H et al. Phys Rev Lett 2009;102:046804. Copyright 2009 by the American Physical Society [51].

demonstrate a significant suppression of the peak components corresponding to the first and the second vHs of semiconducting SWCNTs (labeled $S_1^*$ and $S_2^*$ in Fig. 41c) and the appearance of two new peak components (denoted $S_1^{M^*}$ and $S_2^{M^*}$ in Fig. 41c) due to electron doping of the semiconducting nanotubes [51].

The possibility of fine tuning the SWCNT doping level and achieving both *n*- and *p*-type doping *via* the interconversion of incorporated molecules was demonstrated for ferrocene-filled SWCNTs [50,267]. The variation of time and temperature of thermal annealing of ferrocene-filled nanotubes resulting in the DWCNT formation allowed tailoring precisely their Fermi level.

Fig. 42a shows the C 1*s* X-ray photoelectron spectra of the pristine, ferrocene-filled SWCNTs and $FeCp_2$-filled samples annealed at 600 °C for 2 and 22 h [50]. The C 1*s* peak of ferrocene-filled nanotubes is much broader and more asymmetric than that of the pristine SWCNTs. This may be due to the C 1*s* response from ferrocene present inside the nanotubes as well as changes in the chemical environment of carbon atoms as a result of the filling [267]. In contrast, the spectra of annealed samples almost recover the shape of the spectrum of pristine SWCNTs. Furthermore, the C 1*s* peaks of annealed samples are slightly shifted toward lower binding energies, which can be attributed to changes in the electronic properties of nanotubes.

Tracing the van Hove singularity peaks in the valence band spectra acquired by ultraviolet photoelectron spectroscopy allowed the detailed investigation of the degree of charge transfer between the nanotube and filler (Fig. 42b) [50]. The spectrum of ferrocene-filled SWCNTs demonstrates the shift of the vHs peaks to higher binding energies as compared to the spectrum of the pristine SWCNTs testifying to *n*-type doping of nanotubes, which was discussed in Section 6.2.2. Upon annealing at 600 °C the vHs peaks are gradually shifted to lower binding energies and eventually surpass those of the pristine SWCNTs (at this stage, the samples consist of iron doped DWCNTs) [50].

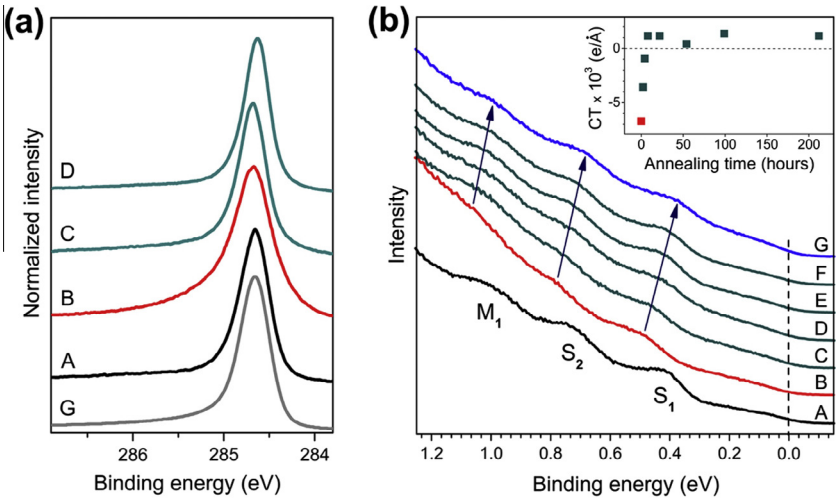


**Fig. 42.** (a) The C 1*s* X-ray photoelectron spectra of the pristine (A), ferrocene-filled SWCNTs (B), Fe-containing DWCNTs obtained after annealing at 600 °C for 2 h (C) and 22 h (D). Gray spectrum (G) is a Doniach-Sunjic profile convoluted with a Gaussian reproducing well the C 1*s* peak of the SWCNTs. The data are replotted from Ref. [50]. (b) The valence band spectra of the pristine (A), ferrocene-filled SWCNTs (B), Fe-containing DWCNTs obtained after annealing at 600 °C for 2 h (C), 8 h (D), 54 h (E) and 212 h (F) and at 1150 °C for 1 h (G). The peaks corresponding to the first and the second vHs of semiconducting SWCNTs and the first vHs of metallic nanotubes are denoted by symbols $S_1$, $S_2$ and $M_1$, respectively. The shift of the vHs peaks upon annealing steps is shown by arrows. The Fermi level is marked by the dashed vertical line. The inset shows the annealing time dependence of the charge transfer density (CT) for the outer tube in units of $e^-$/Å. Reprinted figure with permission from Shiozawa H et al. Phys Rev B 2008;77:153402. Copyright 2008 by the American Physical Society [50].

Upon annealing at 1150 °C the vHs peaks are further shifted to lower energies (at this stage, the sample consists of empty DWCNTs) [50]. This proves that the annealing of ferrocene-filled SWCNTs results in a change of the doping type of nanotubes from *n* to *p*. Moreover, the increase in annealing duration and temperature of treatment enhances the *p*-doping level. The authors of Ref. [50] explained this tendency by the fact that the annealing of sample increased the content of empty DWCNTs, exhibiting charge transfer from the outer tube to the inner tube.

The inset in Fig. 42b demonstrates the dependence of the calculated charge transfer density (CT) on the outer tube per unit length for different durations of annealing at 600 °C. The charge transfer density has a maximum negative value of $-0.0067\ e^-$/Å for ferrocene-filled SWCNTs, it decreases drastically at the first annealing steps and saturates at a positive constant value around $+0.0010\ e^-$/Å after 8 h of annealing [50].

### 7.2. Other nanochemical reactions

The electronic properties of SWCNTs can also be modified *via* chemical reactions without inner tube formation inside their channels.

Authors of Ref. [304] performed the investigation of the electronic properties of nanotubes filled with erbium chloride $ErCl_3$ *via* the melt method and the erbium-filled SWCNTs obtained as result of their high-temperature annealing in vacuum. Fig. 43a shows the HRTEM data of erbium chloride-filled SWCNTs and the same sample after annealing [304]. The low-magnification micrograph in Fig. 43a1 demonstrates the overall morphology of the $ErCl_3$-filled SWCNTs. The high-resolution image in Fig. 43a2 presents an individual filled nanotube. Both low and high-magnification micrographs in Fig. 43a1 and a2 demonstrate a high filling ratio and crystallinity of $ErCl_3$ inside the SWCNTs. The HRTEM micrographs of filled nanotubes after heat treatment obtained in low-magnification (Fig. 43a3) and high-magnification (Fig. 43a4 and a5) regimes demonstrate erbium nanowires inside

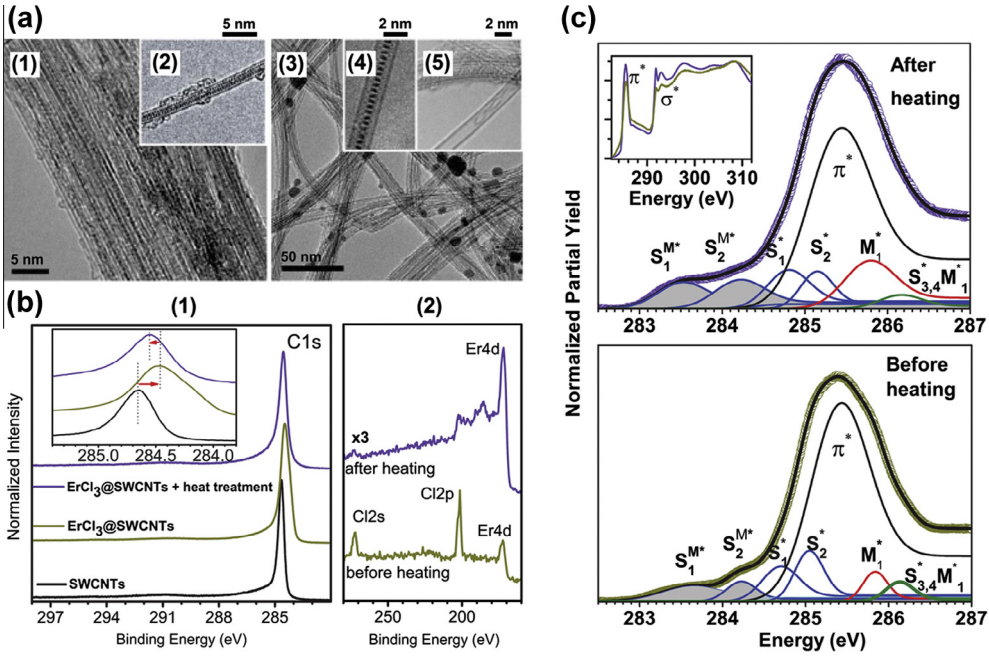


**Fig. 43.** (a) The HRTEM images obtained in low-magnification and high-magnification regime of the erbium chloride-filled SWCNTs (1 and 2, respectively) and erbium-containing SWCNTs (3 and 4, 5, respectively). The scales shown on the top of the high-magnification images are made on the basis of the given nanotube mean diameter (1.9 nm). (b) The X-ray photoelectron spectra of the pristine, $ErCl_3$-filled SWCNTs and the heated sample acquired in the C 1*s* core level region (1) and in the survey scan regime (2). The inset to (1) zooms in the maxima of the C 1*s* peaks. Their positions are denoted by the dashed vertical lines. The shifts of the peak positions are shown by arrows. In the spectra (2) the assignment of the observed peaks is shown by symbols. (c) The C 1*s* X-ray absorption spectra of the erbium chloride-filled SWCNTs (dark yellow) and heated sample (violet). The inset demonstrates the overall C 1*s* XAS spectra, which include the $\pi^*$- and $\sigma^*$-resonances, and the main panels show the region of the spectra containing the $\pi^*$-resonance. The recorded data (plotted in circles) are shown together with their fitting with the peaks of the overall conduction band $\pi^*$ and individual vHs. The symbols $S_1^*$, $S_2^*$, $S_{3,4}^*$ and $M_1^*$ denote the first, the second, the third/fourth vHs of semiconducting SWCNTs and the first vHs of metallic nanotubes, respectively. The peaks with shaded area labeled $S_1^{M^*}$ and $S_2^{M^*}$ correspond to the screened vHs in the conduction band of semiconducting tubes. Reprinted figure with permission from Ayala P et al. Phys Rev B 2011;83:085407. Copyright 2011 by the American Physical Society [304].

the SWCNT channels. Their chemical composition was confirmed by the energy dispersive X-ray analysis.

A combination of X-ray photoelectron spectroscopy and X-ray absorption spectroscopy was employed as a versatile tool set to probe the charge transfer and bonding environment in the $ErCl_3$-filled SWCNTs and the annealed sample. Fig. 43b compares the XPS data of the pristine, erbium chloride-filled SWCNTs and erbium-filled nanotubes [304]. Fig. 43b1 shows the C 1*s* XPS spectra of the samples. The C 1*s* peak of $ErCl_3$-filled SWCNTs is shifted to lower binding energies as compared to the peak of pristine nanotubes, and there is also a shoulder appearing at lower binding energies. This shoulder testifies to a finite hybridization of the erbium chloride states with the SWCNT $\pi$-orbitals. The C 1*s* XPS spectrum of the annealed sample (Fig. 43b1) demonstrates the shift of the peak back to higher binding energies (slightly lower than the position of pristine SWCNTs) and smearing out of the shoulder. The spectral changes are in line with the formation of Er nanowires inside the SWCNT channels, which is further corroborated by the XPS survey scan spectra (Fig. 43b2), demonstrating the decomposition of the $ErCl_3$ and the loss of the Cl atoms after annealing.

Fig. 43c shows the C 1*s* X-ray absorption spectra of the erbium chloride-filled SWCNTs and heated sample. The inset demonstrates the overall C 1*s* XAS spectra, which include the $\pi^*$- and $\sigma^*$-resonances. The main panels show the region of the spectra containing the $\pi^*$-resonance together with a

line-shape analysis that includes the individual vHs peaks. The labels $S_1^*$, $S_2^*$, $S_{3,4}^*$ and $M_1^*$ indicate the first, the second, the third/fourth vHs of semiconducting SWCNTs and the first vHs of metallic nanotubes, respectively, and $S_1^{M^*}$, $S_2^{M^*}$ correspond to the vHs of semiconducting tubes where the core holes are screened by the encapsulated material [304]. The peaks of the screened vHs are increased in the spectrum of the annealed sample, which can be attributed to an additional charge transfer in the sample after heat treatment as a result of stronger hybridization between the nanotube $\pi$-states and the Er 5*d* orbitals [304]. This was also proven by resonant photoemission spectra recorded across the Er 4*d* and 3*d* edges, showing a reduced effective valence of the Er in the nanowire hybrid [304].

## 8. Applications of filled nanotubes

The possibility of incorporating specific substances into the SWCNT channels and controlling the nanotube doping level makes these nanostructures promising candidates for applications in different fields. This section is dedicated to the discussion of possible (demonstrated and expected) applications of filled SWCNTs.

### 8.1. Nanoelectronic devices

The most promising applications of filled nanotubes are in the field of nanoelectronics [16,53,54,239,247,277,332,416–425].

It was suggested that the filled SWCNTs can be used for very effective nanoelectronic circuits [334]. An air-stable *p*–*n* junction was created in Ref. [420] as result of the partial filling of the SWCNT channel with iron. Later on, the possibility to realize an air-stable *p*–*n* junction as result of piecewise filling the SWCNT channel with electron donor and acceptor substances (cesium and iodine, and also cesium and fullerene $C_{60}$ molecules) was pioneered in Ref. [334]. Also, it was found that the transport properties of SWCNTs are directly dependent on the doping level, and it is possible to control them during the SWCNT filling process [332].

Authors of Ref. [424] showed that the SWCNTs filled with fullerene $C_{60}$ molecules can be used as channels of field effect transistors with *p*-type conductivity. At the same time, it was demonstrated that the encapsulation of endohedral fullerene Gd@$C_{82}$ inside the SWCNT inner cavities led to a decrease of the SWCNT band gap from about 0.5 eV to about 0.1 eV, and on the basis of these findings the use of nanostructures as the channels of transistors with ambipolar conductivity type was proposed [419,422,424].

The temperature dependence of the conductivity type of the SWCNTs filled with the molecules of endohedral fullerene Dy@$C_{82}$ was found in Refs. [247,416]. These nanostructures had *p*-type conductivity at room temperature, but cooling them down to 265 K switched the conductivity to *n*-type. Fig. 44a shows the atomic force microscopy (AFM) image and the sketch of the device fabricated for the transport measurements in Ref. [247]. The device was constructed on a silicon dioxide insulating layer on top of a degenerately doped silicon substrate, which functioned as a back-gate electrode modulating the electrostatic potential of the Dy@$C_{82}$-filled nanotube [247]. The resulting gate voltage dependencies of the conductance along the nanotube at room temperature (300 K) and at 265 K are shown in Fig. 44b and c. The dependence measured at room temperature (Fig. 44b) demonstrates the increase of the conductance at negative gate voltages, indicating the *p*-type semiconducting behavior of the peapod. The dependence measured at 265 K (Fig. 44c) demonstrates the increase of the conductance at positive gate voltages, indicating the *n*-type semiconducting behavior of the peapod due to extra electrons on the nanotube. Decreasing the gate voltage leads to a complete suppression of the conductance (Fig. 44c) [247].

### 8.2. Electrochemical energy storage

The use of filled nanotubes for electrochemical energy storage and production was among the earliest suggested applications of filled nanotubes [57]. It was demonstrated in Ref. [426] that the pseudocapacitance effects connected with the presence of high capacity chromium oxide inside

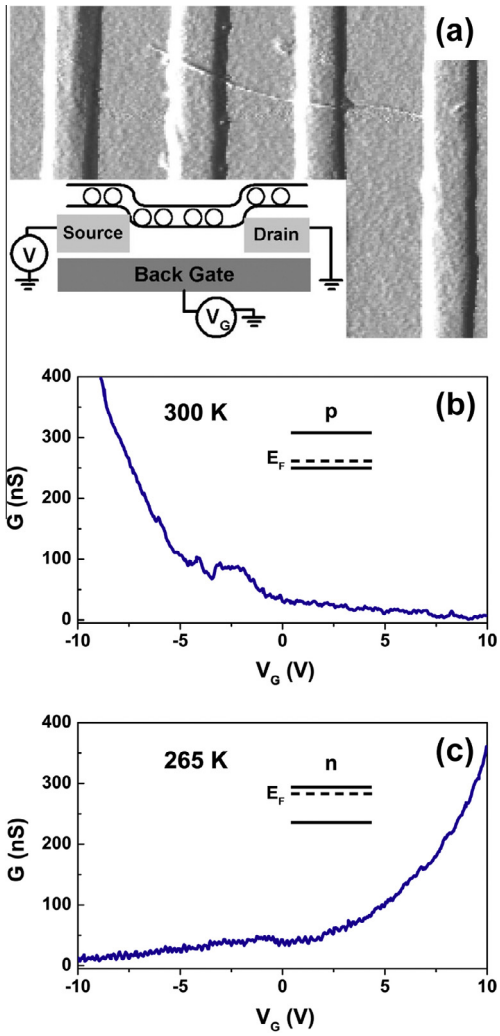


**Fig. 44.** (a) The atomic force microscopy image of an individual Dy@$C_{82}$-filled SWCNT 1.5 nm in height, which was adsorbed from a dispersion on top of predefined electrodes with a spacing of 150 nm. The inset shows the sketch of the device fabricated for the transport measurements. Reprinted with permission from Chiu PW et al. Appl Phys Lett 2001;79:3845. Copyright 2001, AIP Publishing LLC [247]. The dependencies of the conductance along the nanotube (G) on gate voltage ($V_G$) at 300 K (b) and at 265 K (c). The insets demonstrate the schemes of the band diagrams. The upper solid horizontal line represents the bottom of the conduction band, the lower – the top of the valence band. At 300 K (b) the peapod has the *p*-type semiconducting behavior, and the Fermi level (shown as the dashed horizontal line) is placed near the top of the valence band of SWCNTs. At 265 K (c) the peapod has the *n*-type semiconducting behavior, and the Fermi level is positioned near the bottom of the conduction band of SWCNTs. The data are replotted from Ref. [247].

the channels of highly conductive SWCNTs open the way to use these nanostructures for building efficient electrodes of supercapacitors. The authors showed that the encapsulation of nanoparticles of chromium oxide into the SWCNTs led to an increase in the charging rate of the electrical double layer and fast faradaic reactions. The achieved capacitance of the system was 60 F $g^{-1}$, and the charge propagation was observed to be exceptionally quick. This was explained by the peculiarities of physical and textural properties of the $CrO_3$-filled SWCNTs [426].

### 8.3. Catalyst support

The filled nanotubes can also be used as a catalyst support. It was suggested in Ref. [336] that the clusters of transition metals located inside the SWCNT channels may be promising for catalytic applications, because the nanoparticles of smaller size have larger catalytic activity; moreover, the nanotubes of small diameters influence the course of chemical reactions. The SWCNTs filled with nanoparticles of a catalyst can be mixed with the components of a chemical reaction, and the nanotube wall will prevent the nanoparticles from the direct contact with them. Under special conditions, the SWCNT wall can be damaged that leads to releasing the catalytic particles [55].

### 8.4. Biomedical applications

The filled SWCNTs can also be employed for biomedical applications. One of them is the use as nanocontainers for the delivery of contrast agents to organism tissues in order to perform the investigations by magnetic resonance imaging (MRI). As pointed out in Ref. [57], the contrast agents like gadolinium [427] or iron oxide [428] that are contained inside the SWCNTs will be less likely to interact with the surrounding tissue and being excreted from the organism more quickly. The contrast agents can be directly delivered to certain body tissues and provide molecular level contrast and biosensing [428]. Additionally, these nanostructures can be used for hyperthermic treatment of cancer *via* selective heating by applying the magnetic field of the diseased tissue that was previously impregnated with magnetic particle-containing nanotubes.

It was suggested that the nanotubes containing endohedral fullerenes with incorporated radioactive atoms can be used as markers for radiographic investigations of organisms [55].

Another biomedical application of filled SWCNTs is targeted drug delivery. The medicines chemically attached to fullerenes that are encapsulated inside the nanotube channels can be delivered to different parts of the body, organs or cells [55]. In these cases, a nanotube acts both as a nanocontainer for medicine delivery and a nanosyringe for its injection.

### 8.5. Other applications

Besides the cases discussed above, the filled SWCNTs can have applications in other fields. It was demonstrated in Ref. [429] that the nanotubes containing fullerene and endohedral fullerene molecules can be used for processing quantum information, which provides a possible route for building a quantum computer.

The authors of Ref. [430] demonstrated that the SWCNTs filled with copper iodide have a small work function, and it paves the way to use such nanostructures for the creation of field emitters of electroluminescence and X-ray tubes [54].

Also, it was suggested that the SWCNTs filled with fullerenes containing special functional groups may be used as active elements in sensors [298].

## 9. Summary and outlook

The single-walled carbon nanotubes are a promising material for electronic applications, because of their unique properties. Developing methods of tailoring the SWCNT electronic properties is a key step to realize potential applications of nanotubes in devices.

In the present review, the methods of filling the SWCNT internal channels and chemical transformation of encapsulated substances were discussed with a view to their use for tailoring the electronic properties of nanotubes. These methods are promising for the modification of the SWCNT electronic properties, because of the following reasons. Firstly, a long list of substances possessing different chemical and physical properties can be introduced into the nanotube channels. This was demonstrated *via* the systematization of electron acceptors and donors encapsulated into the SWCNTs. Secondly, various approaches can be used to fill the internal channels of nanotubes with different substances. This was shown by the analysis of literature data and classification of filling

methods of the SWCNTs. These methods are well-established. This was illustrated by the description of the filling methods and comparison of their effectiveness for the encapsulation of various substances inside the nanotubes. Thirdly, the process of incorporation can lead to large filling degrees of the SWCNT internal channels, and it may cause significant changes in the electronic properties of nanotubes. This was demonstrated by the analysis and summary of the results reported on experimental and theoretical investigations of the electronic properties of filled nanotubes. Fourthly, the chemical reactions inside the SWCNT channels open the way of fine tuning the SWCNT electronic structure by choosing a suitable precursor and conditions for the reaction. This was illustrated by the systematization of precursors for the DWCNT formation, methods of their encapsulation and transformation and the analysis of the data on the characterization of the electronic properties of these nanostructures.

This review is the result of a detailed systematic investigation of more than 400 reports, most of which were published in the last five years, because the field of studying the electronic properties of filled SWCNTs is actively developing. The substances incorporated into the SWCNTs were for the first time categorized by their influence on the electronic properties of nanotubes, and the reported data on the modification of the electronic properties of the SWCNTs as a result of the filling and the nanochemical reactions inside their channels were analyzed and summarized.

In conclusion, virtually all of the reports discussed here were dedicated to the tailored modification of the electronic properties of bundled SWCNTs and their spectroscopic investigations on the bulk scale. The established methods and knowledge about the modified electronic properties provide the fundamentals for functioning devices on the basis of functionalized nanotubes. The next step toward applications of these nanostructures should be applying the approaches of tailoring the electronic properties to individual nanotubes, which can be integrated into nanoelectronic devices.

## References


[1] Iijima S, Ichihashi T. Single-shell carbon nanotubes of 1-nm diameter. Nature 1993;363:603–5.
[2] Saito R, Dresselhaus G, Dresselhaus MS. Physical properties of carbon nanotubes. London: Imperial College Press; 1998.
[3] Ajayan PM, Zhou OZ. Applications of carbon nanotubes. In: Dresselhaus MS, Dresselhaus G, Avouris A, editors. Topics in applied physics, vol. 80. Berlin: Springer; 2001. p. 391–425.
[4] Endo M, Strano MS, Ajayan PM. Potential applications of carbon nanotubes. In: Jorio A, Dresselhaus G, Dresselhaus MS, editors. Topics in applied physics, vol. 111. Berlin: Springer; 2008. p. 13–62.
[5] Smith BW, Monthioux M, Luzzi DE. Encapsulated $C_{60}$ in carbon nanotubes. Nature 1998;396:323–4.
[6] Sloan J, Hammer J, Zwiefka-Sibley M, Green MLH. The opening and filling of single walled carbon nanotubes (SWTs). Chem Commun 1998:347–8.
[7] Guan LH, Shi ZJ, Li MX, Gu ZN. Ferrocene-filled single-walled carbon nanotubes. Carbon 2005;43:2780–5.
[8] Hirahara K, Suenaga K, Bandow S, Kato H, Okazaki T, Shinohara H, et al. One-dimensional metallofullerene crystal generated inside single-walled carbon nanotubes. Phys Rev Lett 2000;85:5384–7.
[9] Luzzi DE, Smith BW. Carbon cage structures in single wall carbon nanotubes: a new class of materials. Carbon 2000;38:1751–6.
[10] Monthioux M, Smith BW, Burteaux B, Claye A, Fischer JE, Luzzi DE. Sensitivity of single-wall carbon nanotubes to chemical processing: an electron microscopy investigation. Carbon 2001;39:1251–72.
[11] Morgan DA, Sloan J, Green MLH. Direct imaging of o-carborane molecules within single walled carbon nanotubes. Chem Commun 2002:2442–3.
[12] Sloan J, Dunin-Borkowski RE, Hutchison JL, Coleman KS, Williams VC, Claridge JB, et al. The size distribution, imaging and obstructing properties of $C_{60}$ and higher fullerenes formed within arc-grown single walled carbon nanotubes. Chem Phys Lett 2000;316:191–8.
[13] Smith BW, Monthioux M, Luzzi DE. Carbon nanotube encapsulated fullerenes: a unique class of hybrid materials. Chem Phys Lett 1999;315:31–6.
[14] Smith BW, Luzzi DE. Formation mechanism of fullerene peapods and coaxial tubes: a path to large scale synthesis. Chem Phys Lett 2000;321:169–74.
[15] Suenaga K, Tence T, Mory C, Colliex C, Kato H, Okazaki T, et al. Element-selective single atom imaging. Science 2000;290:2280–2.
[16] Sun BY, Sato Y, Suenaga K, Okazaki T, Kishi N, Sugai T, et al. Entrapping of exohedral metallofullerenes in carbon nanotubes: $(CsC_{60})_n$@SWNT nano-peapods. J Am Chem Soc 2005;127:17972–3.
[17] Chancolon J, Archaimbault F, Pineau A, Bonnamy S. Filling of carbon nanotubes with selenium by vapor phase process. J Nanosci Nanotechnol 2006;6:82–6.
[18] Costa PMFJ, Sloan J, Rutherford T, Green MLH. Encapsulation of $Re_xO_y$ clusters within single-walled carbon nanotubes and their in tubulo reduction and sintering to Re metal. Chem Mater 2005;17:6579–82.
[19] Govindaraj A, Satishkumar BC, Nath M, Rao CNR. Metal nanowires and intercalated metal layers in single-walled carbon nanotube bundles. Chem Mater 2000;12:202–5.

[20] Kiang CH, Choi JS, Tran TT, Bacher AD. Molecular nanowires of 1 nm diameter from capillary filling of single-walled carbon nanotubes. J Phys Chem B 1999;103:7449–51.
[21] Sloan J, Wright DM, Woo HG, Bailey S, Brown G, York APE, et al. Capillarity and silver nanowire formation observed in single walled carbon nanotubes. Chem Commun 1999:699–700.
[22] Zhang ZL, Li B, Shi ZJ, Gu ZN, Xue ZQ, Peng LM. Filling of single-walled carbon nanotubes with silver. J Mater Res 2000;15:2658–61.
[23] Brown G, Bailey SR, Sloan J, Xu CG, Friedrichs S, Flahaut E, et al. Electron beam induced in situ clusterisation of 1D $ZrCl_4$ chains within single-walled carbon nanotubes. Chem Commun 2001:845–6.
[24] Brown G, Bailey SR, Novotny M, Carter R, Flahaut E, Coleman KS, et al. High yield incorporation and washing properties of halides incorporated into single walled carbon nanotubes. Appl Phys A 2003;76:457–62.
[25] Hulman M, Kuzmany H, Costa PMFJ, Friedrichs S, Green MLH. Light-induced instability of PbO-filled single-wall carbon nanotubes. Appl Phys Lett 2004;85:2068–70.
[26] Sloan J, Terrones M, Nufer S, Friedrichs S, Bailey SR, Woo HG, et al. Metastable one-dimensional $AgCl_{1-x}I_x$ solid-solution wurzite "tunnel" crystals formed within single-walled carbon nanotubes. J Am Chem Soc 2002;124:2116–7.
[27] Bendall JS, Ilie A, Welland ME, Sloan J, Green MLH. Thermal stability and reactivity of metal halide filled single-walled carbon nanotubes. J Phys Chem B 2006;110:6569–73.
[28] Fan X, Dickey EC, Eklund PC, Williams KA, Grigorian L, Buczko R, et al. Atomic arrangement of iodine atoms inside single-walled carbon nanotubes. Phys Rev Lett 2000;84:4621–4.
[29] Flahaut E, Sloan J, Friedrichs S, Kirkland AI, Coleman KS, Williams VC, et al. Crystallization of 2H and 4H $PbI_2$ in carbon nanotubes of varying diameters and morphologies. Chem Mater 2006;18:2059–69.
[30] Friedrichs S, Kirkland AI, Meyer RR, Sloan J, Green MLH. $LaI_2$@(18,3)SWNT: the unprecedented structure of a $LaI_2$ "crystal," encapsulated within a single-walled carbon nanotube. Microsc Microanal 2005;11:421–30.
[31] Guan LH, Suenaga K, Shi ZJ, Gu ZN, Iijima S. Polymorphic structures of iodine and their phase transition in confined nanospace. Nano Lett 2007;7:1532–5.
[32] Hutchison JL, Sloan J, Kirkland AI, Green MLH, Green MLH. Growing and characterizing one-dimensional crystals within single-walled carbon nanotubes. J Electr Microsc 2004;53:101–6.
[33] Kirkland AI, Meyer MR, Sloan J, Hutchison JL. Structure determination of atomically controlled crystal architectures grown within single wall carbon nanotubes. Microsc Microanal 2005;11:401–9.
[34] Kiselev NA, Zakalyukin RM, Zhigalina OM, Grobert N, Kumskov AS, Grigoriev YV, et al. The structure of 1D CuI crystals inside SWNTs. J Microsc – Oxford 2008;232:335–42.
[35] Kiselev NA, Kumskov AS, Zakalyukin RM, Vasiliev AL, Chernisheva MV, Eliseev AA, et al. The structure of nanocomposite 1D cationic conductor crystal@SWNT. J Microsc 2012;246:309–21.
[36] Kumskov AS, Eliseev AA, Freitag B, Kiselev NA. HRTEM of 1DSnTe@SWNT nanocomposite located on thin layers of graphite. J Microsc 2012;248:117–9.
[37] Meyer RR, Sloan J, Dunin-Borkowski RE, Kirkland AI, Novotny MC, Bailey SR, et al. Discrete atom imaging of one-dimensional crystals formed within single-walled carbon nanotubes. Science 2000;289:1324–6.
[38] Philp E, Sloan J, Kirkland AI, Meyer RR, Friedrichs S, Hutchison JL, et al. An encapsulated helical one-dimensional cobalt iodide nanostructure. Nat Mater 2003;2:788–91.
[39] Satishkumar BC, Taubert A, Luzzi DE. Filling single-wall carbon nanotubes with d- and f-metal chloride and metal nanowires. J Nanosci Nanotechnol 2003;3:159–63.
[40] Sloan J, Novotny MC, Bailey SR, Brown G, Xu C, Williams VC, et al. Two layer 4:4 coordinated KI crystals grown within single walled carbon nanotubes. Chem Phys Lett 2000;329:61–5.
[41] Sloan J, Kirkland AI, Hutchison JL, Green MLH. Integral atomic layer architectures of 1D crystals inserted into single walled carbon nanotubes. Chem Commun 2002:1319–32.
[42] Sloan J, Friedrichs S, Meyer RR, Kirkland AI, Hutchison JL, Green MLH. Structural changes induced in nanocrystals of binary compounds confined within single walled carbon nanotubes: a brief review. Inorg Chim Acta 2002;330:1–12.
[43] Sloan J, Grosvenor SJ, Friedrichs S, Kirkland AI, Hutchison JL, Green MLH. A one-dimensional $BaI_2$ chain with five- and six-coordination, formed within a single-walled carbon nanotube. Angew Chem Int Ed 2002;41:1156–9.
[44] Sloan J, Kirkland AI, Hutchison JL, Green MLH. Aspects of crystal growth within carbon nanotubes. CR Phys 2003;4:1063–74.
[45] Thamavaranukup N, Hoppe HA, Ruiz-Gonzalez L, Costa PMFJ, Sloan J, Kirkland A, et al. Single-walled carbon nanotubes filled with M OH (M = K, Cs) and then washed and refilled with clusters and molecules. Chem Commun 2004:1686–7.
[46] Corio P, Santos AP, Santos PS, Temperini MLA, Brar VW, Pimenta MA, et al. Characterization of single wall carbon nanotubes filled with silver and with chromium compounds. Chem Phys Lett 2004;383:475–80.
[47] Li LJ, Khlobystov AN, Wiltshire JG, Briggs GAD, Nicholas RJ. Diameter-selective encapsulation of metallocenes in single-walled carbon nanotubes. Nat Mater 2005;4:481–5.
[48] Takenobu T, Takano T, Shiraishi M, Murakami Y, Ata M, Kataura H, et al. Stable and controlled amphoteric doping by encapsulation of organic molecules inside carbon nanotubes. Nat Mater 2003;2:683–8.
[49] Pichler T, Kramberger C, Ayala P, Shiozawa H, Knupfer M, Rummeli MH, et al. Bonding environment and electronic structure of Gd metallofullerene and Gd nanowire filled single-wall carbon nanotubes. Phys Status Solidi B 2008;245:2038–41.
[50] Shiozawa H, Pichler T, Kramberger C, Gruneis A, Knupfer M, Buchner B, et al. Fine tuning the charge transfer in carbon nanotubes via the interconversion of encapsulated molecules. Phys Rev B 2008;77:153402.
[51] Shiozawa H, Pichler T, Kramberger C, Rummeli M, Batchelor D, Liu Z, et al. Screening the missing electron: nanochemistry in action. Phys Rev Lett 2009;102:046804.
[52] Joselevich E, Dai HJ, Liu J, Hata K, Windle AH. Carbon nanotube synthesis and organization. In: Jorio A, Dresselhaus G, Dresselhaus MS, editors. Topics in applied physics, vol. 111. Berlin: Springer; 2008. p. 101–65.
[53] Eliseev A, Yashina L, Kharlamova M, Kiselev N. One-dimensional crystals inside single-walled carbon nanotubes: growth, structure and electronic properties. In: Marulanda JM, editor. Electronic properties of carbon nanotubes. Rijeka, Croatia: InTech; 2011. p. 127–56.

[54] Eliseev AA, Kharlamova MV, Chernysheva MV, Lukashin AV, Tretyakov YD, Kumskov AS, et al. Preparation and properties of single-walled nanotubes filled with inorganic compounds. Russ Chem Rev 2009;78:833–54.
[55] Monthioux M. Filling single-wall carbon nanotubes. Carbon 2002;40:1809–23.
[56] Monthioux M, Flahaut E, Cleuziou JP. Hybrid carbon nanotubes: strategy, progress, and perspectives. J Mater Res 2006;21:2774–93.
[57] Sloan J, Monthioux M. Filled carbon nanotubes: (X@CNTs). In: Monthioux M, editor. Carbon meta-nanotubes: synthesis, properties, and applications. Chichester: John Wiley & Sons Ltd.; 2012. p. 225–71.
[58] Kramberger C, Rauf H, Knupfer M, Shiozawa H, Batchelor D, Rubio A, et al. Potassium-intercalated single-wall carbon nanotube bundles: archetypes for semiconductor/metal hybrid systems. Phys Rev B 2009;79:195442.
[59] Kittel C. Introduction to solid state physics. Moscow: Nauka; 1978 [Russian translation from Kittel C. Introduction to solid state physics. 4th ed. New York: Wiley; 1971].
[60] Pavlov PV, Khokhlov AF. Solid state physics. 3rd ed. Moscow: Vysshaya shkola; 2000 [in Russian].
[61] Shalimova KV. Physics of semiconductors. 3rd ed. Moscow: Energoatomizdat; 1985 [in Russian].
[62] Ashcroft N, Mermin N. Solid state physics. Moscow: Mir; 1979 [Russian translation from Ashcroft NW, Mermin ND. Solid state physics. 1st ed. Orlando: Harcourt College Publishers; 1976].
[63] Charlier JC, Blase X, Roche S. Electronic and transport properties of nanotubes. Rev Mod Phys 2007;79:677–732.
[64] Kreupl F. Carbon nanotubes in microelectronics applications. In: Hierold C, editor. Advanced micro and nanosystems, vol. 8. Weinheim: Wiley-VCH; 2008. p. 1–41.
[65] Hamada N, Sawada S, Oshiyama A. New one-dimensional conductors – graphitic microtubules. Phys Rev Lett 1992;68:1579–81.
[66] Mintmire JW, Dunlap BI, White CT. Are fullerene tubules metallic. Phys Rev Lett 1992;68:631–4.
[67] Saito R, Fujita M, Dresselhaus G, Dresselhaus MS. Electronic structure of chiral graphene tubules. Appl Phys Lett 1992;60:2204–6.
[68] Saito R, Kataura H. Optical properties and Raman spectroscopy of carbon nanotubes. In: Dresselhaus MS, Dresselhaus G, Avouris A, editors. Topics in applied physics, vol. 80. Berlin: Springer; 2001. p. 213–46.
[69] Saito R, Dresselhaus G, Dresselhaus MS. Trigonal warping effect of carbon nanotubes. Phys Rev B 2000;61:2981–90.
[70] Castro Neto AH, Guinea F, Peres NMR, Novoselov KS, Geim AK. The electronic properties of graphene. Rev Mod Phys 2009;81:109–62.
[71] Painter GS, Ellis DE. Electronic band structure and optical properties of graphite from a variational approach. Phys Rev B 1970;1:4747–52.
[72] Reich S, Maultzsch J, Thomsen C, Ordejon P. Tight-binding description of graphene. Phys Rev B 2002;66:035412.
[73] Chico L, Crespi VH, Benedict LX, Louie SG, Cohen ML. Pure carbon nanoscale devices: nanotube heterojunctions. Phys Rev Lett 1996;76:971–4.
[74] Dresselhaus MS, Dresselhaus G, Charlier JC, Hernandez E. Electronic, thermal and mechanical properties of carbon nanotubes. Philos Trans R Soc Lond A 2004;362:2065–98.
[75] Kataura H, Kumazawa Y, Maniwa Y, Umezu I, Suzuki S, Ohtsuka Y, et al. Optical properties of single-wall carbon nanotubes. Synthet Met 1999;103:2555–8.
[76] Odom TW, Huang JL, Kim P, Lieber CM. Atomic structure and electronic properties of single-walled carbon nanotubes. Nature 1998;391:62–4.
[77] Pichler T, Knupfer M, Golden MS, Fink J, Rinzler A, Smalley RE. Localized and delocalized electronic states in single-wall carbon nanotubes. Phys Rev Lett 1998;80:4729–32.
[78] Bachilo SM, Strano MS, Kittrell C, Hauge RH, Smalley RE, Weisman RB. Structure-assigned optical spectra of single-walled carbon nanotubes. Science 2002;298:2361–6.
[79] Kramberger C, Rauf H, Shiozawa H, Knupfer M, Buchner B, Pichler T, et al. Unraveling van Hove singularities in X-ray absorption response of single-wall carbon nanotubes. Phys Rev B 2007;75:235437.
[80] Ishii H, Kataura H, Shiozawa H, Yoshioka H, Otsubo H, Takayama Y, et al. Direct observation of Tomonaga–Luttinger-liquid state in carbon nanotubes at low temperatures. Nature 2003;426:540–4.
[81] Yi JY, Bernholc J. Atomic-structure and doping of microtubules. Phys Rev B 1993;47:1708–11.
[82] Bethune DS, Klang CH, de Vries MS, Gorman G, Savoy R, Vazquez J, et al. Cobalt-catalysed growth of carbon nanotubes with single-atomic-layer walls. Nature 1993;363:605–7.
[83] Ayala P, Grueneis A, Gemming T, Grimm D, Kramberger C, Ruemmeli MH, et al. Tailoring N-doped single and double wall carbon nanotubes from a nondiluted carbon/nitrogen feedstock. J Phys Chem C 2007;111:2879–84.
[84] Elias AL, Ayala P, Zamudio A, Grobosch M, Cruz-Silva E, Romo-Herrera JM, et al. Spectroscopic characterization of N-doped single-walled carbon nanotube strands: an X-ray photoelectron spectroscopy and Raman study. J Nanosci Nanotechnol 2010;10:3959–64.
[85] Glerup M, Steinmetz J, Samaille D, Stephan O, Enouz S, Loiseau A, et al. Synthesis of N-doped SWNT using the arc-discharge procedure. Chem Phys Lett 2004;387:193–7.
[86] Keskar G, Rao R, Luo J, Hudson J, Chen J, Rao AM. Growth, nitrogen doping and characterization of isolated single-wall carbon nanotubes using liquid precursors. Chem Phys Lett 2005;412:269–73.
[87] Krstic V, Rikken GLJA, Bernier P, Roth S, Glerup M. Nitrogen doping of metallic single-walled carbon nanotubes: n-type conduction and dipole scattering. Europhys Lett 2007;77:37001.
[88] Lin H, Lagoute J, Chacon C, Arenal R, Stephan O, Repain V, et al. Combined STM/STS, TEM/EELS investigation of $CN_x$-SWNTs. Phys Status Solidi B 2008;245:1986–9.
[89] Lin H, Arenal R, Enouz-Vedrenne S, Stephan O, Loiseau A. Nitrogen configuration in individual $CN_x$-SWNTs synthesized by laser vaporization technique. J Phys Chem C 2009;113:9509–11.
[90] Maciel IO, Anderson N, Pimenta MA, Hartschuh A, Qian HH, Terrones M, et al. Electron and phonon renormalization near charged defects in carbon nanotubes. Nat Mater 2008;7:878–83.
[91] Susi T, Zhu Z, Ruiz-Soria G, Arenal R, Ayala P, Nasibulin AG, et al. Nitrogen-doped SWCNT synthesis using ammonia and carbon monoxide. Phys Status Solidi B 2010;247:2726–9.

[92] Villalpando-Paez F, Zamudio A, Elias AL, Son H, Barros EB, Chou SG, et al. Synthesis and characterization of long strands of nitrogen-doped single-walled carbon nanotubes. Chem Phys Lett 2006;424:345–52.
[93] Wiltshire JG, Li LJ, Herz LM, Nicholas RJ, Glerup M, Sauvajol JL, et al. Chirality-dependent boron-mediated growth of nitrogen-doped single-walled carbon nanotubes. Phys Rev B 2005;72:205431.
[94] Ayala P, Plank W, Gruneis A, Kauppinen EI, Rummeli MH, Kuzmany H, et al. A one step approach to B-doped single-walled carbon nanotubes. J Mater Chem 2008;18:5676–81.
[95] Ayala P, Reppert J, Grobosch M, Knupfer M, Pichler T, Rao AM. Evidence for substitutional boron in doped single-walled carbon nanotubes. Appl Phys Lett 2010;96:183110.
[96] Borowiak-Palen E, Pichler T, Fuentes GG, Graff A, Kalenczuk RJ, Knupfer M, et al. Efficient production of B-substituted single-wall carbon nanotubes. Chem Phys Lett 2003;378:516–20.
[97] Borowiak-Palen E, Pichler T, Graff A, Kalenezuk RJ, Knupfer M, Fink J. Synthesis and electronic properties of B-doped single wall carbon nanotubes. Carbon 2004;42:1123–6.
[98] Daothong S, Parjanne J, Kauppinen EI, Valkeapaa M, Pichler T, Singjai P, et al. Study of the role of Fe based catalysts on the growth of B-doped SWCNTs synthesized by CVD. Phys Status Solidi B 2009;246:2518–22.
[99] Fuentes GG, Borowiak-Palen E, Knupfer M, Pichler T, Fink J, Wirtz L, et al. Formation and electronic properties of $BC_3$ single-wall nanotubes upon boron substitution of carbon nanotubes. Phys Rev B 2004;69:245403.
[100] Gai PL, Stephan O, McGuire K, Rao AM, Dresselhaus MS, Dresselhaus G, et al. Structural systematics in boron-doped single wall carbon nanotubes. J Mater Chem 2004;14:669–75.
[101] McGuire K, Gothard N, Gai PL, Dresselhaus MS, Sumanasekera G, Rao AM. Synthesis and Raman characterization of boron-doped single-walled carbon nanotubes. Carbon 2005;43:219–27.
[102] Ayala P, Arenal R, Loiseau A, Rubio A, Pichler T. The physical and chemical properties of heteronanotubes. Rev Mod Phys 2010;82:1843–85.
[103] Ayala P, Arenal R, Rummeli M, Rubio A, Pichler T. The doping of carbon nanotubes with nitrogen and their potential applications. Carbon 2010;48:575–86.
[104] Kang HS, Jeong S. Nitrogen doping and chirality of carbon nanotubes. Phys Rev B 2004;70:233411.
[105] Nevidomskyy AH, Csanyi G, Payne MC. Chemically active substitutional nitrogen impurity in carbon nanotubes. Phys Rev Lett 2003;91:105502.
[106] Terrones M, Souza AG, Rao AM. Doped carbon nanotubes: synthesis, characterization and applications. In: Jorio A, Dresselhaus G, Dresselhaus MS, editors. Topics in applied physics, vol. 111. Berlin: Springer; 2008. p. 531–66.
[107] Czerw R, Terrones M, Charlier JC, Blase X, Foley B, Kamalakaran R, et al. Identification of electron donor states in N-doped carbon nanotubes. Nano Lett 2001;1:457–60.
[108] Rocha AR, Padilha JE, Fazzio A, da Silva AJR. Transport properties of single vacancies in nanotubes. Phys Rev B 2008;77:153406.
[109] Wirtz L, Rubio A. Band structure of boron doped carbon nanotubes. AIP Conf Proc 2003;685:402–5.
[110] Tasis D, Tagmatarchis N, Bianco A, Prato M. Chemistry of carbon nanotubes. Chem Rev 2006;106:1105–36.
[111] Andrews R, Jacques D, Qian DL, Rantell T. Multiwall carbon nanotubes: synthesis and application. Acc Chem Res 2002;35:1008–17.
[112] Bahr JL, Tour JM. Covalent chemistry of single-wall carbon nanotubes. J Mater Chem 2002;12:1952–8.
[113] Balasubramanian K, Burghard M. Chemically functionalized carbon nanotubes. Small 2005;1:180–92.
[114] Banerjee S, Kahn MGC, Wong SS. Rational chemical strategies for carbon nanotube functionalization. Chem A: Eur J 2003;9:1899–908.
[115] Banerjee S, Hemraj-Benny T, Wong SS. Covalent surface chemistry of single-walled carbon nanotubes. Adv Mater 2005;17:17–29.
[116] Dai LM, Mau AWH. Controlled synthesis and modification of carbon nanotubes and $C_{60}$: carbon nanostructures for advanced polymer composite materials. Adv Mater 2001;13:899–913.
[117] Davis JJ, Coleman KS, Azamian BR, Bagshaw CB, Green MLH. Chemical and biochemical sensing with modified single walled carbon nanotubes. Chem A: Eur J 2003;9:3732–9.
[118] de la Torre G, Blau W, Torres T. A survey on the functionalization of single-walled nanotubes. The chemical attachment of phthalocyanine moieties. Nanotechnology 2003;14:765–71.
[119] Dyke CA, Tour JM. Covalent functionalization of single-walled carbon nanotubes for materials applications. J Phys Chem A 2004;108:11151–9.
[120] Dyke CA, Tour JM. Overcoming the insolubility of carbon nanotubes through high degrees of sidewall functionalization. Chem A: Eur J 2004;10:812–7.
[121] Fischer JE. Chemical doping of single-wall carbon nanotubes. Acc Chem Res 2002;35:1079–86.
[122] Fu KF, Sun YP. Dispersion and solubilization of carbon nanotubes. J Nanosci Nanotechnol 2003;3:351–64.
[123] Hilding J, Grulke EA, Zhang ZG, Lockwood F. Dispersion of carbon nanotubes in liquids. J Dispers Sci Technol 2003;24:1–41.
[124] Hirsch A. Functionalization of single-walled carbon nanotubes. Angew Chem Int Ed 2002;41:1853–9.
[125] Hirsch A, Vostrowsky O. Functionalization of carbon nanotubes. In: Schluter AD, editor. Topics in current chemistry, vol. 245. Berlin: Springer; 2005. p. 193.
[126] Katz E, Willner I. Biomolecule-functionalized carbon nanotubes: applications in nanobioelectronics. ChemPhysChem 2004;5:1085–104.
[127] Lin T, Bajpai V, Ji T, Dai LM. Chemistry of carbon nanotubes. Aust J Chem 2003;56:635–51.
[128] Lu X, Chen ZF. Curved Pi-conjugation, aromaticity, and the related chemistry of small fullerenes ($<C_{60}$) and single-walled carbon nanotubes. Chem Rev 2005;105:3643–96.
[129] Niyogi S, Hamon MA, Hu H, Zhao B, Bhowmik P, Sen R, et al. Chemistry of single-walled carbon nanotubes. Acc Chem Res 2002;35:1105–13.
[130] Rao CNR, Satishkumar BC, Govindaraj A, Nath M. Nanotubes. ChemPhysChem 2001;2:78–105.
[131] Sinnott SB. Chemical functionalization of carbon nanotubes. J Nanosci Nanotechnol 2002;2:113–23.

[132] Sun YP, Fu KF, Lin Y, Huang WJ. Functionalized carbon nanotubes: properties and applications. Acc Chem Res 2002;35:1096–104.
[133] Tasis D, Tagmatarchis N, Georgakilas V, Prato M. Soluble carbon nanotubes. Chem A: Eur J 2003;9:4001–8.
[134] Terrones M. Science and technology of the twenty-first century: synthesis, properties and applications of carbon nanotubes. Annu Rev Mater Res 2003;33:419–501.
[135] Thostenson ET, Ren ZF, Chou TW. Advances in the science and technology of carbon nanotubes and their composites: a review. Compos Sci Technol 2001;61:1899–912.
[136] Hamwi A, Alvergnat H, Bonnamy S, Beguin F. Fluorination of carbon nanotubes. Carbon 1997;35:723–8.
[137] Kawasaki S, Komatsu K, Okino F, Touhara H, Kataura H. Fluorination of open- and closed-end single-walled carbon nanotubes. Phys Chem Chem Phys 2004;6:1769–72.
[138] Mickelson ET, Huffman CB, Rinzler AG, Smalley RE, Hauge RH, Margrave JL. Fluorination of single-wall carbon nanotubes. Chem Phys Lett 1998;296:188–94.
[139] Nakajima T, Kasamatsu S, Matsuo Y. Synthesis and characterization of fluorinated carbon nanotube. Eur J Solid State Inorg Chem 1996;33:831–40.
[140] Touhara H, Okino F. Property control of carbon materials by fluorination. Carbon 2000;38:241–67.
[141] Touhara H, Inahara J, Mizuno T, Yokoyama Y, Okanao S, Yanagiuch K, et al. Property control of new forms of carbon materials by fluorination. J Fluorine Chem 2002;114:181–8.
[142] Yudanov NF, Okotrub AV, Shubin YV, Yudanova LI, Bulusheva LG, Chuvilin AL, et al. Fluorination of arc-produced carbon material containing multiwall nanotubes. Chem Mater 2002;14:1472–6.
[143] Pehrsson PE, Zhao W, Baldwin JW, Song CH, Liu J, Kooi S, et al. Thermal fluorination and annealing of single-wall carbon nanotubes. J Phys Chem B 2003;107:5690–5.
[144] Zhao W, Song CH, Zheng B, Liu J, Viswanathan T. Thermal recovery behavior of fluorinated single-walled carbon nanotubes. J Phys Chem B 2002;106:293–6.
[145] An KH, Heo JG, Jeon KG, Bae D, Jo CS, Yang CW, et al. X-ray photoemission spectroscopy study of fluorinated single-walled carbon nanotubes. Appl Phys Lett 2002;80:4235–7.
[146] Brzhezinskaya MM, Vinogradov AS, Krestinin AV, Zvereva GI, Kharitonov AP. Electronic structure of fluorinated single-walled carbon nanotubes studied by X-ray absorption and photoelectron spectroscopy. Fullerenes, Nanotubes, Carbon Nanostruct 2010;18:590–4.
[147] Lee YS, Cho TH, Lee BK, Rho JS, An KH, Lee YH. Surface properties of fluorinated single-walled carbon nanotubes. J Fluorine Chem 2003;120:99–104.
[148] Plank NOV, Jiang LD, Cheung R. Fluorination of carbon nanotubes in $CF_4$ plasma. Appl Phys Lett 2003;83:2426–8.
[149] Plank NOV, Cheung R. Functionalisation of carbon nanotubes for molecular electronics. Microelectron Eng 2004;73–4:578–82.
[150] Fedoseeva YV, Bulusheva LG, Okotrub AV, Vyalikh DV, Fonseca A. XANES investigation of pristine and fluorinated single-walled carbon nanotubes before and after annealing. Fullerenes, Nanotubes, Carbon Nanostruct 2010;18:595–9.
[151] Kelly KF, Chiang IW, Mickelson ET, Hauge RH, Margrave JL, Wang X, et al. Insight into the mechanism of sidewall functionalization of single-walled nanotubes: an STM study. Chem Phys Lett 1999;313:445–50.
[152] Bettinger HF, Kudin KN, Scuseria GE. Thermochemistry of fluorinated single wall carbon nanotubes. J Am Chem Soc 2001;123:12849–56.
[153] Bettinger HF. Experimental and computational investigations of the properties of fluorinated single-walled carbon nanotubes. ChemPhysChem 2003;4:1283–9.
[154] Bettinger HF. Effects of finite carbon nanotube length on sidewall addition of fluorine atom and methylene. Org Lett 2004;6:731–4.
[155] Jaffe RL. Quantum chemistry study of fullerene and carbon nanotube fluorination. J Phys Chem B 2003;107:10378–88.
[156] Kudin KN, Bettinger HF, Scuseria GE. Fluorinated single-wall carbon nanotubes. Phys Rev B 2001;63:045413.
[157] Lebedev NG, Zaporotskova IV, Chernozatonskii LA. Fluorination of carbon nanotubes within the molecular cluster method. Microelectron Eng 2003;69:511–8.
[158] Root MJ. Comparison of fluorofullerenes with carbon monofluorides and fluorinated carbon single wall nanotubes: thermodynamics and electrochemistry. Nano Lett 2002;2:541–3.
[159] Van Lier G, Ewels CP, Zuliani F, De Vita A, Charlier JC. Theoretical analysis of fluorine addition to single-walled carbon nanotubes: functionalization routes and addition patterns. J Phys Chem B 2005;109:6153–8.
[160] Coleman KS, Chakraborty AK, Bailey SR, Sloan J, Alexander M. Iodination of single-walled carbon nanotubes. Chem Mater 2007;19:1076–81.
[161] Alvaro M, Atienzar P, de la Cruz P, Delgado JL, Garcia H, Langa F. Sidewall functionalization of single-walled carbon nanotubes with nitrile imines. Electron transfer from the substituent to the carbon nanotube. J Phys Chem B 2004;108:12691–7.
[162] Callegari A, Marcaccio M, Paolucci D, Paolucci F, Tagmatarchis N, Tasis D, et al. Anion recognition by functionalized single wall carbon nanotubes. Chem Commun 2003:2576–7.
[163] Chen J, Hamon MA, Hu H, Chen YS, Rao AM, Eklund PC, et al. Solution properties of single-walled carbon nanotubes. Science 1998;282:95–8.
[164] Georgakilas V, Kordatos K, Prato M, Guldi DM, Holzinger M, Hirsch A. Organic functionalization of carbon nanotubes. J Am Chem Soc 2002;124:760–1.
[165] Guldi DM, Marcaccio M, Paolucci D, Paolucci F, Tagmatarchis N, Tasis D, et al. Single-wall carbon nanotube-ferrocene nanohybrids: observing intramolecular electron transfer in functionalized SWNTs. Angew Chem Int Ed 2003;42:4206–9.
[166] Wang YB, Iqbal Z, Mitra S. Microwave-induced rapid chemical functionalization of single-walled carbon nanotubes. Carbon 2005;43:1015–20.
[167] Islam MF, Rojas E, Bergey DM, Johnson AT, Yodh AG. High weight fraction surfactant solubilization of single-wall carbon nanotubes in water. Nano Lett 2003;3:269–73.
[168] Matarredona O, Rhoads H, Li ZR, Harwell JH, Balzano L, Resasco DE. Dispersion of single-walled carbon nanotubes in aqueous solutions of the anionic surfactant NaDDBS. J Phys Chem B 2003;107:13357–67.

[169] Moore VC, Strano MS, Haroz EH, Hauge RH, Smalley RE, Schmidt J, et al. Individually suspended single-walled carbon nanotubes in various surfactants. Nano Lett 2003;3:1379–82.
[170] Fernando KAS, Lin Y, Wang W, Kumar S, Zhou B, Xie SY, et al. Diminished band-gap transitions of single-walled carbon nanotubes in complexation with aromatic molecules. J Am Chem Soc 2004;126:10234–5.
[171] Fifield LS, Dalton LR, Addleman RS, Galhotra RA, Engelhard MH, Fryxell GE, et al. Noncovalent functionalization of carbon nanotubes with molecular anchors using supercritical fluids. J Phys Chem B 2004;108:8737–41.
[172] Nakashima N, Tomonari Y, Murakami H. Water-soluble single-walled carbon nanotubes via noncovalent sidewall-functionalization with a pyrene-carrying ammonium ion. Chem Lett 2002;31:638–9.
[173] Paloniemi H, Aaritalo T, Laiho T, Liuke H, Kocharova N, Haapakka K, et al. Water-soluble full-length single-wall carbon nanotube polyelectrolytes: preparation and characterization. J Phys Chem B 2005;109:8634–42.
[174] Zhang J, Lee JK, Wu Y, Murray RW. Photoluminescence and electronic interaction of anthracene derivatives adsorbed on sidewalls of single-walled carbon nanotubes. Nano Lett 2003;3:403–7.
[175] Collins PG, Bradley K, Ishigami M, Zettl A. Extreme oxygen sensitivity of electronic properties of carbon nanotubes. Science 2000;287:1801–4.
[176] Kong J, Franklin NR, Zhou CW, Chapline MG, Peng S, Cho KJ, et al. Nanotube molecular wires as chemical sensors. Science 2000;287:622–5.
[177] Geng HZ, Kim KK, So KP, Lee YS, Chang Y, Lee YH. Effect of acid treatment on carbon nanotube-based flexible transparent conducting films. J Am Chem Soc 2007;129:7758–9.
[178] Kim KK, Yoon SM, Choi JY, Lee J, Kim BK, Kim JM, et al. Design of dispersants for the dispersion of carbon nanotubes in an organic solvent. Adv Funct Mater 2007;17:1775–83.
[179] Shin HJ, Kim SM, Yoon SM, Benayad A, Kim KK, Kim SJ, et al. Tailoring electronic structures of carbon nanotubes by solvent with electron-donating and -withdrawing groups. J Am Chem Soc 2008;130:2062–6.
[180] Lee RS, Kim HJ, Fischer JE, Thess A, Smalley RE. Conductivity enhancement in single-walled carbon nanotube bundles doped with K and Br. Nature 1997;388:255–7.
[181] Rao AM, Eklund PC, Bandow S, Thess A, Smalley RE. Evidence for charge transfer in doped carbon nanotube bundles from Raman scattering. Nature 1997;388:257–9.
[182] Bandow S, Rao AM, Sumanasekera GU, Eklund PC, Kokai F, Takahashi K, et al. Evidence for anomalously small charge transfer in doped single-wall carbon nanohorn aggregates with Li, K and Br. Appl Phys A 2000;71:561–4.
[183] Baxendale M, Mordkovich VZ, Yoshimura S, Chang RPH. Magnetotransport in bundles of intercalated carbon nanotubes. Phys Rev B 1997;56:2161–5.
[184] Bockrath M, Hone J, Zettl A, Mceuen PL, Rinzler AG, Smalley RE. Chemical doping of individual semiconducting carbon-nanotube ropes. Phys Rev B 2000;61:10606–8.
[185] Bower C, Suzuki S, Tanigaki K, Zhou O. Synthesis and structure of pristine and alkali-metal-intercalated single-walled carbon nanotubes. Appl Phys A 1998;67:47–52.
[186] Claye A, Fischer JE. Electrochemical doping of single wall carbon nanotubes with lithium. Mol Cryst Liq Cryst 2000;340:743–8.
[187] Duclaux L, Metenier K, Salvetat JP, Lauginie P, Bonnamy S, Beguin F. Doping of carbon nanotubes by heavy alkali metals. Mol Cryst Liq Cryst 2000;340:769–74.
[188] Duclaux L. Review of the doping of carbon nanotubes (multiwalled and single-walled). Carbon 2002;40:1751–64.
[189] Duclaux L, Salvetat JP, Lauginie P, Cacciaguera T, Faugere AM, Goze-Bac C, et al. Synthesis and characterization of SWNT-heavy alkali metal intercalation compounds, effect of host SWNTs materials. J Phys Chem Solids 2003;64:571–81.
[190] Galambos M, Fabian G, Simon F, Ciric L, Forro L, Korecz L, et al. Identifying the electron spin resonance of conduction electrons in alkali doped SWCNTs. Phys Status Solidi B 2009;246:2760–3.
[191] Jouguelet E, Mathis C, Petit P. Controlling the electronic properties of single-wall carbon nanotubes by chemical doping. Chem Phys Lett 2000;318:561–4.
[192] Kramberger C, Rauf H, Knupfer M, Shiozawa H, Batchelor D, Kataura H, et al. Electronic and optical properties of alkali metal doped carbon nanotubes. Phys Status Solidi B 2009;246:2693–8.
[193] Kukovecz A, Pichler T, Pfeiffer R, Kramberger C, Kuzmany H. Diameter selective doping of single wall carbon nanotubes. Phys Chem Chem Phys 2003;5:582–7.
[194] Lee RS, Kim HJ, Fischer JE, Lefebvre J, Radosavljevic M, Hone J, et al. Transport properties of a potassium-doped single-wall carbon nanotube rope. Phys Rev B 2000;61:4526–9.
[195] Liu X, Pichler T, Knupfer M, Fink J. Electronic and optical properties of alkali-metal-intercalated single-wall carbon nanotubes. Phys Rev B 2003;67:125403.
[196] Liu X, Pichler T, Knupfer M, Fink J. Electronic properties of barium-intercalated single-wall carbon nanotubes. Phys Rev B 2004;70:245435.
[197] Petit P, Mathis C, Journet C, Bernier P. Tuning and monitoring the electronic structure of carbon nanotubes. Chem Phys Lett 1999;305:370–4.
[198] Pichler T, Sing M, Knupfer M, Golden MS, Fink J. Potassium intercalated bundles of single-wall carbon nanotubes: electronic structure and optical properties. Solid State Commun 1999;109:721–6.
[199] Pichler T, Kukovecz A, Kuzmany H, Kataura H. Charge transfer in doped single wall carbon nanotubes. Synthet Met 2003;135:717–9.
[200] Pichler T, Liu X, Knupfer M, Fink J. Electronic properties of intercalated single-wall carbon nanotubes and $C_{60}$ peapods. New J Phys 2003;5:156.
[201] Pichler T, Rauf H, Knupfer M, Fink J, Kataura H. A photoemission study of the nature of the metallic state in single wall carbon nanotube bundles at low potassium doping. Synthet Met 2005;153:333–6.
[202] Rauf H, Pichler T, Knupfer M, Fink J, Kataura H. Transition from a Tomonaga–Luttinger liquid to a Fermi liquid in potassium-intercalated bundles of single-wall carbon nanotubes. Phys Rev Lett 2004;93:096805.
[203] Shimoda H, Gao B, Tang XP, Kleinhammes A, Fleming L, Wu Y, et al. Lithium intercalation into opened single-wall carbon nanotubes: storage capacity and electronic properties. Phys Rev Lett 2002;88:015502.

[204] Simon F, Galambos M, Quintavalle D, Nafradi B, Forro L, Koltai J, et al. Electron spin resonance in alkali doped SWCNTs. Phys Status Solidi B 2008;245:1975–8.
[205] Suzuki S, Bower C, Zhou O. In-situ TEM and EELS studies of alkali-metal intercalation with single-walled carbon nanotubes. Chem Phys Lett 1998;285:230–4.
[206] Suzuki S, Bower C, Watanabe Y, Zhou O. Work functions and valence band states of pristine and Cs-intercalated single-walled carbon nanotube bundles. Appl Phys Lett 2000;76:4007–9.
[207] Suzuki S, Maeda F, Watanabe Y, Ogino T. Electronic structure of single-walled carbon nanotubes encapsulating potassium. Phys Rev B 2003;67:115418.
[208] Bower C, Kleinhammes A, Wu Y, Zhou O. Intercalation and partial exfoliation of single-walled carbon nanotubes by nitric acid. Chem Phys Lett 1998;288:481–6.
[209] De Blauwe K, Kramberger C, Plank W, Kataura H, Pichler T. Raman response of $FeCl_3$ intercalated single-wall carbon nanotubes at high doping. Phys Status Solidi B 2009;246:2732–6.
[210] Graupner R, Abraham J, Vencelova A, Seyller T, Hennrich F, Kappes MM, et al. Doping of single-walled carbon nanotube bundles by Bronsted acids. Phys Chem Chem Phys 2003;5:5472–6.
[211] Grigorian L, Williams KA, Fang S, Sumanasekera GU, Loper AL, Dickey EC, et al. Reversible intercalation of charged iodine chains into carbon nanotube ropes. Phys Rev Lett 1998;80:5560–3.
[212] Hennrich F, Wellmann R, Malik S, Lebedkin S, Kappes MM. Reversible modification of the absorption properties of single-walled carbon nanotube thin films via nitric acid exposure. Phys Chem Chem Phys 2003;5:178–83.
[213] Kazaoui S, Minami N, Jacquemin R, Kataura H, Achiba Y. Amphoteric doping of single-wall carbon-nanotube thin films as probed by optical absorption spectroscopy. Phys Rev B 1999;60:13339–42.
[214] Kim KK, Bae JJ, Park HK, Kim SM, Geng HZ, Park KA, et al. Fermi level engineering of single-walled carbon nanotubes by $AuCl_3$ doping. J Am Chem Soc 2008;130:12757–61.
[215] Lee I, Kim UJ, Bin Son H, Yoon SM, Yao F, Yu WJ, et al. Hygroscopic effects on $AuCl_3$-doped carbon nanotubes. J Phys Chem C 2010;114:11618–22.
[216] Liu X, Pichler T, Knupfer M, Fink J, Kataura H. Electronic properties of $FeCl_3$-intercalated single-wall carbon nanotubes. Phys Rev B 2004;70:205405.
[217] Sumanasekera GU, Allen JL, Fang SL, Loper AL, Rao AM, Eklund PC. Electrochemical oxidation of single wall carbon nanotube bundles in sulfuric acid. J Phys Chem B 1999;103:4292–7.
[218] Yoon SM, Kim UJ, Benayad A, Lee IH, Son H, Shin HJ, et al. Thermal conversion of electronic and electrical properties of $AuCl_3$-doped single-walled carbon nanotubes. ACS Nano 2011;5:1353–9.
[219] Yu ZH, Brus LE. Reversible oxidation effect in Raman scattering from metallic single-wall carbon nanotubes. J Phys Chem A 2000;104:10995–9.
[220] Dresselhaus MS, Dresselhaus G. Intercalation compounds of graphite. Adv Phys 1981;30:139–326.
[221] Fischer JE, Bloch JM, Shieh CC, Preil ME, Jelley K. Reflectivity spectra and dielectric function of stage-1 donor intercalation compounds of graphite. Phys Rev B 1985;31:4773–83.
[222] Zhou O, Fischer JE, Coustel N, Kycia S, Zhu Q, Mcghie AR, et al. Structure and bonding in alkali-metal-doped $C_{60}$. Nature 1991;351:462–4.
[223] Pichler T. Electron energy-loss studies of pristine and doped nanotubes. New Diamond Front Carbon Technol 2001;11:375–97.
[224] Ruzicka B, Degiorgi L, Gaal R, Thien-Nga L, Bacsa R, Salvetat JP, et al. Optical and dc conductivity study of potassium-doped single-walled carbon nanotube films. Phys Rev B 2000;61:R2468–71.
[225] Bendiab N, Anglaret E, Bantignies JL, Zahab A, Sauvajol JL, Petit P, et al. Stoichiometry dependence of the Raman spectrum of alkali-doped single-wall carbon nanotubes. Phys Rev B 2001;64:245424.
[226] Iwasa Y, Fudo H, Yatsu Y, Mitani T, Kataura H, Achiba Y. Phase stability of doped carbon nanotubes. Synthet Met 2001;121:1203–4.
[227] Kukovecz A, Pichler T, Pfeiffer R, Kuzmany H. Diameter selective charge transfer in p- and n-doped single wall carbon nanotubes synthesized by the HiPCO method. Chem Commun 2002:1730–1.
[228] Rao AM, Bandow S, Richter E, Eklund PC. Raman spectroscopy of pristine and doped single wall carbon nanotubes. Thin Solid Films 1998;331:141–7.
[229] Jacquemin R, Kazaoui S, Yu D, Hassanien A, Minami N, Kataura H, et al. Doping mechanism in single-wall carbon nanotubes studied by optical absorption. Synthet Met 2000;115:283–7.
[230] Bandow S, Yudasaka M, Yamada R, Iijma S, Kokai F, Takahashi K. Electron spin resonance of K-doped single-wall carbon nanohorns and single-wall carbon nanotubes. Mol Cryst Liq Cryst 2000;340:749–56.
[231] Claye AS, Nemes NM, Janossy A, Fischer JE. Structure and electronic properties of potassium-doped single-wall carbon nanotubes. Phys Rev B 2000;62:R4845–8.
[232] Grigorian L, Sumanasekera GU, Loper AL, Fang S, Allen JL, Eklund PC. Transport properties of alkali-metal-doped single-wall carbon nanotubes. Phys Rev B 1998;58:R4195–8.
[233] Itkis ME, Niyogi S, Meng ME, Hamon MA, Hu H, Haddon RC. Spectroscopic study of the Fermi level electronic structure of single-walled carbon nanotubes. Nano Lett 2002;2:155–9.
[234] Zhang Y, Iijima S, Shi Z, Gu Z. Defects in arc-discharge-produced single-walled carbon nanotubes. Philos Mag Lett 1999;79:473–9.
[235] Burteaux B, Claye A, Smith BW, Monthioux M, Luzzi DE, Fischer JE. Abundance of encapsulated $C_{60}$ in single-wall carbon nanotubes. Chem Phys Lett 1999;310:21–4.
[236] Kataura H, Maniwa Y, Kodama T, Kikuchi K, Hirahara K, Suenaga K, et al. High-yield fullerene encapsulation in single-wall carbon nanotubes. Synthet Met 2001;121:1195–6.
[237] Khlobystov AN, Porfyrakis K, Kanai M, Britz DA, Ardavan A, Shinohara H, et al. Molecular motion of endohedral fullerenes in single-walled carbon nanotubes. Angew Chem Int Ed 2004;43:1386–9.
[238] Khlobystov AN, Britz DA, Briggs GAD. Molecules in carbon nanotubes. Acc Chem Res 2005;38:901–9.
[239] Shimada T, Ohno Y, Okazaki T, Sugai T, Suenaga K, Kishimoto S, et al. Transport properties of $C_{78}$, $C_{90}$ and $Dy@C_{82}$ fullerenes-nanopeapods by field effect transistors. Physica E 2004;21:1089–92.

[240] Shiozawa H, Ishii H, Kihara H, Sasaki N, Nakamura S, Yoshida T, et al. Photoemission and inverse photoemission study of the electronic structure of $C_{60}$ fullerenes encapsulated in single-walled carbon nanotubes. Phys Rev B 2006;73:075406.
[241] Simon F, Kuzmany H, Rauf H, Pichler T, Bernardi J, Peterlik H, et al. Low temperature fullerene encapsulation in single wall carbon nanotubes: synthesis of N@$C_{60}$@SWCNT. Chem Phys Lett 2004;383:362–7.
[242] Pagona G, Rotas G, Khlobystov AN, Chamberlain TW, Porfyrakis K, Tagmatarchis N. Azafullerenes encapsulated within single-walled carbon nanotubes. J Am Chem Soc 2008;130:6062–3.
[243] Kalbac M, Kavan L, Zukalova M, Dunsch L. Two positions of potassium in chemically doped $C_{60}$ peapods: an in situ spectroelectrochemical study. J Phys Chem B 2004;108:6275–80.
[244] Pichler T, Kuzmany H, Kataura H, Achiba Y. Metallic polymers of $C_{60}$ inside single-walled carbon nanotubes. Phys Rev Lett 2001;87:267401.
[245] Pichler T, Kukovecz A, Kuzmany H, Kataura H, Achiba Y. Quasicontinuous electron and hole doping of $C_{60}$ peapods. Phys Rev B 2003;67:125416.
[246] Ashino M, Obergfell D, Haluska M, Yang SH, Khlobystov AN, Roth S, et al. Atomically resolved mechanical response of individual metallofullerene molecules confined inside carbon nanotubes. Nat Nanotechnol 2008;3:337–41.
[247] Chiu PW, Gu G, Kim GT, Philipp G, Roth S, Yang SF, et al. Temperature-induced change from p to n conduction in metallofullerene nanotube peapods. Appl Phys Lett 2001;79:3845–7.
[248] Debarre A, Jaffiol R, Julien C, Richard A, Nutarelli D, Tchenio P. Antenna effect in dimetallofullerene peapods. Chem Phys Lett 2003;380:6–11.
[249] Gloter A, Suenaga K, Kataura H, Fujii R, Kodama T, Nishikawa H, et al. Structural evolutions of carbon nano-peapods under electron microscopic observation. Chem Phys Lett 2004;390:462–6.
[250] Kitaura R, Imazu N, Kobayashi K, Shinohara H. Fabrication of metal nanowires in carbon nanotubes via versatile nano-template reaction. Nano Lett 2008;8:693–9.
[251] Okazaki T, Suenaga K, Hirahara K, Bandow S, Iijima S, Shinohara IE. Real time reaction dynamics in carbon nanotubes. J Am Chem Soc 2001;123:9673–4.
[252] Okazaki T, Suenaga K, Hirahara K, Bandow S, Iijima S, Shinohara H. Electronic and geometric structures of metallofullerene peapods. Physica B 2002;323:97–9.
[253] Smith BW, Luzzi DE, Achiba Y. Tumbling atoms and evidence for charge transfer in $La_2$@$C_{80}$@SWNT. Chem Phys Lett 2000;331:137–42.
[254] Suenaga K, Okazaki T, Wang CR, Bandow S, Shinohara H, Iijima S. Direct imaging of $Sc_2$@$C_{84}$ molecules encapsulated inside single-wall carbon nanotubes by high resolution electron microscopy with atomic sensitivity. Phys Rev Lett 2003;90:055506.
[255] Suenaga K, Taniguchi R, Shimada T, Okazaki T, Shinohara H, Iijima S. Evidence for the intramolecular motion of Gd atoms in a $Gd_2$@$C_{92}$ nanopeapod. Nano Lett 2003;3:1395–8.
[256] Ayala P, Kitaura R, Kramberger C, Shiozawa H, Imazu N, Kobayashi K, et al. A resonant photoemission insight to the electronic structure of Gd nanowires templated in the hollow core of SWCNTs. Mater Exp 2011;1:30–5.
[257] Briones A, Liu XJ, Kramberger C, Saito T, Pichler T. Nanochemical reactions by laser annealing of ferrocene filled single-walled carbon nanotubes. Phys Status Solidi B 2011;248:2488–91.
[258] Kocsis D, Kaptas D, Botos A, Pekker A, Kamaras K. Ferrocene encapsulation in carbon nanotubes: various methods of filling and investigation. Phys Status Solidi B 2011;248:2512–5.
[259] Liu XJ, Kuzmany H, Saito T, Pichler T. Temperature dependence of inner tube growth from ferrocene-filled single-walled carbon nanotubes. Phys Status Solidi B 2011;248:2492–5.
[260] Liu XJ, Kuzmany H, Ayala P, Calvaresi M, Zerbetto F, Pichler T. Selective enhancement of photoluminescence in filled single-walled carbon nanotubes. Adv Funct Mater 2012;22:3202–8.
[261] Plank W, Kuzmany H, Pfeiffer R, Saito T, Iijima S. Raman scattering from ferrocene encapsulated in narrow diameter carbon nanotubes. Phys Status Solidi B 2009;246:2724–7.
[262] Sauer M, Shiozawa H, Ayala P, Ruiz-Soria G, Kataura H, Yanagi K, et al. In situ filling of metallic single-walled carbon nanotubes with ferrocene molecules. Phys Status Solidi B 2012;249:2408–11.
[263] Sauer M, Shiozawa H, Ayala P, Ruiz-Soria G, Liu XJ, Chernov A, et al. Internal charge transfer in metallicity sorted ferrocene filled carbon nanotube hybrids. Carbon 2013;59:237–45.
[264] Shiozawa H, Pichler T, Pfeiffer R, Kuzmany H, Kataura H. Ferrocene encapsulated in single-wall carbon nanotubes: a precursor to secondary tubes. Phys Status Solidi B 2007;244:4102–5.
[265] Shiozawa H, Pichler T, Gruneis A, Pfeiffer R, Kuzmany H, Liu Z, et al. A catalytic reaction inside a single-walled carbon nanotube. Adv Mater 2008;20:1443–9.
[266] Shiozawa H, Kramberger C, Pfeiffer R, Kuzmany H, Pichler T, Liu Z, et al. Catalyst and chirality dependent growth of carbon nanotubes determined through nano-test tube chemistry. Adv Mater 2010;22:3685–9.
[267] Kharlamova MV, Sauer M, Saito T, Krause S, Liu X, Yanagi K, et al. Inner tube growth properties and electronic structure of ferrocene-filled large diameter single-walled carbon nanotubes. Phys Status Solidi B 2013;250:2575–80.
[268] Plank W, Pfeiffer R, Schaman C, Kuzmany H, Calvaresi M, Zerbetto F, et al. Electronic structure of carbon nanotubes with ultrahigh curvature. ACS Nano 2010;4:4515–22.
[269] Shiozawa H, Kramberger C, Rummeli M, Batchelor D, Kataura H, Pichler T, et al. Electronic properties of single-walled carbon nanotubes encapsulating a cerium organometallic compound. Phys Status Solidi B 2009;246:2626–30.
[270] Shiozawa H, Silva SRP, Liu Z, Suenaga K, Kataura H, Kramberger C, et al. Low-temperature growth of single-wall carbon nanotubes inside nano test tubes. Phys Status Solidi B 2010;247:2730–3.
[271] Kitaura R, Nakanishi R, Saito T, Yoshikawa H, Awaga K, Shinohara H. High-yield synthesis of ultrathin metal nanowires in carbon nanotubes. Angew Chem Int Ed 2009;48:8298–302.
[272] Nakanishi R, Kitaura R, Ayala P, Shiozawa H, De Blauwe K, Hoffmann P, et al. Electronic structure of Eu atomic wires encapsulated inside single-wall carbon nanotubes. Phys Rev B 2012;86:115445.
[273] Wang ZY, Shi ZJ, Gu ZN. Synthesis of single-walled carbon nanotube/metal nanoparticle hybrid materials from potassium-filled nanotubes. Carbon 2010;48:443–6.

[274] Nishide D, Dohi H, Wakabayashi T, Nishibori E, Aoyagi S, Ishida M, et al. Single-wall carbon nanotubes encaging linear chain $C_{10}H_2$ polyyne molecules inside. Chem Phys Lett 2006;428:356–60.
[275] Chamberlain TW, Popov AM, Knizhnik AA, Samoilov GE, Khlobystov AN. The role of molecular clusters in the filling of carbon nanotubes. ACS Nano 2010;4:5203–10.
[276] Yudasaka M, Ajima K, Suenaga K, Ichihashi T, Hashimoto A, Iijima S. Nano-extraction and nano-condensation for $C_{60}$ incorporation into single-wall carbon nanotubes in liquid phases. Chem Phys Lett 2003;380:42–6.
[277] Gimenez-Lopez MD, Chuvilin A, Kaiser U, Khlobystov AN. Functionalised endohedral fullerenes in single-walled carbon nanotubes. Chem Commun 2011;47:2116–8.
[278] Luzzi DE, Smith BW, Russo R, Satishkumar BC, Stercel F, Nemes N. Encapsulation of metallofullerenes and metallocenes in carbon nanotubes. AIP Conf Proc 2001;591:622–6.
[279] Shiozawa H, Rauf H, Pichler T, Knupfer M, Kalbac M, Yang S, et al. Effective valency of Dy ions in $Dy_3N@C_{80}$ metallofullerenes in peapods. AIP Conf Proc 2002;786:325–8.
[280] Chamberlain TW, Champness NR, Schroder M, Khlobystov AN. A piggyback ride for transition metals: encapsulation of exohedral metallofullerenes in carbon nanotubes. Chem A: Eur J 2011;17:668–74.
[281] Chamberlain TW, Meyer JC, Biskupek J, Leschner J, Santana A, Besley NA, et al. Reactions of the inner surface of carbon nanotubes and nanoprotrusion processes imaged at the atomic scale. Nat Chem 2011;3:732–7.
[282] Khlobystov AN. Carbon nanotubes: from nano test tube to nano-reactor. ACS Nano 2011;5:9306–8.
[283] Fan J, Chamberlain TW, Wang Y, Yang SH, Blake AJ, Schroder M, et al. Encapsulation of transition metal atoms into carbon nanotubes: a supramolecular approach. Chem Commun 2011;47:5696–8.
[284] Shiozawa H, Giusca CE, Silva SRP, Kataura H, Pichler T. Capillary filling of single-walled carbon nanotubes with ferrocene in an organic solvent. Phys Status Solidi B 2008;245:1983–5.
[285] Loebick CZ, Majewska M, Ren F, Haller GL, Pfefferle LD. Fabrication of discrete nanosized cobalt particles encapsulated inside single-walled carbon nanotubes. J Phys Chem C 2010;114:11092–7.
[286] Kataura H, Maniwa Y, Abe M, Fujiwara A, Kodama T, Kikuchi K, et al. Optical properties of fullerene and non-fullerene peapods. Appl Phys A 2002;74:349–54.
[287] Kataura H, Maniwa Y, Kodama T, Kikuchi K, Suzuki S, Achiba Y, et al. One-dimensional system in carbon nanotubes. AIP Conf Proc 2003;685:349–53.
[288] Tschirner N, Brose K, Maultzsch J, Yanagi K, Kataura H, Thomsen C. The influence of incorporated beta-carotene on the vibrational properties of single wall carbon nanotubes. Phys Status Solidi B 2010;247:2734–7.
[289] Yanagi K, Miyata Y, Kataura H. Highly stabilized beta-carotene in carbon nanotubes. Adv Mater 2006;18:437–41.
[290] Borowiak-Palen E, Mendoza E, Bachmatiuk A, Rummeli MH, Gemming T, Nogues J, et al. Iron filled single-wall carbon nanotubes – a novel ferromagnetic medium. Chem Phys Lett 2006;421:129–33.
[291] Borowiak-Palen E, Bachmatiuk A, Rummeli MH, Gemming T, Pichler T, Kalenczuk RJ. Iron filled singlewalled carbon nanotubes – synthesis and characteristic properties. Phys Status Solidi B 2006;243:3277–80.
[292] Mittal J, Monthioux M, Allouche H, Stephan O. Room temperature filling of single-wall carbon nanotubes with chromium oxide in open air. Chem Phys Lett 2001;339:311–8.
[293] Kharlamova MV, Niu JJ. Comparison of metallic silver and copper doping effects on single-walled carbon nanotubes. Appl Phys A 2012;109:25–9.
[294] Kharlamova MV, Niu JJ. Donor doping of single-walled carbon nanotubes by filling of channels with silver. JETP 2012;115:485–91.
[295] Kharlamova MV, Niu JJ. New method of the directional modification of the electronic structure of single-walled carbon nanotubes by filling channels with metallic copper from a liquid phase. JETP Lett 2012;95:314–9.
[296] Borowiak-Palen E, Ruemmeli MH, Gemming T, Pichler T, Kalenczuk RJ, Silva SRP. Silver filled single-wall carbon nanotubes – synthesis, structural and electronic properties. Nanotechnology 2006;17:2415–9.
[297] Botos A, Khlobystov AN, Botka B, Hackl R, Szekely E, Simandi B, et al. Investigation of fullerene encapsulation in carbon nanotubes using a complex approach based on vibrational spectroscopy. Phys Status Solidi B 2010;247:2743–5.
[298] Britz DA, Khlobystov AN, Wang JW, O'Neil AS, Poliakoff M, Ardavan A, et al. Selective host–guest interaction of single-walled carbon nanotubes with functionalised fullerenes. Chem Commun 2004:176–7.
[299] Khlobystov AN, Britz DA, Wang JW, O'Neil SA, Poliakoff M, Briggs GAD. Low temperature assembly of fullerene arrays in single-walled carbon nanotubes using supercritical fluids. J Mater Chem 2004;14:2852–7.
[300] Britz DA, Khlobystov AN, Porfyrakis K, Ardavan A, Briggs GAD. Chemical reactions inside single-walled carbon nano test-tubes. Chem Commun 2005:37–9.
[301] Chamberlain TW, Camenisch A, Champness NR, Briggs GAD, Benjamin SC, Ardavan A, et al. Toward controlled spacing in one-dimensional molecular chains: alkyl-chain-functionalized fullerenes in carbon nanotubes. J Am Chem Soc 2007;129:8609–14.
[302] Kissell KR, Hartman KB, Van der Heide PAW, Wilson LJ. Preparation of $I_2$@ SWNTs: synthesis and spectroscopic characterization of $I_2$-loaded SWNTs. J Phys Chem B 2006;110:17425–9.
[303] Chernysheva MV, Kiseleva EA, Verbitskii NI, Eliseev AA, Lukashin AV, Tretyakov YD, et al. The electronic properties of SWNTs intercalated by electron acceptors. Physica E 2008;40:2283–8.
[304] Ayala P, Kitaura R, Nakanishi R, Shiozawa H, Ogawa D, Hoffmann P, et al. Templating rare-earth hybridization via ultrahigh vacuum annealing of $ErCl_3$ nanowires inside carbon nanotubes. Phys Rev B 2011;83:085407.
[305] Chernysheva MV, Eliseev AA, Lukashin AV, Tretyakov YD, Savilov SV, Kiselev NA, et al. Filling of single-walled carbon nanotubes by CuI nanocrystals via capillary technique. Physica E 2007;37:62–5.
[306] Eliseev AA, Yashina LV, Brzhezinskaya MM, Chernysheva MV, Kharlamova MV, Verbitsky NI, et al. Structure and electronic properties of AgX (X = Cl, Br, I)-intercalated single-walled carbon nanotubes. Carbon 2010;48:2708–21.
[307] Eliseev AA, Yashina LV, Verbitskiy NI, Brzhezinskaya MM, Kharlamova MV, Chernysheva MV, et al. Interaction between single walled carbon nanotube and 1D crystal in CuX@SWCNT (X = Cl, Br, I) nanostructures. Carbon 2012;50:4021–39.
[308] Flahaut E, Sloan J, Coleman K, Green M. Synthesis of 1D P-block halide crystals within single walled carbon nanotubes. AIP Conf Proc 2001;59:283–6.

[309] Friedrichs S, Falke U, Green MLH. Phase separation of $LaI_3$ inside single-walled carbon nanotubes. ChemPhysChem 2005;6:300–5.
[310] Kharlamova MV, Brzhezinskaya M, Vinogradov A, Suzdalev I, Maksimov YV, Imshennik V, et al. The forming and properties of one-dimensional $FeHal_2$ (Hal = Cl, Br, I) nanocrystals in channels of single-walled carbon nanotubes. Russ Nanotechnol 2009;4:77–87.
[311] Kharlamova MV, Eliseev AA, Yashina LV, Petukhov DI, Liu CP, Wang CY, et al. Study of the electronic structure of single-walled carbon nanotubes filled with cobalt bromide. JETP Lett 2010;91:196–200.
[312] Kharlamova MV, Yashina LV, Eliseev AA, Volykhov AA, Neudachina VS, Brzhezinskaya MM, et al. Single-walled carbon nanotubes filled with nickel halogenides: atomic structure and doping effect. Phys Status Solidi B 2012;249:2328–32.
[313] Kharlamova MV, Eliseev AA, Yashina LV, Lukashin AV, Tretyakov YD. Synthesis of nanocomposites on basis of single-walled carbon nanotubes intercalated by manganese halogenides. J Phys: Conf Ser 2012;345:012034.
[314] Kharlamova MV, Yashina LV, Volykhov AA, Niu JJ, Neudachina VS, Brzhezinskaya MM, et al. Acceptor doping of single-walled carbon nanotubes by encapsulation of zinc halogenides. Eur Phys J B 2012;85:34.
[315] Kharlamova MV, Yashina LV, Lukashin AV. Comparison of modification of electronic properties of single-walled carbon nanotubes filled with metal halogenide, chalcogenide, and pure metal. Appl Phys A 2013;112:297–304.
[316] Kharlamova MV, Yashina LV, Lukashin AV. Charge transfer in single-walled carbon nanotubes filled with cadmium halogenides. J Mater Sci 2013;48:8412–9.
[317] Kharlamova MV. Comparison of influence of incorporated 3d-, 4d-and 4f-metal chlorides on electronic properties of single-walled carbon nanotubes. Appl Phys A 2013;111:725–31.
[318] Kitaura R, Ogawa D, Kobayashi K, Saito T, Ohshima S, Nakamura T, et al. High yield synthesis and characterization of the structural and magnetic properties of crystalline $ErCl_3$ nanowires in single-walled carbon nanotube templates. Nano Res 2008;1:152–7.
[319] Kumskov AS, Zhigalina VG, Chuvilin AL, Verbitskiy NI, Ryabenko AG, Zaytsev DD, et al. The structure of 1D and 3D CuI nanocrystals grown within 1.5–2.5 nm single wall carbon nanotubes obtained by catalyzed chemical vapor deposition. Carbon 2012;50:4696–704.
[320] Sloan J, Friedrichs S, Flahaut E, Brown G, Bailey SR, Coleman KS, et al. The characterisation of sub-nanometer scale structures within single walled carbon nanotubes. AIP Conf Proc 2001;591:277–82.
[321] Xu CG, Sloan J, Brown G, Bailey S, Williams VC, Friedrichs S, et al. 1D lanthanide halide crystals inserted into single-walled carbon nanotubes. Chem Commun 2000:2427–8.
[322] Zakalyukin RM, Mavrin BN, Dem'yanets LN, Kiselev NA. Synthesis and characterization of single-walled carbon nanotubes filled with the superionic material $SnF_2$. Carbon 2008;46:1574–8.
[323] Yashina LV, Eliseev AA, Kharlamova MV, Volykhov AA, Egorov AV, Savilov SV, et al. Growth and characterization of one-dimensional SnTe crystals within the single-walled carbon nanotube channels. J Phys Chem C 2011;115:3578–86.
[324] Carter R, Sloan J, Kirkland AI, Meyer RR, Lindan PJD, Lin G, et al. Correlation of structural and electronic properties in a new low-dimensional form of mercury telluride. Phys Rev Lett 2006;96:215501.
[325] Li LJ, Lin TW, Doig J, Mortimer IB, Wiltshire JG, Taylor RA, et al. Crystal-encapsulation-induced band-structure change in single-walled carbon nanotubes: photoluminescence and Raman spectra. Phys Rev B 2006;74:245418.
[326] Li LJ, Lin TW, Doig J, Mortimer IB, Wiltshire JG, Taylor RA, et al. Band structure changes in carbon nanotubes caused by $MnTe_2$ crystal encapsulation. AIP Conf Proc 2007;893:1047–8.
[327] Sloan J, Carter R, Meyer RR, Vlandas A, Kirkland AI, Lindan PJD, et al. Structural correlation of band-gap modifications induced in mercury telluride by dimensional constraint in single walled carbon nanotubes. Phys Status Solidi B 2006;243:3257–62.
[328] Kharlamova MV. Novel approach to tailoring the electronic properties of single-walled carbon nanotubes by the encapsulation of high-melting gallium selenide using a single-step process. JETP Lett 2013;98:272–7.
[329] Bajpai A, Gorantla S, Loffler M, Hampel S, Rummeli MH, Thomas J, et al. The filling of carbon nanotubes with magnetoelectric $Cr_2O_3$. Carbon 2012;50:1706–9.
[330] Friedrichs S, Meyer RR, Sloan J, Kirkland AI, Hutchison JL, Green MLH. Complete characterisation of a $Sb_2O_3$/(21, −8)SWNT inclusion composite. Chem Commun 2001:929–30.
[331] Friedrichs S, Sloan J, Green MLH, Hutchison JL, Meyer RR, Kirkland AI. Simultaneous determination of inclusion crystallography and nanotube conformation for a $Sb_2O_3$/single-walled nanotube composite. Phys Rev B 2001;64:045406.
[332] Hatakeyama R, Li Y. Synthesis and electronic-property control of Cs-encapsulated single- and double-walled carbon nanotubes by plasma ion irradiation. J Appl Phys 2007;102:034309.
[333] Jeong GH, Hatakeyama R, Hirata T, Tohji K, Motomiya K, Yaguchi T, et al. Formation and structural observation of cesium encapsulated single-walled carbon nanotubes. Chem Commun 2003:152–3.
[334] Kato T, Hatakeyama R, Shishido J, Oohara W, Tohji K. P–N junction with donor and acceptor encapsulated single-walled carbon nanotubes. Appl Phys Lett 2009;95:083109.
[335] Jeong GH, Hirata T, Hatakeyama R, Tohji K, Motomiya K. $C_{60}$ encapsulation inside single-walled carbon nanotubes using alkali-fullerene plasma method. Carbon 2002;40:2247–53.
[336] Chamberlain TW, Zoberbier T, Biskupek J, Botos A, Kaiser U, Khlobystov AN. Formation of uncapped nanometre-sized metal particles by decomposition of metal carbonyls in carbon nanotubes. Chem Sci 2012;3:1919–24.
[337] Zoberbier T, Chamberlain TW, Biskupek J, Kuganathan N, Eyhusen S, Bichoutskaia E, et al. Interactions and reactions of transition metal clusters with the interior of single-walled carbon nanotubes imaged at the atomic scale. J Am Chem Soc 2012;134:3073–9.
[338] Eliseev AA, Chernysheva MV, Verbitskii NI, Kiseleva EA, Lukashin AV, Tretyakov YD, et al. Chemical reactions within single-walled carbon nanotube channels. Chem Mater 2009;21:5001–3.
[339] Bandow S, Takizawa M, Hirahara K, Yudasaka M, Iijima S. Raman scattering study of double-wall carbon nanotubes derived from the chains of fullerenes in single-wall carbon nanotubes. Chem Phys Lett 2001;337:48–54.
[340] Pfeiffer R, Kuzmany H, Kramberger C, Schaman C, Pichler T, Kataura H, et al. Unusual high degree of unperturbed environment in the interior of single-wall carbon nanotubes. Phys Rev Lett 2003;90:225501.

[341] Simon F, Kramberger C, Pfeiffer R, Kuzmany H, Zolyomi V, Kurti J, et al. Isotope engineering of carbon nanotube systems. Phys Rev Lett 2005;95:017401.
[342] Simon F, Kukovecz A, Kramberger C, Pfeiffer R, Hasi F, Kuzmany H, et al. Diameter selective reaction processes of single-wall carbon nanotubes. Phys Rev B 2005;71:165439.
[343] Bandow S, Hiraoka T, Yumura T, Hirahara K, Shinohara H, Iijima S. Raman scattering study on fullerene derived intermediates formed within single-wall carbon nanotube: from peapod to double-wall carbon nanotube. Chem Phys Lett 2004;384:320–5.
[344] Kramberger C, Waske A, Biedermann K, Pichler T, Gemming T, Buchner B, et al. Tailoring carbon nanostructures via temperature and laser irradiation. Chem Phys Lett 2005;407:254–9.
[345] Pfeiffer R, Holzweber M, Peterlik H, Kuzmany H, Liu Z, Suenaga K, et al. Dynamics of carbon nanotube growth from fullerenes. Nano Lett 2007;7:2428–34.
[346] Fujita Y, Niwa N, Bandow S, Iijima S. Enhancement of inner tube formation from peapods in de-pressurized inert gas environment. Appl Phys A 2006;85:307–10.
[347] Fujita Y, Bandow S, Iijima S. Effect of hydrogen on polymerizing the fullerene molecules in the single-wall carbon nanotubes. Chem Lett 2007;36:94–5.
[348] Pfeiffer R, Simon F, Kuzmany H, Popov VN. Fine structure of the radial breathing mode of double-wall carbon nanotubes. Phys Rev B 2005;72:161404.
[349] Simon F, Kuzmany H. Growth of single wall carbon nanotubes from $C^{13}$ isotope labelled organic solvents inside single wall carbon nanotube hosts. Chem Phys Lett 2006;425:85–8.
[350] Pfeiffer R, Pichler T, Kim YA, Kuzmany H. Double-wall carbon nanotubes. In: Jorio A, Dresselhaus G, Dresselhaus MS, editors. Topics in applied physics, vol. 111. Berlin: Springer; 2008. p. 495–530.
[351] Byl O, Liu J, Yates JT. Etching of carbon nanotubes by ozone – a surface area study. Langmuir 2005;21:4200–4.
[352] Geng HZ, Zhang XB, Mao SH, Kleinhammes A, Wu Y, Zhou O. Opening and closing of single-wall carbon nanotubes. Abstr Pap Am Chem S 2005;229:U919.
[353] Liu J, Rinzler AG, Dai HJ, Hafner JH, Bradley RK, Boul PJ, et al. Fullerene pipes. Science 1998;280:1253–6.
[354] Dujardin E, Ebbesen TW, Krishnan A, Treacy MMJ. Wetting of single shell carbon nanotubes. Adv Mater 1998;10:1472–5.
[355] Kharlamova MV. Electronic properties of pristine and modified single-walled carbon nanotubes. Phys Usp 2013;56:1047–73.
[356] Lu J, Nagase S, Yu DP, Ye HQ, Han RS, Gao ZX, et al. Amphoteric and controllable doping of carbon nanotubes by encapsulation of organic and organometallic molecules. Phys Rev Lett 2004;93:116804.
[357] Liu X, Pichler T, Knupfer M, Golden MS, Fink J, Kataura H, et al. Filling factors, structural, and electronic properties of $C_{60}$ molecules in single-wall carbon nanotubes. Phys Rev B 2002;65:045419.
[358] Du MH, Cheng HP. Manipulation of fullerene-induced impurity states in carbon peapods. Phys Rev B 2003;68:113402.
[359] Dubay O, Kresse G. Density functional calculations for $C_{60}$ peapods. Phys Rev B 2004;70:165424.
[360] Lu J, Nagase S, Zhang S, Peng LM. Strongly size-dependent electronic properties in $C_{60}$-encapsulated zigzag nanotubes and lower size limit of carbon nanopeapods. Phys Rev B 2003;68:121402(R).
[361] Okada S, Otani M, Oshiyama A. Electron-state control of carbon nanotubes by space and encapsulated fullerenes. Phys Rev B 2003;67:205411.
[362] Otani M, Okada S, Oshiyama A. Energetics and electronic structures of one-dimensional fullerene chains encapsulated in zigzag nanotubes. Phys Rev B 2003;68:125424.
[363] Rochefort A. Electronic and transport properties of carbon nanotube peapods. Phys Rev B 2003;67:115401.
[364] Sceats EL, Green JC, Reich S. Theoretical study of the molecular and electronic structure of one-dimensional crystals of potassium iodide and composites formed upon intercalation in single-walled carbon nanotubes. Phys Rev B 2006;73:125441.
[365] Fagan SB, Filho AGS, Filho JM, Corio P, Dresselhaus MS. Electronic properties of Ag- and $CrO_3$-filled single-wall carbon nanotubes. Chem Phys Lett 2005;406:54–9.
[366] Dresselhaus MS, Dresselhaus G, Jorio A, Souza AG, Saito R. Raman spectroscopy on isolated single wall carbon nanotubes. Carbon 2002;40:2043–61.
[367] Dresselhaus MS, Eklund PC. Phonons in carbon nanotubes. Adv Phys 2000;49:705–814.
[368] Jorio A, Pimenta MA, Souza AG, Saito R, Dresselhaus G, Dresselhaus MS. Characterizing carbon nanotube samples with resonance Raman scattering. New J Phys 2003;5:139.
[369] Fouquet M, Telg H, Maultzsch J, Wu Y, Chandra B, Hone J, et al. Longitudinal optical phonons in metallic and semiconducting carbon nanotubes. Phys Rev Lett 2009;102:075501.
[370] Brown SDM, Corio P, Marucci A, Dresselhaus MS, Pimenta MA, Kneipp K. Anti-Stokes Raman spectra of single-walled carbon nanotubes. Phys Rev B 2000;61:R5137–R51340.
[371] Kalbac M, Kavan L, Dunsch L, Dresselhaus MS. Development of the tangential mode in the Raman spectra of SWCNT bundles during electrochemical charging. Nano Lett 2008;8:1257–64.
[372] Ayala P, Miyata Y, De Blauwe K, Shiozawa H, Feng Y, Yanagi K, et al. Disentanglement of the electronic properties of metallicity-selected single-walled carbon nanotubes. Phys Rev B 2009;80:205427.
[373] Kavan L, Dunsch L. Electrochemistry of carbon nanotubes. In: Jorio A, Dresselhaus G, Dresselhaus MS, editors. Topics in applied physics, vol. 111. Berlin: Springer; 2008. p. 567–603.
[374] Cronin SB, Barnett R, Tinkham M, Chou SG, Rabin O, Dresselhaus MS, et al. Electrochemical gating of individual single-wall carbon nanotubes observed by electron transport measurements and resonant Raman spectroscopy. Appl Phys Lett 2004;84:2052–4.
[375] Kavan L, Dunsch L. Spectroelectrochemistry of carbon nanostructures. ChemPhysChem 2007;8:975–98.
[376] Kavan L, Rapta P, Dunsch L. In situ Raman and Vis-NIR spectroelectrochemistry at single-walled carbon nanotubes. Chem Phys Lett 2000;328:363–8.
[377] An CP, Vardeny ZV, Iqbal Z, Spinks G, Baughman RH, Zakhidov A. Raman scattering study of electrochemically doped single wall nanotubes. Synthet Met 2001;116:411–4.

[378] Corio P, Santos PS, Brar VW, Samsonidze GG, Chou SG, Dresselhaus MS. Potential dependent surface Raman spectroscopy of single wall carbon nanotube films on platinum electrodes. Chem Phys Lett 2003;370:675–82.
[379] Corio P, Jorio A, Demir N, Dresselhaus MS. Spectro-electrochemical studies of single wall carbon nanotubes films. Chem Phys Lett 2004;392:396–402.
[380] Ghosh S, Sood AK, Rao CNR. Electrochemical tuning of band structure of single-walled carbon nanotubes probed by in situ resonance Raman scattering. J Appl Phys 2002;92:1165–7.
[381] Gupta S, Hughes M, Windle AH, Robertson J. Charge transfer in carbon nanotube actuators investigated using in situ Raman spectroscopy. J Appl Phys 2004;95:2038–48.
[382] Gupta S, Robertson J. Ion transport and electrochemical tuning of Fermi level in single-wall carbon nanotube probed by in situ Raman scattering. J Appl Phys 2006;100:083711.
[383] Gupta S. Electrochemical tuning and investigations on actuator mechanism of single-wall carbon nanotubes. Diam Relat Mater 2006;15:378–84.
[384] Murakoshi K, Okazaki K. Electrochemical potential control of isolated single-walled carbon nanotubes on gold electrode. Electrochim Acta 2005;50:3069–75.
[385] Okazaki K, Nakato Y, Murakoshi K. Absolute potential of the Fermi level of isolated single-walled carbon nanotubes. Phys Rev B 2003;68:035434.
[386] Okazaki K, Nakato Y, Murakoshi K. Characteristics of Raman features of isolated single-walled carbon nanotubes under electrochemical potential control. Surf Sci 2004;566:436–42.
[387] Rafailov PM, Maultzsch J, Thomsen C, Kataura H. Electrochemical switching of the Peierls-like transition in metallic single-walled carbon nanotubes. Phys Rev B 2005;72:045411.
[388] Rafailov PM, Thomsen C. Raman spectroscopy on electrochemically doped carbon nanotubes. J Optoelectron Adv Mater 2005;7:461–4.
[389] Stoll M, Rafailov PM, Frenzel W, Thomsen C. Electrochemical and Raman measurements on single-walled carbon nanotubes. Chem Phys Lett 2003;375:625–31.
[390] Wang ZJ, Pedrosa H, Krauss T, Rothberg L. Determination of the exciton binding energy in single-walled carbon nanotubes. Phys Rev Lett 2006;96:047403.
[391] Kalbac M, Kavan L, Zukalova M, Dunsch L. The identification of dispersive and non-dispersive intermediate frequency modes of HiPco single walled carbon nanotubes by in situ Raman spectroelectrochemistry. Phys Status Solidi B 2006;243:3134–7.
[392] Kavan L, Rapta P, Dunsch L, Bronikowski MJ, Willis P, Smalley RE. Electrochemical tuning of electronic structure of single-walled carbon nanotubes: in-situ Raman and vis-NIR study. J Phys Chem B 2001;105:10764–71.
[393] Kavan L, Dunsch L. Diameter-selective electrochemical doping of HiPco single-walled carbon nanotubes. Nano Lett 2003;3:969–72.
[394] Kavan L, Kalbac M, Zukalova M, Dunsch L. Electrochemical doping of chirality-resolved carbon nanotubes. J Phys Chem B 2005;109:19613–9.
[395] Kavan L, Kalbac M, Zukalova M, Dunsch L. Raman spectroelectrochemistry of index-identified metallic carbon nanotubes: the resonance rule revisited. Phys Status Solidi B 2006;243:3130–3.
[396] Kavan L, Dunsch L. Ionic liquid for in situ Vis/NIR and Raman spectroelectrochemistry: doping of carbon nanostructures. ChemPhysChem 2003;4:944–50.
[397] Claye A, Rahman S, Fischer JE, Sirenko A, Sumanasekera GU, Eklund PC. In situ Raman scattering studies of alkali-doped single wall carbon nanotubes. Chem Phys Lett 2001;333:16–22.
[398] Dresselhaus MS, Jorio A, Saito R. Characterizing graphene, graphite, and carbon nanotubes by Raman spectroscopy. Annu Rev Condens Matter Phys 2010;1:89–108.
[399] Garcia-Suarez VM, Ferrer J, Lambert CJ. Tuning the electrical conductivity of nanotube-encapsulated metallocene wires. Phys Rev Lett 2006;96:106804.
[400] Sceats EL, Green JC. Noncovalent interactions between organometallic metallocene complexes and single-walled carbon nanotubes. J Chem Phys 2006;125:154704.
[401] Li WF, Zhao MW, Xia YY, He T, Song C, Lin XH, et al. Silver-filled single-walled carbon nanotubes: atomic and electronic structures from first-principles calculations. Phys Rev B 2006;74:195421.
[402] Zhou J, Yan X, Luo GF, Qin R, Li H, Lu J, et al. Structural, electronic, and transport properties of Gd/Eu atomic chains encapsulated in single-walled carbon nanotubes. J Phys Chem C 2010;114:15347–53.
[403] Galpern EG, Stankevich IV, Chistykov AL, Chernozatonskii LA. Carbon nanotubes with metal inside – electron-structure of tubelenes $[Li@C_{24}]_N$ and $[K@C_{36}]_N$. Chem Phys Lett 1993;214:345–8.
[404] Du XJ, Zhang JM, Wang SF, Xu KW, Ji V. First-principle study on energetics and electronic structure of a single copper atomic chain bound in carbon nanotube. Eur Phys J B 2009;72:119–26.
[405] Ivanovskaya VV, Kohler C, Seifert G. 3d metal nanowires and clusters inside carbon nanotubes: structural, electronic, and magnetic properties. Phys Rev B 2007;75:075410.
[406] Kang YJ, Choi J, Moon CY, Chang KJ. Electronic and magnetic properties of single-wall carbon nanotubes filled with iron atoms. Phys Rev B 2005;71:115441.
[407] Meunier V, Muramatsu H, Hayashi T, Kim YA, Shimamoto D, Terrones H, et al. Properties of one-dimensional molybdenum nanowires in a confined environment. Nano Lett 2009;9:1487–92.
[408] Parq JH, Yu J, Kim G. First-principles study of ultrathin $(2 \times 2)$ Gd nanowires encapsulated in carbon nanotubes. J Chem Phys 2010;132:054701.
[409] Sun Y, Yang XB, Ni J. Bonding differences between single iron atoms versus iron chains with carbon nanotubes: first-principles calculations. Phys Rev B 2007;76:035407.
[410] Xie Y, Zhang JM, Huo YP. Structural, electronic and magnetic properties of hcp Fe, Co and Ni nanowires encapsulated in zigzag carbon nanotubes. Eur Phys J B 2011;81:459–65.
[411] Bachilo SM, Balzano L, Herrera JE, Pompeo F, Resasco DE, Weisman RB. Narrow (n, m)-distribution of single-walled carbon nanotubes grown using a solid supported catalyst. J Am Chem Soc 2003;125:11186–7.

[412] Larciprete R, Petaccia L, Lizzit S, Goldoni A. Transition from one-dimensional to three-dimensional behavior induced by lithium doping in single wall carbon nanotubes. Phys Rev B 2005;71:115435.
[413] Araujo PT, Maciel IO, Pesce PBC, Pimenta MA, Doorn SK, Qian H, et al. Nature of the constant factor in the relation between radial breathing mode frequency and tube diameter for single-wall carbon nanotubes. Phys Rev B 2008;77:241403.
[414] Kane C, Balents L, Fisher MPA. Coulomb interactions and mesoscopic effects in carbon nanotubes. Phys Rev Lett 1997;79:5086–9.
[415] Voit J. One-dimensional Fermi liquids. Rep Prog Phys 1995;58:977–1116.
[416] Chiu PW, Yang SF, Yang SH, Gu G, Roth S. Temperature dependence of conductance character in nanotube peapods. Appl Phys A 2003;76:463–7.
[417] Hornbaker DJ, Kahng SJ, Misra S, Smith BW, Johnson AT, Mele EJ, et al. Mapping the one-dimensional electronic states of nanotube peapod structures. Science 2002;295:828–31.
[418] Kato T, Hatakeyama R, Tohji K. Diffusion plasma chemical vapour deposition yielding freestanding individual single-walled carbon nanotubes on a silicon-based flat substrate. Nanotechnology 2006;17:2223–6.
[419] Lee J, Kim H, Kahng SJ, Kim G, Son YW, Ihm J, et al. Bandgap modulation of carbon nanotubes by encapsulated metallofullerenes. Nature 2002;415:1005–8.
[420] Li Y, Hatakeyama R, Shishido J, Kato T, Kaneko T. Air-stable p–n junction diodes based on single-walled carbon nanotubes encapsulating Fe nanoparticles. Appl Phys Lett 2007;90:173127.
[421] Obergfell D, Meyer JC, Haluska M, Khlobystov AN, Yang S, Fan L, et al. Transport and TEM on dysprosium metallofullerene peapods. Phys Status Solidi B 2006;243:3430–4.
[422] Okazaki T, Shimada T, Suenaga K, Ohno Y, Mizutani T, Lee J, et al. Electronic properties of $Gd@C_{82}$ metallofullerene peapods: $(Gd@C_{82})_n$@SWNTs. Appl Phys A 2003;76:475–8.
[423] Service RF. Solid-state physics – nanotube 'peapods' show electrifying promise. Science 2001;292:45.
[424] Shimada T, Okazaki T, Taniguchi R, Sugai T, Shinohara H, Suenaga K, et al. Ambipolar field-effect transistor behavior of $Gd@C_{82}$ metallofullerene peapods. Appl Phys Lett 2002;81:4067–9.
[425] Zhao JJ, Xie RH. Electronic and photonic properties of doped carbon nanotubes. J Nanosci Nanotechnol 2003;3:459–78.
[426] Lota G, Frackowiak E, Mittal J, Monthioux M. High performance supercapacitor from chromium oxide-nanotubes based electrodes. Chem Phys Lett 2007;434:73–7.
[427] Sitharaman B, Kissell KR, Hartman KB, Tran LA, Baikalov A, Rusakova I, et al. Superparamagnetic gadonanotubes are high-performance MRI contrast agents. Chem Commun 2005:3915–7.
[428] Choi JH, Nguyen FT, Barone PW, Heller DA, Moll AE, Patel D, et al. Multimodal biomedical imaging with asymmetric single-walled carbon nanotube/iron oxide nanoparticle complexes. Nano Lett 2007;7:861–7.
[429] Benjamin SC, Ardavan A, Briggs GAD, Britz DA, Gunlycke D, Jefferson J, et al. Towards a fullerene-based quantum computer. J Phys – Condens Matter 2006;18:S867–83.
[430] Zhukov AA, Gartman VK, Borisenko DN, Chernysheva MV, Eliseev AA. Measurements of work function of pristine and CuI doped carbon nanotubes. JETP 2009;109:307–13.